Tampere University

José Ángel Ochoa Martínez

COMPUTATIONAL ANALYSIS OF INTRACELLULAR CALCIUM ELEVATIONS RELATED TO MORPHOLOGY CHANGES IN ASTROCYTES

Master's thesis
Faculty of Medicine and Health Technology (MET)
Examiner: Jari Hyttinen
Examiner: Kerstin Lenk
07 / 2020

ABSTRACT

José Ángel Ochoa Martínez: Computational analysis of intracellular calcium elevations related to morphology changes in astrocytes
Master's thesis
Tampere University
Master's Degree Program in Biomedical Engineering
July 2020

Astrocytes, an essential type of glial cells, seem to be part of many neuropathologies, such as in Alzheimer's, where the astrocyte's soma and processes swells up. Astrocytes use intracellular calcium (Ca^{2+}) elevations to encode information and generate main functional chores of the cell. The increase of the astrocytic Ca^{2+} levels could be related to the synaptic activity in the brain. There is a lack of understanding of the detailed spatiotemporal Ca^{2+} dynamics in astrocytes, and computational modeling can help us to comprehend this phenomenon better. In this work, we will study how morphological changes in the astrocytes affect their intracellular Ca^{2+}.

This thesis proposes a 2D single-cell astrocyte model, simulated with the finite elements method (FEM) in COMSOL Multiphysics based on the previous study by Khalid *et al.* (2018). The mathematical model that describes the IP_3 and calcium phenomena is based on the model by De Pittà *et al.* (2009). This model was implanted in FEM and extended to cover the diffusion inside the astrocyte. Additionally, the influence of four different Ca^{2+} buffering models was examined. MATLAB and Minitab softwares were used for analyzing the data. Two different geometrical models were evaluated in order to analyse the influence of different geometrical parameters as the thickness of a process, the angle between subprocesses or the stimulus distribution to the calcium behaviour in the astrocyte.

The results showed that the frequency and propagation distance of the Ca^{2+} events are higher in narrow processes compared to wider ones while having the same stimulus. Also, my analysis showed that the angle between subprocesses and the stimulus distribution does not significantly affect the Ca^{2+} events, suggesting a possibility to to simplify future geometries. Finally, promising results showed the significant influence of the local geometry and the possibility of clustering the data by the geometrical shape. It has been statically proved how the distance between clusters is more significant when the astrocyte geometries present bigger differences between them. Furthermore, the Ca^{2+} buffers were studied, and the intracellular Ca^{2+} was affected differently depending on the buffering model, parameters, and complexity.

This work forms a base for the analysis of the Ca^{2+} in astrocytes. It also improves our understanding of the impact of morphological changes in Ca^{2+} signaling, like the thickening of astrocyte processes in different pathologies.

Keywords: Astrocytes, Calcium Signaling, Modelling, Astrocyte Geometry, Finite Element Method, Data Analysis, Calcium Buffering, Neuroscience, Brain

PREFACE

This master's thesis was done during a student's exchange at Tampere University, Finland, under the Erasmus program of the Public University of Navarra, Spain.

I am very thankful for Computational Biophysics and Imaging Group (CBIG) for accepting me to develop my master's thesis with them. Especially to my supervisors Prof Jari Hyttinen and Dr. Kerstin Lenk, for their continuous guidance and help through all the thesis. Also, a lot of thanks to the researchers Aapo Tervonen and Antti Paldanious for helping me to understand the biological processes of the cell and guiding me in the computational process of my thesis.

I would like to thank also to all my family for supporting me through all my academic life and give me the best advice from their humble roots. Thanks to my little sister for seeing me as her role model, and for sure, she will become a great future engineer.

Become a biomedical engineer has always been my goal. Now close to finish my university days is time to look for a job or a predoctoral position. The labor market presents an unknown sea full of new challenges. With a bit of luck, I will be doing something that makes me happy.

Tampere, 20 July 2020

José Ángel Ochoa Martínez

CONTENTS

LIST OF FIGURES

LIST OF TABLES

1. INTRODUCTION

Two hundred thousand years have passed since the first human brain evolved. In this time, we have been able to discover the main governing laws of our planet, travelled outside of the earth, and started to understand the laws that govern the universe. However, since the beginning of humanity, there has been something that makes all of us what we are, and its complete understanding is far from been known. We are talking about the brain, 1.5kg, with more than 170 billion cells, creating the most unknown machinery of our planet (Herculano-Houzel, 2009). Also, the most unknown organ of the human body, far from being transplanted, and in a lot of cases, irreparable.

The main communication event inside the brain is called synaptic event, and it is the way of exchanging information between neurons (Swanson *et al.*, 1999). Apart from neurons, recent studies pointed out some glia cells called astrocytes are a crucial piece in the synaptic event. Responding to the synaptic activity through calcium ion (Ca^{2+}) elevations inside the cell, they are able to decrypt the neuronal signal, release gliotransmitters and thus affect the neuronal synaptic event (Hirrlinger, Hülsmann and Kirchhoff, 2004; Agulhon *et al.*, 2008; Di Castro *et al.*, 2011; Gordleeva *et al.*, 2019). This is the environment where this thesis was developed.

Synaptic activity can lead to the activation of Gq-protein-coupled receptors (GPCR), which leads to an activation of the inositol 1,4,5-trisphosphate (IP_3) signaling cascade and results in a rise of the intracellular Ca^{2+} concentrations, mainly via the IP_3 receptor type 2 activation (IP_3R2). There is a lack of understanding of the detailed spatiotemporal Ca^{2+} dynamics in astrocytes and how the cell morphology affects them. Many astrocyte models have been published in the recent years, from mathematical as De Pittà *et al.* (2009), to the most complex 3D models as the one published by Savchenko *et al.* (2018)

This thesis proposes a 2D single-cell astrocyte model, simulated with the finite elements method (FEM) in COMSOL Multiphysics 5.4 based in previous the previous study Khalid *et al.*, 2018. The computational model that describes the calcium phenomena in 2D astrocyte FEM is based on the model by De Pittà *et al.* (2009), a mathematical model of the pathway described before. Our model describes spatiotemporally the Ca^{2+} pathway defined before and includes the diffusion of Ca^{2+} and IP_3. Calcium behavior is also af-

fected by the calcium buffering of the cell, where different structures inside the cell capture and reduce the amount of free intracellular Ca^{2+} (Verkhratsky and Butt, 2013), which will be another topic in this thesis. Four computational buffering models in astrocytes will be analysed and tested into our model.

Results will come from simulations run in simple geometries that will let us evaluate

In order to undertested better the astrocytes behaviour and its roll in neurodegenerative diseases, it is important to analyse how simple changes in the geometry affect the intracellular Ca^{2+}. For example, the thickening of a process, the angle between subprocesses, the stimulus distribution, and also the differences between geometries. It is expected to obtain the differences between the simulation models and the influence of the geometry analytically. The last step would be to relate the equations and predictions calculated statistically with published experimentation and bibliography and finalize the thesis with the conclusions extracted.

2. BIOLOGICAL AND THEORETICAL BACK-GROUND

Glia cells, in general, are the main supportive structures and the most abundant cell types in the central nervous system. They do not produce electrical impulses, but they are fundamental for the correct performance of neurons and the whole brain in general, carrying out numerous vital chores like maintaining homeostasis, taking care of the myelin, support, and protection of the brain. The main types are oligodendrocytes, astrocytes, ependymal cells, and microglía (Verkhratsky and Butt, 2013).

2.1 Introduction to astrocytes

A great part of the human brain's tissue is cover by astrocytes (Verkhratsky and Butt, 2013). The traditional view shows them basically as supportive cells, providing metabolic and structural support to the neuronal network. However, recent studies have corroborated that these cell types have a significant direct and active role in the synaptic events, neuronal activation, and regulation of brain microcirculation. As astrocytes participate in information processing and cognitive functions in the brain, they also participate in neurodegenerative diseases and numerous brain disorders (Almad and Maragakis, 2018).

This star-shaped glia cells also connect the cells controlling vasculature by vascular endfeet and by the glial sheet at brain surfaces, defining the cytoarchitecture of the grey matter of the brain. Numerous functions of vital importance in the Central Nervous System (CNS) are involved by astrocytes, including aging, development, and experience-dependent adaptation (Verkhratsky and Nedergaard, 2018).

In the mid of the 1990s, scientists recognized that astrocytes are also involved in the dynamic modulation of synaptic functions, where they are able to modulate synaptic activity releasing gliotransmitters (Parpura and Zorec, 2010). An astrocyte, a presynapse, and a postsynapse build the so-called tripartite synapse and the information travel between them with the release of gliotransmitters like glutamate and adenosine triphosphate (ATP), and it is known as the way of exchanging information between neurons (Araque *et al.*, 1999; Perea, Navarrete, and Araque, 2009; Di Castro *et al.*, 2011). These are some of the reasons to understand why astrocytes have become new novel targets

for therapeutic strategies in neuropathologies like epilepsy, ischemia, Alzheimer's, and Parkinson's diseases.

2.1.1 Astrocyte types

There exist numerous subgroups where astrocytes can be divided; the literature describes more than fourteen subtypes of different astrocytes characterized by having their own qualities. Furthermore, fibrous and protoplasmic astrocytes are the two main groups (Verkhratsky and Butt, 2013).

Fibrous astrocytes are mainly found in the white matter in the brain, in the spinal cord, and in the nerve fiber layer of the retina. Few of them can also be found in grey mather like in the thalamus of humans. Fibrous astrocytes have processes longer (up to 300 μm) and less elaborate than protoplasmic astroglia (Pfaff, D. W., & Volkow, 2016).

Protoplasmic astrocytes are mainly in the grey matter and in the spinal cord. The density of protoplasmic astrocytes in the cortex varies between 10,000 and 30,000 per mm^3. Their primary processes can be 50μm long, and also, they can extend in high elaborated branches to form complex process arborizations (Pfaff, D. W., & Volkow, 2016).

Then there are some important subtypes like surface-associated astrocytes, velate astrocytes, interlaminar astrocytes, solarized astrocytes, and varicose projection astrocytes. (Verkhratsky and Nedergaard, 2018).

2.1.2 Astrocytes in diseases

As astrocytes perform numerous vital functions for the correct performance of the brain and nervous system, they are also involved in numerous neurological diseases like Epilepsy, Alexander disease, Rett syndrome, and Alzheimer's, which are directly related to an anomer behavior of the astrocytes (Almad and Maragakis, 2018).

Alzheimer's disease (A.D.) can cause problems with memory, thinking, and behavior. Nowadays is a major cause of death for the elderly and the most common form of dementia. It results from the deposition of amyloid-β (Aβ) plaques and neurofibrillary twist. A.D. involves reactive astrocytes and microglia causing neuroinflammation, loss of neurons, and dysfunction of synapses. Reactive astrocytes in A.D. are characterized by the swelling of astrocytic processes and upregulation of glial fibrillary acidic protein (GFAP), especially close to the Aβ plaques. Also, one of the multiple astrocytes roles is to regulate

the Aβ concentrations in the brain. When they turn into pathological phenotypes, there is a defective functionality in this role (Almad and Maragakis, 2018). The hypertrophy of astrocytic processes is visible with immunoreactivity images (Figure 1) (Wilhelmsson *et al.*, 2006).

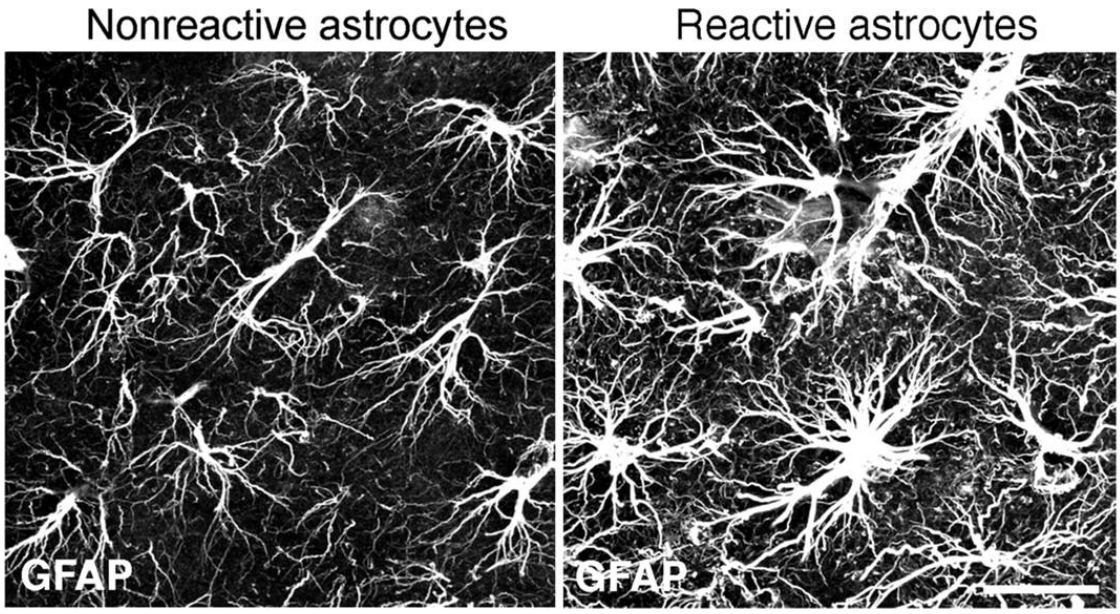

Figure 1. *Astrocytes change morphology and functionality under brain lesion in GFAP immunoreactivity. These reactive astrocytes can be related to reactive Alzheimer's astrocytes. The picture on the left shows a nonreactive group of astrocyte, and a picture on the right shows an image of reactive astrocyte when is appreciable the morphology change in them and the swollen geometry (Wilhelmsson et al., 2006).*

2.2 Calcium events in astrocytes

In astrocytes, Ca^{2+} elevations are known as the most important hallmark of their behavior. They play an essential role in signal transduction and response to the environment, as well as functionality indicators. In astrocytes, information and responses to the surrounding inputs do not travel through them with an electric potential as they are electrically non-excitable and is mainly done by Ca^{2+} transient through the cell (Verkhratsky and Nedergaard, 2018).

Numerous studies prove that intracellular Ca^{2+} elevations with their detailed spatial and temporal properties might be a result of the synaptic activity (Guerra-Gomes *et al.*, 2018). The glutamate release in the extracellular space between two neurons can induce the stimulation of the G-protein coupled metabotropic glutamate receptors (mGluRs), which

activates phospholipase C-beta (PLCβ) enzyme in the astrocyte membrane. In the membrane, PLCβ and phospholipase C-delta (PLCδ) hydrolyze phosphatidylinositol 4,5-bisphosphate (PIP2) into inositol 1,4,5-trisphosphate (IP_3). However, PLCδ, instead of being controlled by the surface receptors of the cell, it is driven by the intracellular Ca^{2+} concentration, and it is the beginning of the calcium-induced-calcium-release (CIRC) system of the cell. Then the rising of IP_3 concentration promotes the IP_3 receptor (IP_3R) channels opening, which slightly increases the intracellular Ca^{2+}. The opening probability of IP_3R channels depends nonlinearly on the Ca^{2+} concertation, and the IP3R channels control the sarco-endoplasmic reticulum (SR) Ca^{2+} -ATPase (SERCA) pumps, which release the Ca^{2+} stored in the endoplasmic reticulum (ER) to the cytosol of the astrocyte. When the Ca^{2+} concentration in the cytosol rises significantly, the IP_3R channels start to deactivate, and the SERCA pumps drive the Ca^{2+} back from the cytosol to the ER. Also, the rise of Ca^{2+} concentration in the cytosol leads to the phosphorylation of IP_3 into inositol 1,3,4,5-tetrakisphosphate (IP_4), catalyzes by IP_3 3-kinase (3K) which is controlled by the Ca^{2+} concentration, and the dephosphorylation by inositol polyphosphate 5-phosphatase (IP-5P) into PIP2. Finally, the cycle feeds back itself (Communi *et al.*, 2001; De Pittà *et al.*, 2009).

As it was said, Ca^{2+} elevations can directly affect the synaptic event through the gliotransmitters release, and they also influence circuit outputs like sensory plasticity and network synchronization (Guerra-Gomes *et al.*, 2018; Gordleeva *et al.*, 2019). However, there are many calcium pathways in astrocytes, another important one, a part of the mGluR-dependent is the glutamate transporter (GluT)-dependent pathway, in which the activity of glutamate, sodium ion (Na^+) and potassium ion (K^+) transport Ca^{2+} between the extracellular and the intracellular space (Oschmann *et al.*, 2017). Ca^{2+} wave propagation can also be transmitted between cells by two pathways; one involves second messengers from the cytosol of two adjoining astrocytes over gap junction in the intracellular channels, and the other through the activation of membrane receptors as a result of extracellular diffusion of agonists (Scemes *et al.*, 2006).

It is essential to highlight that the Ca^{2+} wave is not an ordinary propagating wave that moves through the cell with the common spatio-temporal ion diffusion concepts. The propagation of the Ca^{2+} wave is mainly a result of the release events associated with the opening of Ca^{2+} release channels through the ER membrane to the cytosol of the cell. And the calcium concentration is also drastically restricted by cytoplasmic Ca^{2+} buffering (Verkhratsky and Nedergaard, 2018).

2.3 Astrocyte imaging

2.3.1 Identification and morphology of astrocytes

Since the beginning, visualization and identification of astrocytes have been a task far from trivial, particularly in the in-situ preparations and much more in the in vivo brain imaging. The lack of a universal marker that may label astrocytes and the morphological heterogeneity of them has made it a difficult chore. Here is a summary of the most well-known markers used in different techniques for astrocyte's morphology studies.

Glutamine synthetase is a specific enzyme from astroglia that converts ammonia and glutamate into glutamine. It is situated in the cytosol, and with the immunostaining technique, it reveals the full structure of the cell (Anlauf and Derouiche, 2013). For the same purpose, it is also very extended to use the GFAP as it is an intermediate filament protein expressed in a subpopulation of astrocytes in the CNS, and also, exists an upregulated expression of GFAP in reactive astroglia (Eng, Ghirnikar and Lee, 2000). Vimentin is an intermediate filament protein also used for identifying astrocyte's morphology. It is present in immature astrocytes, in subpopulations of protoplasmic and fibrous astrocytes, and in tanycytes. In reactive astrocytes, Vimentin expression is upregulated. Finally, the connexins Cx43 and Cx30, are expressed mainly in astrocytes and Cx30 is mostly found in the grey matter and primarily concentrated in the astroglia end-feet (Nagy *et al.*, 2011; Verkhratsky and Nedergaard, 2018).

S100B protein is a Ca^{2+}- binding protein that acts as Ca^{2+} buffer for Ca^{2+} sensing (Donato *et al.*, 2012). Moreover, glutamate transporters like excitatory amino acid transporter 1 (EAAT-1), also known as glutamate aspartate transporter 1 (GLAST) and excitatory amino acid transporter 1 (EAAT-2) also known as glutamate transporter 1 (GLT-1) are specific glutamate transporters in astroglia that show regional variability. EAAT2 is the main transporter type, except in the cerebellum, where EAAT1 is predominantly expressed (Jungblut *et al.*, 2012). Finally, aquaporin (AQP4) is expressed in astrocytes and ependymocytes. AQP4 can be found in the end-feet staining the structure of healthy astrocytes (Nagelhus and Ottersen, 2013).

The transcriptional factor SOX9 labels the nucleus of astrocytes out of the neurogenic niches (Sun *et al.*, 2017). Also, Aldehyde dehydrogenase 1 family, member L1 (ALDH1L1), is a specific astroglial marker, although its expression changes with age. ALDH1L1 is an enzyme that contributes to the nucleotide biosynthesis and also in the cell division in folate metabolism (Cahoy *et al.*, 2008).

2.3.2 Calcium imaging of astrocytes

Ca^{2+} imaging is a potent tool to study astrocytes, the behavior of these cells and their response to events and cell signaling in a neighboring and local environment (McIver, Faideau and Haydon, 2013). Nevertheless, detailed spatio-temporal imaging of Ca^{2+} dynamics in astrocytes has not a trivial answer when it comes to providing enough information about the ionic functions from a local resolution to the whole-cell level, and nowadays it is still a situation to be solved. One of the biggest problems in calcium imaging results from the fact that spatial and temporal resolution used to be mutually exclusive in the majority of the cases. Wherefore, detecting the whole-cell calcium event turns into the main use if calcium imaging in astrocytes. (Losi *et al.*, 2017).

Inside the imaging techniques, wide-field microscopy was a pioneer in the new imaging techniques of astrocytes, but major improvement came in the 1980s with the confocal microscopy or confocal laser scanning microscopy (CLSM) and is the most widely used one. The refined technique and new microscopes let combine it with more tools like the immunostaining labeling to study different properties in the astrocytes (Loaiza, Porras and Barros, 2003; Perez-Alvarez, Araque and Martin, 2013). There are 2-photon and 3-photon microscopy, which are useful tools that were used, for example, in cortical and subcortical astrocytes in awake animals (1 mm depth). However, they are not useful for imaging deep structures (Horton *et al.*, 2013; Perea *et al.*, 2014). Furthermore, for imaging of deep brain (>1 mm depth) areas, it is possible to use optical microendoscopy or micro prisms. It is an invasive technique and it produces inflammation and potential damage to the imaged grain region (Chia and Levene, 2009).

In imaging with fluorescence microscopy, the main and most challenging task lies in the selection of appropriated fluorescence dyes, there are multiple of them that can be used simultaneously, and they must be carefully designed for the assignment. Furthermore, it can be a useful tool for trying to understand the functionality of the astrocyte-neuron network (Verkhratsky *et al.*, 2010). Due to their high affinity for Ca^{2+}, fluorophores can also be used to study the general effect of the neuronal activity on astrocytes and likewise to study the event of IP_3 release simultaneously with Ca^{2+} induced release. For this, a more accurate procedure is necessary without disrupting the Ca^{2+} signal. In that case, they are recommended to be used smaller molecule fluorophores and lower affinity ones like cationic mitochondrial dye 4-Di-2-ASP, sulforhodamine 101 (SR101) or β-Ala-Lys-Nε-AMCA, among others. (Preston, Cervasio and Laughlin, 2019).

New sensitive Ca^{2+} dyes, for example, genetically-encoded calcium indicators (GECIs), can monitor Ca^{2+} activity at the distal fine astrocytic processes, and several tools like viral vectors can be used to express GECIs in specific brain areas, they are able to bind Ca^{2+} and induce a change in fluorescence signal. The main disadvantages of GECIs are the potential cytotoxicity and expression techniques, and promoter sequences are critical for a good signal to noise signal (Srinivasan *et al.*, 2015).

The latest studies of the Ca^{2+} dynamics in astrocytes consider novel techniques like the three-dimensional(3D) Ca^{2+} transient thought time in the GECI GCaMP6f-expressing astrocytes with promising results due to its high sensitivity to detect Ca^{2+} waves in processes and microdomains with high-frequency Ca^{2+} transients (Losi *et al.*, 2017; Ye *et al.*, 2017).

2.4 Computational modeling of astrocytes

There is a lack of comprehension of the calcium dynamics in astrocytes. Furthermore, the fact that having detailed spatio-temporal imaging of Ca^{2+} dynamics in astrocytes is a hard task not completely solved. This makes computational modeling an exciting tool to study this cell type.

2.4.1 Computational modeling of biology

Computational Modeling of Biology, also known as Computational Biophysics, consists of *"the use of numerical algorithms to study the physical principles underlying biological phenomena and processes. It provides a means of approximating solutions for theoretical biophysical problems lacking closed-form solutions, and simulating systems for which experiments are deemed infeasible."* (Computational Biophysics, nature.com).

Computational models are also used in industry since the beginning of computing science. They can be used to corroborate laboratory results and understand the system that is being simulated. Furthermore, if a computational model of a system is developed successfully and is able to simulate the event that is being studied in the laboratory, it can reduce the laboratory experimentation and, as a consequence, reduce substantially the cost of the study.

2.4.2 Computational models of astrocytes

In biophysics, the main use of computational models is to improve the understanding of cell dynamics. There are many different types of computational cell models, including, mechanical, diffusion, electrical models, and combinations of them. However, as this thesis focus on the calcium events in astrocytes, our model will be governed mainly by diffusion equations. In the following, we highlight some models that are the bases of most of the actual studies related to the topic. Furthermore,, at the end of the section is presented a summary table with the characteristics and differences between the following models (Table 1).

Model by De Pittà et al. (2009)

De Pittà *et al.* (2009) propose a mathematical model to describe the pathway inside an astrocyte that links the synaptic event through the activation of Gq-protein-coupled receptors, with the intracellular Ca^{2+} release from the ER of the cell.

Based on Li and Rinzel *et al.* (1994), the model describes the activating and inactivating intracellular Ca^{2+} binding sites and the activating IP_3 receptors for calcium-induced calcium release. De Pittà *et al.* (2009) additionally incorporate the regulation of IP_3 production and phosphorylation, turning the model in a three-variable one.

The three-variable model is composed by the variable *C,* which refers to the Ca^{2+} concentration, *h* is a parameter used to account for the kinetics of IP_3Rs and variable *I* that refers to the IP_3 concentration; that compose the *ChI* model. Finally, this model also added the IP_3 production by external glutamate signals. In the G-ChI model, *G* represents the extracellular glutamate concentration that could come from the synaptic event and interact with the astrocyte. Compared with previous models, De Pittà *et al.* (2009) include a more detailed and realistic description of the IP_3 dynamics with complex equations for the production and degradation pathways of the molecule. It is the model used in this thesis.

For the *ChI* model, Ca^{2+} flow through the ER and the cytosol is governed by different equations that can be summarized in three variables:

$$\dot{C} = J_{SERCA} + J_{chan} + J_{leak} \tag{1}$$

The ER calcium transport through the SERCA pump, J_{SERCA}, is defined by $v_{ER,}$ which is the maximal rate of Ca^{2+} uptake by the pump, and K_{ER} is the SERCA Ca^{2+} affinity. The Hill rate expression takes the exponent 2:

$$J_{SERCA}(C) = v_{ER} \cdot Hill(C^2, K_{ER}) \quad (2)$$

The Ca^{2+} leak current, J_{leak}, is described by r_L, which is the maximal rate of Ca^{2+} leak from the ER. C_0 is the total free Ca^{2+} concentration in relation to the cytosol volume, and c_1 in the ER-to-cytosol volume ratio:

$$J_{leak}(C) = r_L\,(C_0 - (1 + c_1)C) \quad (3)$$

In the model, it is assumed that kinetic rates of binding reactions are ordered, such as the IP_3-binding leads to the Ca^{2+} -activation and then to the Ca^{2+} -inactivation. In the equation, parameters *m* and *n* follow the Hill equation (m∞ = Hill(I,d1), n∞ = Hill (C, d5)), where *d1* is the IP_3 dissociation constant, and *d5* is the Ca^{2+} activation dissociation constant. r_c is the maximal calcium-induced calcium-release (CICR) rate. m_∞^3 represent the IP3-binding and n_∞^3 theactivating Ca2+-binding (Li and Rinzel, 1994).

$$J_{chan}(C, h, I) = r_c m_\infty^3 n_\infty^3 h^3 (C_0 - (1 + c_1)C) \quad (3)$$

The *h* parameter is used to account for the kinetics of IP_3Rs and represent the fraction of channels not yet inactivated by Ca^{2+}. *h* attends the following equations, where d_1 is the IP_3 dissociation constant, d_2 the Ca^{2+} inactivation dissociation constant, d_3 the is the IP_3 dissociation constant and a_2 the IP_3R binding rate for Ca^{2+} inhibition.

$$\dot{h} = \frac{h_\infty - h}{\tau_h} \quad (4)$$

$$h_\infty = \frac{Q_2}{Q_2 + C} \quad \tau_h = \frac{1}{a_2(Q_2 + C)} \quad Q_2 = d_2 \frac{I + d_1}{I + d_3} \quad (5)$$

The equation that describes the dynamics of IP_3 production and degradation is the central component of the model, due to a great number of metabolic reactions that it describes. As a consequence of the coupling with intracellular Ca^{2+} dynamics, the equation is determinate by a complex feedback mechanism. The following equation 6, was divided

into two models, a model for the production and degradation of IP_3 governed by the CICR pathway and another model for the glutamate-dependent IP_3 production.

$$\dot{I} = \underbrace{v_\delta\,(C, I\,) + v_{5P}\,(I) + v_{3K}\,(C, I)}_{\text{Production and degradation of } IP_3} + \underbrace{v_{glu}(\gamma, C)}_{\text{Glutamate-dependent } IP_3 \text{ production}} \tag{6}$$

Fist model describes the group of equations for the production and the degradation of IP_3, which is also divided into three different variables.

$$v_\delta\,(C, I\,) + v_{5P}\,(I) + v_{3K}\,(C, I) \tag{7}$$

The production of IP_3 is driven in the equation by the variable "$v_\delta\,(C, I\,)$":

$$v_\delta\,(C, I\,) \;=\; v'_\delta\,(I\,) \cdot Hill\,(C^2, K_{PLC}) \tag{8}$$

Where the maximal PLCδ-dependent IP_3 production follows. Also parameter K_{PLC} is the Inhibition constant of PLCδ activity, k_δ is the Ca^{2+} affinity of PLCδ, and $\bar{v}_\delta$ in the maximal rate of IP_3 production by PLCδ.

$$v'_\delta\,(I) \;= \frac{\bar{v}_\delta}{1 + \frac{1}{\mathrm{k}_\delta}} \tag{9}$$

IP_3 degradation can be considered as of the Michaelis–Menten equation, which includes the rate of both IP-5P dephosphorylation (v_{5P}) and IP_3-3K phosphorylation (v_{3K}) of IP_3. $\bar{r}_{3K}$ is the maximal rate of degradation by IP_3-3K, $\bar{r}_{5p}$ is the maximal rate of degradation by IP-5P and K_D the Ca^{2+} affinity of IP_3-3K.

$$v_{5P}\,(I) \;\approx \bar{r}_{5P} \cdot I \tag{10}$$

$$v_{3K}\,(C, I) = \bar{r}_{3K} \cdot Hill(C^4, K_D) \cdot I \tag{11}$$

The second model of the equation describes the glutamate excitation event and the glutamate-dependent IP_3 production.

$$v_{glu}(\gamma, C) = \bar{v}_{\beta} \cdot R(\gamma, C) \quad (12)$$

where R(γ, C) is the fraction of activated (bound) mGluRs, and $\bar{v}_{\beta}$ the maximal rate of IP_3 production by PLCβ.

$$R(\gamma, C) = Hill(\gamma^{0.7}, K_{\gamma}(\gamma, C)) \quad (13)$$

Kγ (γ, C), can be neglected to a fist approximation and simplified as Kγ (C) (De Pittà *et al.*, 2009). Kγ (C) defines the effective Hill midpoint of R(γ, C) increased as PLCβ termination takes over, where $K_R$is the glutamate affinity of the receptor, $K_p$the Ca^{2+}/protein kinase C (PKC)-dependent inhibition factor, and K_{π} the Ca^{2+} affinity of PKC.

$$K_{\gamma}(C) \approx K_R(1 + \frac{K_p}{K_R} Hill(C, K_{\pi})) \quad (14)$$

The parameters of the De Pittà *et al.* (2009) model can be found in the appendix (Table A1).

The model can be set to the amplitude modulation (AM) or frequency modulation (FM) values. As stated in the De Pittà *et al.* (2009) paper, the IP_3 model responds to a mixed amplitude and frequency modulation (AFM) encoding of the synaptic activity and Ca^{2+} oscillations/pulsations are inherently frequency modulation (FM) encoded. Therefore, in this study, the FM parameters will be considered due to the predominant information encoded in the instantaneous frequency of the model (Alan Bloom, 2010).

Model by Oschmann et al. (2017)

Oschmann *et al.* (2017) present a mathematical model based on De Pittà *et al.* (2009) that extends the model for mGluR-dependent pathway signals in astrocytes with the glutamate transporter (GluT)-dependent pathway. The GluT-dependent pathway is describing how GluT, Na^+ and K^+ transport Ca^{2+} between the extracellular and the intracellular space; both pathways can be seen in Figure 2. Furthermore, the model includes the volume ratio between the internal Ca^{2+} store and the intracellular space applied to the geometry, and the membrane voltage (Vm). It makes it possible to analyze better the differences between Ca^{2+} signals in the soma an also close to the synapse (Oschmann *et al.*, 2017).

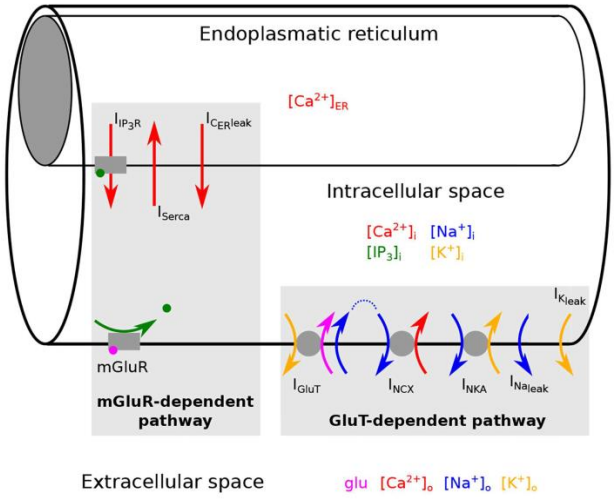

Figure 2. *Schematics of the GluT-dependent pathway and the mGluR-dependent pathway (in grey color), with the three different compartments that the model used, the intracellular space, the internal Ca^{2+} stores in the ER and the extracellular space. The picture was taken from Oschmann et al. (2017).*

Model by Savtchenko et al. (2018)

Savtchenko *et al.* (2018) developed a multi-compartmental 3D cell model, which is integrated into the NEURON environment. NEURON is a simulation platform mainly intended for computational simulations of neurons and networks of neurons. With this study, the authors were able to check the astroglial internal connectivity between the different tubular compartments where the 3D model was divided, in the experiment versus modeled one. Also, this model simulates the passive electrical properties of astrocytes, the voltage-current landscape driven by glutamate uptake, potassium uptake, and redistribution inside astroglia, the gap junctions, and hemichannels. They also probe the influence of calcium buffering on calcium waves and relate it to assessing calcium-buffering capacity in vivo.

For the Ca^{2+} model, they use CICR controlled by IP_3; The IP_3 model comes from De Pittà *et al.* (2009). The IP_3R model from Fink *et al.*, (2000), which uses a reduced version of Li&Rinzel model with simplified “h”.

With their study and simulations, they concluded that fluxes generated by GluT or K^+ channels have insignificant distant effects on membrane potential. Furthermore, the model proves that single astrocytes can effectively deal and interact with extracellular K^+ places of significant activity. Furthermore, they explain how intracellular Ca^{2+} buffers affect Ca^{2+} dynamics and why the Ca^{2+} highly localized Ca^{2+} release from the ER machinery is theoretically compatible with the results of astroglial Ca^{2+} imaging after analyzing the statistical correlations between the simulations and the laboratory experimentation.

Table 1. ***Main characteristics and differences between the computational models of astrocytes.***

Model	Ca^{2+}	IP_3	Glutamate	K^+	Na^+	Vm	Geometry	Ca2+ Buffer	Cytosol	E.R
De Pittà *et al.* (2009)	✔	✔	✔	✘	✘	✘	✘	✘	✔	✘
Oschmann *et al.* (2017)	✔	✔	✔	✔	✔	✔	Compart-mental	✘	✔	✔
Savtchenko *et al.* (2018)	✔	✔	✔	✔	✘	✔	3D	✔	✔	✔

2.4.3 Calcium Buffering

The main distinction of a molecule or process to be considered as a calcium-buffer is the ability to bind Ca^{2+} ions. However, only the Ca^{2+} binding proteins that contain acidic side-chain residues can be referred to as Ca^{2+} buffers (Gilabert, 2012).

Just a minority of the Ca^{2+} ions inside the cell are freely dissociated; most of them are bound to intracellular proteins. This effect in which the cell stabilizes the concentration of free Ca^{2+} ions is described as Ca^{2+} buffering. By binding or releasing Ca^{2+} from intracellular proteins, Ca^{2+} buffers minimize the effect of changes in cytoplasmic free Ca^{2+} concentration when Ca^{2+} is added to or removed from the cytoplasm by transport across the ER or cell membrane. Ca^{2+} sequestration into the intracellular Ca^{2+} stores represents a much more powerful process than the Ca^{2+} buffering. The Ca^{2+} buffering can be considered as a rapid process in the sub-second scale. This process determines Ca^{2+} diffusion and spatiotemporal Ca^{2+} signaling in the cell. (Gilabert, 2012). Also, buffers are used in many experiments because they have the ability to reduce evoked transmitter release in laboratory experiments, for example, when they injected them in the terminal of a giant squid synapse (E. M. Adler *et al.,* 1991).

There are many parameters for which it is crucial to know their role in Ca^{2+} signaling, for example, concentration, affinity for Ca^{2+} or Ca^{2+} binding and releasing kinetics of the buffer. Also, depending on their molecular weight and the diffusion characteristics, it is possible to do a buffer classification between mobile or immobile. Therefore, their rate constants of Ca^{2+} binding and dissociation cover a wide range in which is possible to distinguish between slow buffers (with constants values about 1 s^{-1}) and fast buffers

(constant values about 100 s^{-1}). The majority of cellular Ca^{2+} binding sites are immobile. (Falcke, 2003).

There are numerous equations that describe the Ca^{2+} buffering phenomena in the astrocyte. Here is a small summary of the different types proposed in diverse studies.

Buffering model by Hadfield et al. (2013)

The most simple buffering model would be the one proposed by Hadfield, Plank, and David in 2013. Their model behaves like a constant in front of the Ca^{2+} equation that reduces the Ca^{2+} concentration around 33%. Buffering in the cytosol performs likewise to the low-affinity Ca^{2+} buffering in many mammalian cells (Gonzalez-Fernandez and Ermentrout, 1994). The model used a modification of the model proposed by Gonzalez-Fernandez, and Ermentrout (1994), and parameters are calculated experimentally from astrocytes cultures (Wang *et al.*, 1997). The Ca^{2+} and IP_3 come from Ullah *et al.* (2006).

$$\dot{C} = \rho(J_{SERCA} + J_{chan} + J_{leak}) \tag{15}$$

$$\rho = \frac{(K_d + C)^2}{(K_d + C)^2 + K_d B_T} \tag{16}$$

In the equation parameter, "ρ" represents the fraction of cytosolic Ca^{2+} that is in the unbuffered form, and C is the free Ca^{2+} in the cytosol. K_d represents the buffer disassociation constant with a value of 20 μM, and B_T represents the total buffer concentration with a value of 10 μM.

Buffering model by Lopez-Caamal et al. (2014)

Lopez-Caamal *et al.* (2014) proposed a model based on Korngreen, Gol'shtein, and Priel, (1997). The model has a simple IP_3R model, with a constant rate of IP_3. Where c_c is the Ca^{2+} concentrations in the cytosol, and *b* is the concentration of free Ca^{2+} buffer (Lopez-Caamal *et al.*, 2014). Parameters for the equations can be found in Table 2.

$$\dot{C} = J_{SERCA} + J_{chan} + J_{leak} - J_{on} + J_{off} \tag{17}$$

$$\frac{d}{dt} b = -J_{on} + J_{off} \tag{18}$$

$$J_{on} = k_2 c_c b \tag{19}$$

$$J_{off} = k_{m2}(b_T - b) \tag{20}$$

Table 2. ***Parameters for the buffering model by Lopez-Caamal et al. (2014).***

$\mathbf{k_2}$	601 $(\mu Ms)^{-1}$	Rate of Ca^{2+} associated with the buffer
$\mathbf{k_{m2}}$	97 s^{-1}	Rate of Ca^{2+} dissociation from the buffer
$\mathbf{b_T}$	300 µM	Total concentration of the Ca^{2+} buffer.

Buffering model by Skupin et al. (2010)

Based on De Young & Keizer (IP_3R) model, the model by Skupin *et al.* has no IP_3 dynamics but a constant value of $[IP_3]$. B represents the immobile buffers and Bi the mobile ones (Skupin, Kettenmann, and Falcke, 2010). The parameters for the formulas can be found in Table 3.

$$\dot{C} = J_{SERCA} + J_{chan} + J_{leak} - k^+[B][C] + k^-([B]_T - [B]) - k_i^+[B_i][C] + k_i^-([B_i]_T - B_i) \tag{21}$$

$$\frac{d[B]}{dt} = D_B \nabla^2[B] - k^+ k^+[B][C] + k^-([B]_T - [B]) \tag{22}$$

$$\frac{dB_i}{dt} = -k_i^+[B_i][C] + k_i^-([B_i]_T - B_i) \tag{23}$$

Table 3. *Parameters for the buffering model by Skupin et al. (2010)*

$\mathbf{D_B}$	95 $\mu m^2/s$	diffusion coefficient of mobile buffer.
$\mathbf{[B]_T}$	50 µM	total mobile buffer concentration
$\mathbf{k^+_B}$	1.5 $(\mu Ms)^{-1}$	capture rate of EGTA
$\mathbf{k^-_B}$	0.3 s^{-1}	dissociation rate of EGTA
$\mathbf{k^+_B}$	600 $(\mu Ms)^{-1}$	capture rate of BAPTA [3]

k^-_B	100 s^{-1}	dissociation rate of BAPTA
$[B_i]_T$	30 µM	total immobile buffer concentration
k^+_{Bi}	1 $(\mu Ms)^{-1}$	capture rate of the immobile buffer
k^-_{Bi}	2 s^{-1}	dissociation rate of the immobile buffer

Buffering model by Komin et al. (2015)

The model by Komin *et al.* uses the De Young & Keizer (IP_3R) model and adds separately the mobile buffer to the cytosol and immobile to the ER. Parameters for the buffer equations can be found in Table 4.

$$\dot{C} = J_{SERCA} + J_{chan} + J_{leak} - k_i^+[B_i][C] + k_i^-([B_i]_T - B_i) \tag{24}$$

$$\frac{dB_i}{dt} = -k_i^+[B_i][C] + k_i^-([B_i]_T - B_i) \tag{25}$$

Table 4. *Parameters for the buffering model by Komin et al. (2015)*

D_B	95 $\mu m^2/s$	Diffusion coefficient of mobile buffer
$[B]_T$	52 µM	Total mobile buffer concentration (EGTA)
k^+_B	0.3 $(\mu Ms)^{-1}$	On rate of the mobile buffer
k^-_B	1.5 s^{-1}	Dissociation rate of the mobile buffer

Buffering model by Savtchenko et al. (2018)

Buffering equations in Savtchenko *et al.* (2018) are the same as the one used in the Skupin *et al.* model, equations 21, 22, and 23. The parameters were calculated from experiments with in vivo images of astrocytes using a virus-transduced Ca^{2+} indicator expressed under a GFAP promoter were recorded (Savtchenko *et al.*, 2018). Parameters for the buffer equations can be found in Table 5.

Table 5. *Parameters for the buffering model by Savtchenko et al. (2018)*

D_B	5 $\mu m^2/s$	diffusion coefficient of mobile buffer.
$[B]_T$	10 µM	total mobile buffer concentration
k_f	$600(\mu Ms)^{-1}$	capture rate of mobile buffer
k_D	500 s^{-1}	dissociation rate of mobile buffer
$[B_i]_T$	200 µM	total immobile buffer concentration
k_{fi}	$1000(\mu Ms)^{-1}$	capture rate of the immobile buffer
K_{Di}	20 s^{-1}	dissociation rate of the immobile buffer

2.4.4 FEM for calcium dynamics in astrocytes

An algorithm that describes a process can be written in partial differential equations (PDEs). The finite element method is one way to solve them and perform a Finite Elements Analysis (FEA), obtaining a quite well-approximated solution.

Engineers have been using FEM modeling to reduce the number of experiments and physical prototypes, also to optimize components in their designs. There is a shift from the industrial point of view of the FEM, which is the Computational Modeling of Biology. It is possible to simulate biological algorithms with the FEM technique and obtain good predictions of what is happening in the system, which can be a cell, a group of them, a complete tissue, or a prosthesis. In this area, the use of FEM is more related to the understanding of biology, which sometimes is difficult to see and predict in laboratory experiments.

It is essential to know that the differential form of the equation is considered as a strong form, and the integral form is the weak form of the equation. First, it should come from the differential equation u(x) that describes the physical phenomena and then integrate it, using, for example, integration of parts. A trial function v(x) used to be added in the procedure, that will be removed in the nodal interpolation.

$$u''(x) = f(x) \tag{26}$$

$$\int u''(x)\, v(x) = \int f(x)\, v(x) \tag{27}$$

$$u'(x)\, v(x)\Big|_0^1 - \int u'(x)\, v'(x) = \int f(x)\, v(x) \tag{28}$$

Once the integral or weak form has been structured, it is time to perform a discretization of it. The first step in the discretization consists of transforming the integral into a set of matrix equations. With this, it can be turned into a summarization that can be solved numerically.

$$\left[([M]^T\, [M'])\Big|_0^1 - \int [M']^T \cdot [M']\right]\{u\} = \int [M]^T\, [M']\, \{f\} \tag{29}$$

$$([M]^T\, [M'])\Big|_0^1 - \int [M']^T\, [M'] = [K] \tag{30}$$

$$\int [M]^T\, [M']\, \{f\} = \{R\} \tag{31}$$

$$[K]\{u\} = \{R\} \tag{32}$$

In the matrixial equation, {u} is known as the nodal vector, [K] is the stiffness matrix, and {R} is the residual vector.

The next step is to divide the domain where the equation is going to be solved in small pieces known as “elements”. This procedure is known as the “Meshing process”. It is named “node” to the corner point of each element, and this nodal point is where the unknown function u(x) will be calculated. Then an interpolation will be done to calculate the equation in all the space of nodal points, which can be one-dimensional, two-dimensional, and three-dimensional in most common cases. Moreover, not all the nodes follow the same equations; there are “boundary conditions” that define different behavior of some nodes (for example, a no-flow condition in a wall).

There is a complex mathematical methodology under the interpolation method and exist different techniques optimized depending on the study's purpose. Furthermore, ones the matrix equations have been established, we can use direct or iterative solvers depending on the type of problem.

2.4.5 FEM modeling of astrocytes

FEM modeling has been used for modeling astrocytes. For example, Khalid *et al.*, (2018) implemented the model by De Pittà *et al.*, (2009) in COMOSOL Multiphysics. They computationally demonstrated that different geometries were affecting the Ca^{2+} signaling in the astrocyte.

Apart from this study, there are more of them that corroborate the use of FEM as an interesting tool for studying different parameters in single-cell computational modeling of astrocytes. Jha, and Adlakha (2014) proposed a 2D FEM model in MATLAB to test the exogenous buffers EGTA and BAPTA in an astrocyte shape, corroborating the important role of buffers in Ca^{2+} concentration. Then the same was done with EGTA and voltage-gated calcium channel (VGCC) buffers in Jha, Adlakha and Mehta, (2019). However, there is a lack of geometry in numerous models and the attentiveness in its influence could lead into different results after running the models in more complex astrocytic morphologies. This thesis will focus on the influence of the geometry in the astrocytic Ca^{2+} FEM model.

3. METHODS

3.1 FEM model of an astrocyte

As it was shown, after De Pittà *et al.* (2009), new models had come. Nevertheless, most of them used De Pittà *et al.* (2009) equations as the bases for the intracellular Ca^{2+} dynamics models. New studies added more complexity to this model and took into account more parameters and variables. For example, the ER distribution through the cell, the membrane potential, 3D distribution, or other Ca^{2+} events also important in the cell, like Sodium/ Ca^{2+} exchanger in astroglia Ca^{2+} signaling. Notwithstanding, implementing and studying them would exceed the amount of work and time significantly for a master's thesis. Finally, only De Pittà *et al.* (2009) model with the analysis of the buffering equations has been implemented.

Furthermore, the diffusion coefficients to the molecules were added. In this case, for IP_3, a diffusion coefficient of 300 $\mu m^2/s$ was used (Kang and Othmer, 2009). Ca^{2+} has a diffusion coefficient of 13 $\mu m^2/s$ in the buffered form and 223$\mu m^2/s$ in the free ion form (Allbritton, Meyer and Stryer, 1992; Dickinson *et al.*, 2016).

For the geometrical analysis, as the majority of the Ca^{2+} in the cells is in the buffered form, the diffusion coefficient of 13 $\mu m^2/s$ was used for the computations. Moreover, since the De Pittà *et al.* (2009) model only calculates the Ca^{2+} dynamics in the astrocyte cytosol, the immobile buffer in the model by Komin *et al.* (2015) has not been considered, as it affects only Ca^{2+} in the ER.

Inside the FEM simulations, a new variable (*J_buff*) was calculated and implemented to the Ca^{2+} model for the derivation of the Ca^{2+} affected by the buffer with respect to time, and be computed inside the model; It was done for the buffering model by Skupin *et al.* (2010), the buffering model by Komin *et al.* (2015) and the buffering model by Savtchenko *et al.* (2018):

$$J\_buff = -k^+[B][C] + k^-([B]_T - [B]) - k_i^+[B_i][C] + k_i^-([B_i]_T - B_i) \qquad (33)$$

COMSOL Multiphysics 5.4 is a software developed for finite element analysis, solver, and multiphysics simulations. The Coefficient Form PDE was used to integrate the De

Pittà *et al.* (2009) astrocyte model. The simplified time-dependent equation for one dependent variable "u" was the following one:

$$\frac{du}{dt} - \nabla \cdot (c\nabla u) = f \tag{34}$$

$$u = [C, I, h]^T \tag{35}$$

$$\nabla = [\frac{d}{dx}, \frac{d}{dy}] \tag{36}$$

The parameter "u" represented the dependent variable to study. In our case, we have a three-variable problem, which is "C" that represents Ca^{2+}, "I" which represents IP_3 molecule and "h" which is the parameter used to account IP_3Rs kinetics. The equation contains the diffusion coefficient (c) of the different molecules, which is isotropic. The equations from the De Pittà *et al.* (2009) model are implemented in the source term (f), and they describe the behavior of the different dependent variables (C, I, h). Finally, the Nabla operator (∇) is a common mathematical operator that turns a function into a vector from the spatial domain of the problem.

There is an additional source term (equation 12) in the domain that only affects to the glutamate stimulation area and will be defined as a "stimulus area" thought the thesis. This is a geometrical 2D area inside the 2D geometrical model that represent computationally the domain affected by the glutamate released in synaptic activity. For comparability, the area of stimulation in all geometries was $10\mu m^2$. The glutamate concentration was constant through time with a value of 6μM. The applied parameters for the model come from De Pittà *et al.* (2009), and they can be found in the appendix (Table A1).

3.1.1 Meshing

The models were developed in 2D geometries. A triangular 2D Delaunay´s Tessellation method was applied as default. The extremely fine element was used for the mesh, although it would have been possible to run most of the simulations with bigger size elements without losing quality in the results. The extremely fine size assured convergence when the simulations were run under a parametric sweep (the variable was run for all the specified equidistant values inside a specified range of values).

3.1.2 Solver

The hierarchy under the process of solving a problem in COMSOL Multiphysics 5.4 starts with the predefined Study and Study Step Types. Default Time Dependent study was used in our case. This solver type computes the solution over time and is used when field variables change with time. The solver uses the implicit time-stepping methods backward differentiation formula (BDF) or generalized-α or an explicit method from a family of Runge-Kutta methods depending on the convergence in the simulation. Each simulation in this study was run for 200 seconds.

3.1.3 Boundary conditions

For this model, two different boundary conditions were defined. The first one was the Zero Flux across the boundary that was defined for the nodes in the outline of the geometries. The boundary equation was the following one, where “n” represented the nodal vector and are specified coefficients c, α, γ, β.

$$-n \cdot (-c\nabla u - \alpha u + \gamma) = 0 \tag{37}$$

The second one was a Flux/Source condition, where the outline of selected nodes was not affecting the dynamics of the variables. It can also be named as an out-flow condition.

$$-n \cdot (-c\nabla u - \alpha u + \gamma) = c(n \cdot u) \tag{38}$$

3.1.4 Geometries

For this thesis, two geometries were evaluated. They had been decided due to the parameters that were of interest to study.

For the rectangular geometry, these parameters were the length and width of a process (Figure 3). For their evaluation, a rectangular geometry was used. In this geometry 1, it was also evaluated if the shape of the stimulus area morphology affects the measurements, and finally, the maximum propagation distance was related to the geometry width.

In the bifurcation geometry with the shape of a “Y”, we evaluated the influence of the angle between the process bifurcation (Figure 4). Furthermore, we investigated, differences between using just one synapse location with an area of 10μm^2 or distributed it between the areas in the bifurcated subprocesses of 5μm^2 size each. Also, in this second geometry, we compared if changing the length of the body (domain defined by points “a,b,e,f” Figure 4) affected the results differently as changing the length of just one process. The two geometries are discussed below in detail.

Geometry 1: Rectangular geometry

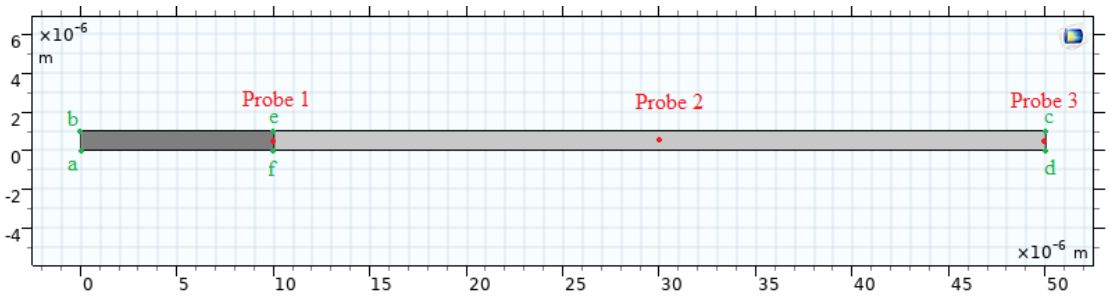

Figure 3. *Example of geometry 1 for a width of 1μm and 50μm in length. Three probes (red) were placed within the process. Letters from “a” to “f” in green color define the points that made the geometry.*

In the rectangular geometry, the different points (a to f in Figure 3) positions are determined by the combination of three parameters: L (length of the process), W (width of the process), and Asy (stimulus area). The location of the geometry points and probes can be found in Table 6. The stimulus area where the constant glutamate stimulus of 6 μM happened was the area enclosed by the points: a,b,e,f. Three probes were placed within the process to measure the Ca^{2+} and IP_3 concentration, and the *h* variable every 0.01s of simulation, and the same role for the probes in the bifurcation geometry. Flux/Source condition defined in equation 38 was applied to the external nodes between points “c” and “d”, and the Zero Flux across the boundary (equation 37) for the rest of the nodes that delimit the geometry. Simulations were run in a parametric sweep where L took values from 30μm to 180μm, and W ranged from 0.5μm to 3.5μm, representative values of in-vivo astrocytic processes (Vasile, Dossi and Rouach, 2017; Savtchenko *et al.*, 2018).

Table 6. *definition of the Rectangular geometry points and probes location*

Point	x position	y position
a	0	0
b	0	W
c	L	W
d	L	0
e	$\frac{Asy}{W}$	W
f	$\frac{Asy}{W}$	0
Probe 1	$\frac{Asy}{W}$	$\frac{W}{2}$
Probe 2	$\frac{L}{2}+\frac{Asy}{2W}$	$\frac{W}{2}$
Probe 3	L	$\frac{W}{2}$

Geometry 2: Bifurcation geometry

Figure 4. *Example of geometry 2: bifurcation geometry. Four probes (red) were placed within the process. Letters from "a" to "m" in green color define the points that made the geometry.*

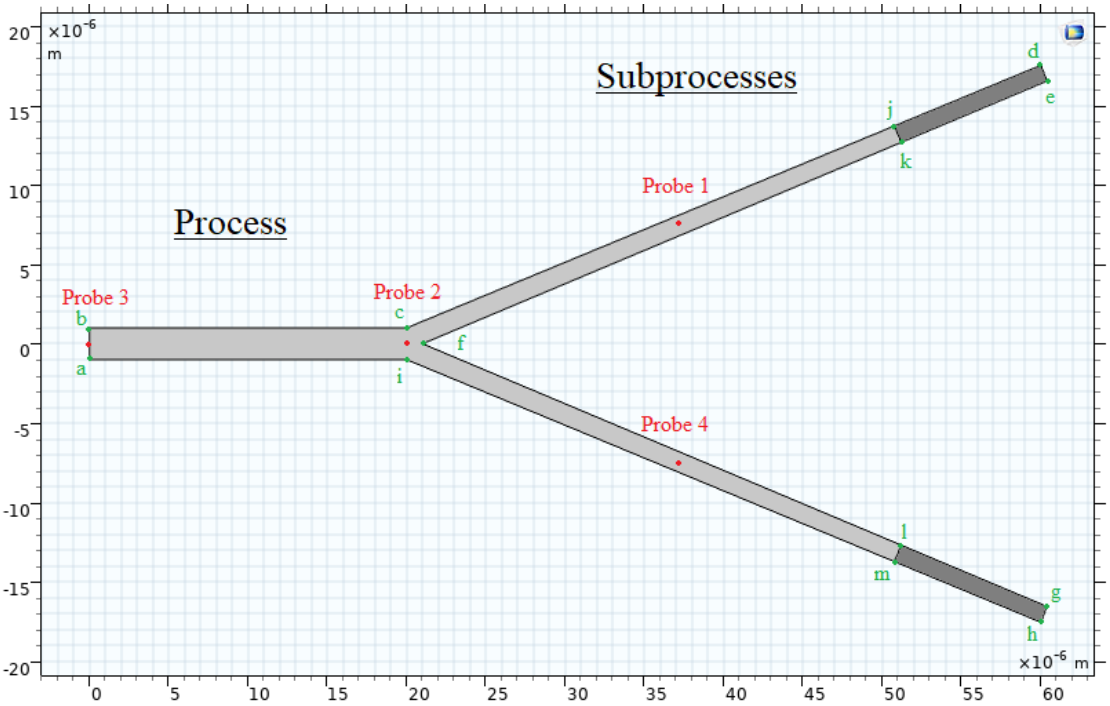

In this second geometry, the different point (a to m in Figure 4) positions were determined by the combination of six parameters: L (process length), leg1 (x-axis length of subprocess 1), leg2 (x-axis length of subprocess 2), W (subprocesses width), Asy (stimulus area), and alpha (angle between subprocesses). The definition of the geometry points can be found in Table 7. Flux/Source condition defined in equation 38 was applied to the external nodes between points "b" and "a", and the Zero Flux across the boundary (equation 37) for the rest of the nodes that delimit the geometry. The stimulus area where the constant glutamate stimulus of 6 μM was applied, was an area distributed in two sides enclosed by points j,k,d,e, and l,m,g,h, in case the stimulus was distributed in two subprocesses. If the stimulus is only in one subprocess, the whole stimulated area Asy was enclosed by j,k,d,e in subprocess 1 and enclosed by l,m,g,h in subprocess 2.

Table 7. *definition of the Bifurcation geometry points and probes locations*

Point	x position	y position
a	0	$-W$
b	0	W

c	L	W
d	$leg1 * \cos(alpha/2) + L$	$W * \cos(alpha/2) + leg1 * \sin(alpha/2)$
e	$leg1 * \cos(alpha/2) + L + W * \sin(alpha/2)$	$leg1 * \sin(alpha/2)$
f	$L + W$	0
g	$leg2 * \cos(alpha/2) + L$	$-W * \cos(alpha/2) - leg2 * \sin(alpha/2)$
h	$leg2 * \cos(alpha/2) + L + W * \sin(alpha/2)$	$-leg2 * \sin(alpha/2)$
i	L	$-W$
j	$leg1 * \cos(alpha/2) + L - \frac{Asy}{W} * \cos(alpha/2)$	$W * \cos(alpha/2) + leg1 * \sin(alpha/2) - \frac{Asy}{W} * \sin(alpha)$
k	$leg1 * \cos\left(\frac{alpha}{2}\right) + L * \sin\left(\frac{alpha}{2}\right) - \frac{Asy}{W} * \cos(alpha/2)$	$leg2 * \sin\left(\frac{alpha}{2}\right) - \frac{Asy}{W} * \sin(alpha/2)$
l	$leg2 * \cos(alpha/2) + L - \frac{Asy}{W} * \cos(alpha/2)$	$\frac{Asy}{W} * \sin(alpha/2) - W - leg * \sin(alpha/2)$
m	$leg2 * \cos(alpha/2) + L + W * \sin(alpha/2) - \frac{Asy}{W} * \cos(alpha/2)$	$Asy/W * \sin(alpha/2) - leg2 * \sin(alpha/2)$
Probe 1	$L + \frac{leg1}{2}\cos(alpha/2)$	$\frac{leg1}{2} * \sin\left(\frac{alpha}{2}\right) + \frac{W}{2} * \tan(alpha/2)$
Probe 2	L	0
Probe 3	$0 + 1 * 10^{-6}$	0

Probe 4	$L + \frac{leg2}{2}\cos(alpha/2)$	$-\frac{leg2}{2} * \sin\left(\frac{alpha}{2}\right) - \frac{W}{2} * \tan(alpha/2)$

For both geometries, we obtained the values of the IP_3 concertation, Ca^{2+} concentration, and *h* parameter in the different point probe locations for every simulation.

3.2 Calculation of geometry and activity describing features

Form COMSOL Multiphysics 5.4 simulations we got a "*.txt*" file with: the value of the simulation time, the parameter value in the sweep, the $Ca^{2+}$and IP_3 concentrations and the value of h variable for every prove in every simulation. Then this files were run in MATLAB (R2017b) to organize the data for the different simulations, and calculate, more parameters for the study; these parameters were the area of the geometry in the simulation, the average amplitude and average width at half maximum height of the Ca^{2+} peaks, and Ca^{2+} peak frequency in the simulation.

Using MATLAB's peak function [pks, locs, widths, proms] = findpeaks (C, 'MinPeakHeight', 0.3) it was possible to obtain from the Ca^{2+} signals the location and value of the local peaks (locs and pks), the threshold was selected due to all the Ca^{2+} peaks had values higher than 0.3. Based on that, we calculated the following parameters for each probe, respectively: "peaksavg" the average amplitude of the peaks. "frecuency" comes from the division of the number of peaks by the simulation time. "widthavg" represents the average full width of the peaks at half-maximum (FWHM). Then with the different parameters of the sweep simulations, we calculated the area of the whole geometry. A1 referred to the area of geometry 1 and A2 in the case of the second geometry.

$$A1 = L * W \tag{39}$$

$$A2 = L * 2W + \frac{leg1 + leg2}{\cos\left(\frac{alpha}{2}\right)} * W \tag{40}$$

3.3 Statistical analysis of the geometry and activity describing features

Minitab 19.1 is a statistical software, focused on the analysis of data and the interpretation of results. Following a statistical procedure, it is possible to find trends and patterns in the results and uncover hidden relationships between the variables.

3.3.1 ANOVA test

The first step came from doing an ANOVA test between the different simulations and looking over if there were significant differences in their means and data dispersion. If their means were significantly different in two simulations, the regression analysis of the simulations was done separately. If their means and dispersion did not represent enough differences (5% significance), the simulations were studied under the same regression analysis.

Tukey's range test or Tukey's honest significance test was used in ANOVA. This test is a very useful tool for analyzing differences between means. Tukey's honest significance test creates confidence intervals for all the combinations and controls the family error rate to a specified level. Tukey's method adjusts the confidence level in all the intervals, and simultaneously the confidence level is equal to a specified value; in our case, it has been 95% of significance (Minitab 19).

3.3.2 Regression analysis

The first step in the regression analysis was to do a matrix representation of all the possible combinations between the variables and check at first sight if there could be any linear relation between the variables.

Then before going to a predictive analysis was important to identify a possible correlation between the parameters. The Pearson's coefficient describes how strong the relation between two variables is:

$$\rho_{X,Y} = \frac{E[(X - \mu_X)(Y - \mu_Y)]}{\sigma_X \sigma_Y} \tag{41}$$

ρX,Y is the Pearson coefficient. X and Y are the variables that we want to study. σX is the standard deviation of X and σY, the standard deviation of Y. μx is the mean of X and μY, the mean of Y. E denotes the expectation. In case that the Pearson's coefficient ρ is equal to zero, there is not linear relation between the parameters, but it could be non-linear. In the case of 1> ρ > 0, there is a positive linear relationship between the parameters. If -1 < p < 0 the linear relation is negative for which Y decreases as X increases. Moreover, if the values are equal to 1 or -1 there is a perfect linear correlation direct and inverse, respectively.

For our study, we built a multiple linear regression model for investigating the dependent variables, the frequency of the Ca^{2+} event, the average width of the Ca^{2+} signal, and its average amplitude. The independent variables of the study were the width, length, area, angle, stimulus position, or geometry. The mean of the dependent variable Y was a linear function of the independent variables X:

$$E(Y/X_1 = x_1, \dots, X_k = x_k) = \beta_0 + \beta_1 x_1 + \beta_2 x_2 + \cdots + \beta_k x_k \quad (42)$$

Finally, the dependent variable was related to the independent ones, where ε represented the aleatory term of the error and E(ε)=0: (Weisberg, S., 2005).

$$Y = E(Y) + \varepsilon \quad (43)$$

For every combination of the values $x_1, x_2 \dots x_k$ from the independent variables, the variance σ^2 of ε was constant. The probability distribution of ε has to be normal, and the aleatory error was associated with the different observations independent (Minitab 19).

Furthermore, Minitab19's multiple linear regression analysis calculates the variance inflation factor (VIF) for the different coefficients in the regression. If the VIF of the coefficients presents values higher than 10, you are facing multicollinearity problems in your multiple linear regression. VIF measures how much the variance calculated with the square of the standard deviation estimation of an estimated regression coefficient is increased because of collinearity. There are different ways to solve this issue; however, in this thesis, it had been chosen to make a Best Subsets Regression and check which variables explain better our model with the least number of them, to avoid multicollinearity problems.

In the Best Subsets Regression, it is recommended to choose the model that has the highest value adjusted of the coefficient of determination (R^2) with the fewer predictor parameters and also the smaller Mallows' Cp that compares the precision and bias of

the full model to models with a subset of the predictors. Models, where Mallows' Cp is small, use to have more significant prediction potential. If the Mallows' Cp is close to the number of predictors in the model, the regression analysis will have many possibilities of having a good prediction potential and no multicollinearity problems. These rules assure that the chosen model is the best combination of the prediction parameters explaining the study variable (Minitab 19; Eddison, J., 2000).

After checking the best subset of parameters for our model without multicollinearity between them, the multiple linear regression will be done for them and analyzed in detail.

4. RESULTS

Every simulation in COMSOL Multiphysics 5.4 gives results for the IP_3 and Ca^{2+} concentrations, as well as the gating variable *h* at several probe points (Figure 5). For each simulation, the average FWHM, the average amplitude, and frequency of the Ca^{2+} wave were calculated. These features were calculated for every probe in the two geometries.

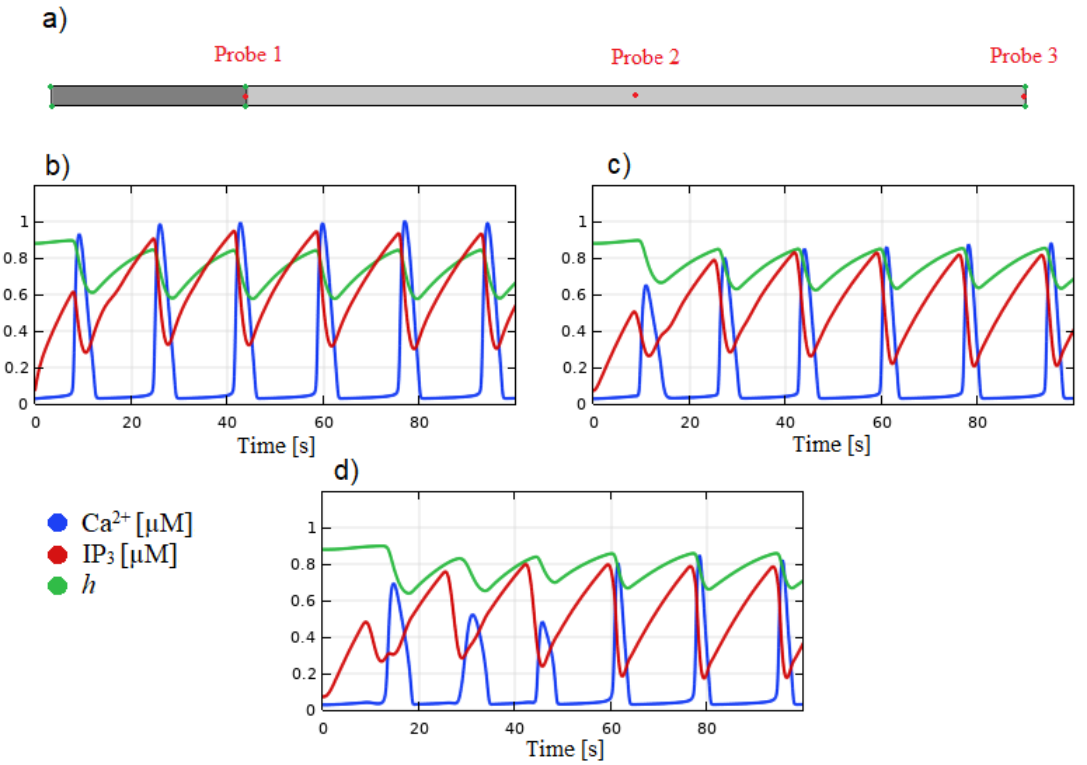

Figure 5. ***a)*** *Represent the rectangular geometry where the simulation was run. IP_3 concentration (red line), Ca^{2+} concentration (blue line), and variable h (green line) for three different probes* ***b)*** *for probe 1 to* ***d)*** *for probe 3) located in the geometry 1, geometrical values come from Figure 3. The simulation time is 100 seconds. The stimulation area had a size of 10 $\mu m^{2,}$ and glutamate concentration was 6 μM. The x-axis shows the time in seconds and the y-axis the concentration in μM.*

After the simulations in COMSOL Multiphysics 5.4 and the data treatment in MATLAB (R2017b), we proceed to analyze the results. Finally, every simulation represents one point with different associated values. Table 8 represents an example of the simulation results for geometry 1 with constant width. In each row in the table, the length of the astrocyte process was changed, and a new simulation was run.

Table 8. *example of the simulation results for geometry 1 after calculations in MATLAB (R2017b)*

L (µm)	W (µm)	peaksavg_s2 (µM)	frecuency_s2 (Hz)	widthsavg_s2 (s)	area_s2 (µm²)	peaksavg_s3 (µM)	frecuency_s3 (s)	widthsavg_s3 (s)
50.00	0.50	1.01	0.08	2.82	25.00	0.95	0.08	2.55
60.00	0.50	0.98	0.07	2.95	30.00	0.86	0.07	2.65
70.00	0.50	0.95	0.07	3.02	35.00	0.69	0.07	3.52
80.00	0.50	0.93	0.07	2.98	40.00	0.60	0.07	4.95
90.00	0.50	0.92	0.07	3.02	45.00	0.64	0.06	4.27
100.00	0.50	0.92	0.07	2.97	50.00	0.61	0.06	4.40
110.00	0.50	0.92	0.07	2.98	55.00	0.56	0.06	4.29
120.00	0.50	0.92	0.07	2.99	60.00	0.54	0.06	4.43
130.00	0.50	0.91	0.07	2.99	65.00	0.54	0.05	4.27
140.00	0.50	0.91	0.07	2.98	70.00	0.54	0.05	3.86

In Table 8, the parameter “peaks_s2” counts the number of peaks in the 200 seconds simulation in probe 1, and “peaksavg_s2” the average amplitude of the peaks for this simulation in probe 1. “frecuency_s2” Comes from the division of the number of peaks under the simulation time. “widthavg_s2” represents the average FWHM. The area is the domain area that, in this case, comes from the multiplication of the length and the width as it is a rectangular geometry. Furthermore, the rest of the terms represent the parameters for the probe 3 location. In the following, the calculated features will be compared for different topological characteristics in both geometries.

4.1 Geometry 1: Rectangular geometry

Using geometry 1, we analyzed how the length (*L*) and the width (*W*) of a process affect the Ca^{2+} dynamics of an astrocyte. Simulations were run in a parametric sweep where *L* took values from 30µm to 180µm, and *W* ranged from 0.5µm to 3.5µm, fitting reasonable configurations of an astrocyte’s process (Vasile, Dossi and Rouach, 2017; Savtchenko *et al.*, 2018).

The Ca^{2+} frequency decreased with a larger width of the astrocytic process (Figure 6a). At the investigated measurement probes 1 and 3, the Ca^{2+} frequency declined for L between 30 and 60 or 70 µm. At probe 1 for W= 1 µm (Figure 6a left) and L between 70 and 180 µm, the frequency stabilized. However, at probe 3 for W=1 µm, the frequency plateaued in-between and then decreased further (Figure 6a right). For W= 2 µm, at both probes, similar behavior was visible. At both probes 1 and 3, the frequency was zero for W=3 µm and L between 70 and 180 µm (Figure 6a). The average amplitude of the Ca^{2+} event does not change between the 3 different widths (Figure 6b) and stays at a constant value of ≈ 0.9 µM. However, the average amplitude of the Ca^{2+} event decrease from ≈1 µM to ≈ 0.4 µM, when Probe 3 increase his distance from the stimulus area (Figure 6d right). The values of the average FWM of the Ca^{2+} event does not change between the 3 different widths (Figure 6c) and stay at a constant value of ≈ 3s. However, the average

FWM of the Ca^{2+} event change when Probe 3 increase his distance from the stimulus area, starting from 2.5 s at 30µm rising till 4.5 at ≈ 30µm and going back till 3 s at 180 µm (Figure 6c right). Is possible to appreciate different values under the same area in the Ca^{2+} frequency for the 3 different widths in the geometry, higher frequency values for smaller widths (W=1 µm) than in the wider ones (W=3 µm) This evidences how the morphology of the area affects the Ca^{2+} event frequency (Figure 7).

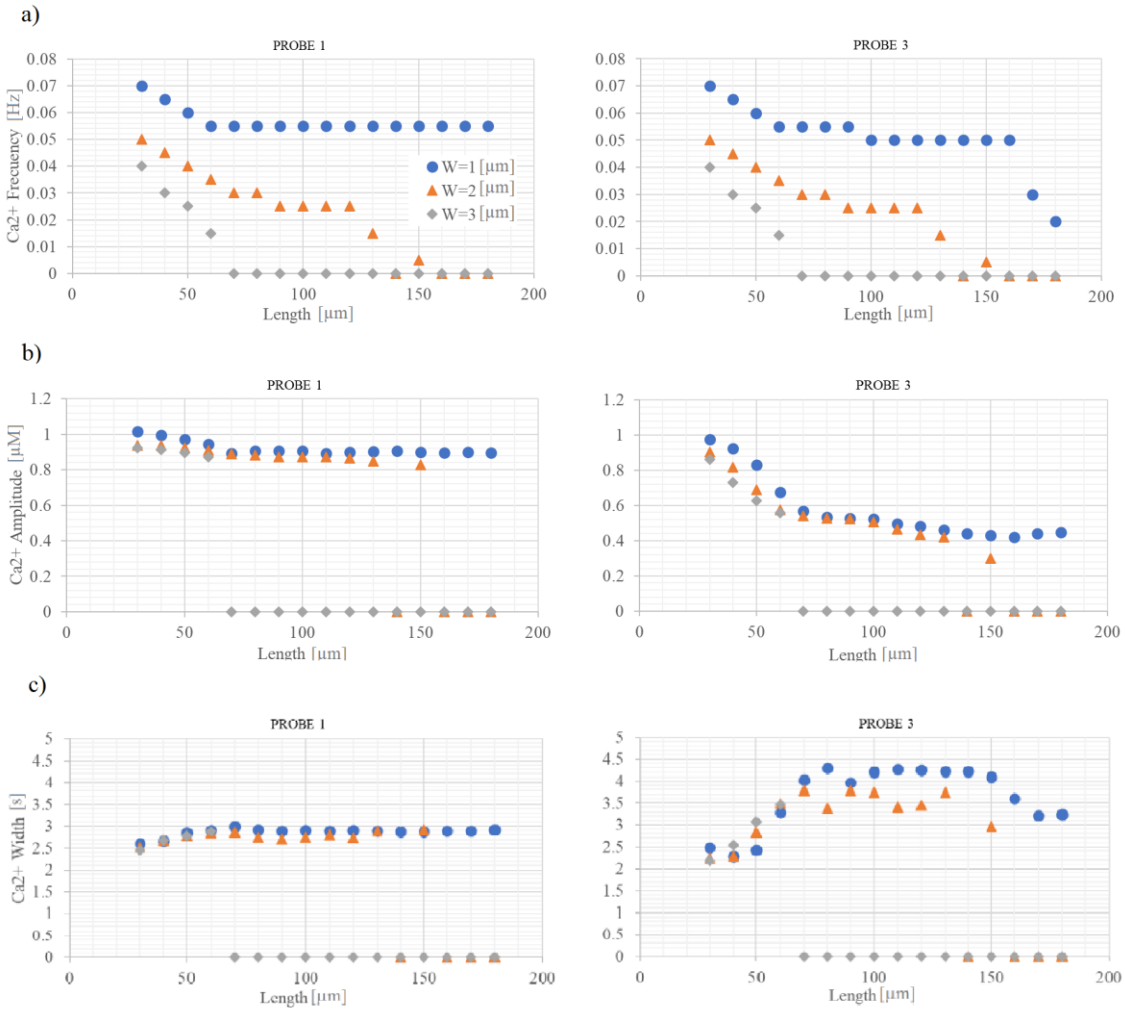

Figure 6. *Ca^{2+} dynamics independence of the process length, L, and three different widths, W. Blue circle, represents the geometry with W= 1µm, orange triangle W= 2µm, and grey diamond W=3µm. a) Ca^{2+} frequency in Hz , b) amplitude in µM and c) the FWHM in seconds [s] at probe 1 (left, respectively) and 3 (right, respectively) are presented. In the simulations, probe 1 does not change its position, and probe 3 is located at the opposite boundary and 1µm from the boundary (For a better explanation, check the tables of the geometries in the methods section: Table 6 and 7).*

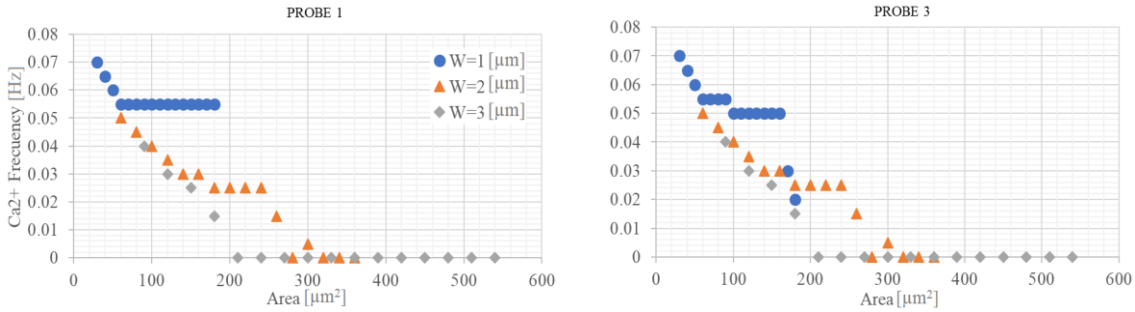

Figure 7. *Following the same markers codification as in Figure 6. This figure represents the Ca^{2+} frequency independence of the geometry 1 area [μm^2], and three different widths, W. It is possible to appreciate different values under the same area. This evidences how the morphology of the area affects the Ca^{2+} event frequency (the wider the area, the lower frequency in the Ca^{2+} event).*

4.1.1 Stimulus area morphology test

For testing, if the stimulus area morphology was affecting our results, new simulations in geometry 1 under the parametric sweep were run. In this simulation, the stimulus area in the domain was a rectangle of 0.2µm width (*Wsy*) and 50µm (*Lsy*) of constant length values for the simulations. The width of geometry 1 was varied from 0.2µm to 1.8µm and the length was a constant value of 130 µm. Results showed similar behavior to the ones in the simulations where the stimulus area was defined by the width of the geometry 1 (W=Wsy and the length of stimulation area was Lsy=W/Asy), Figure 8. Glutamate concentration and area of stimulation were always constant 6µm and 10$\mu m^{2,}$ respectively.

In Figure 8a, it is possible to observe a schematic representation of the most important geometrical parameters. The Ca^{2+} frequency in Probe 2, located in the middle of the geometry, present similar values for $W < 1$ µm and Ca^{2+} frequency for $W \geq 1$ µm is higher in simulations where W=Wsy, (Figure 8b left). Geometry with W=Wsy is able to induce the propagation of a Ca^{2+} event in $W < 1.6$ µm, while simulations were the stimulus area was a constant rectangle (0.2 x 50 µm) could not (Figure 8b). The Ca^{2+} frequency in Probe 3, located at the end of the geometry, present differences in values around $W =$ 0.6 µm, values 50% high in simulations were the stimulus area was a constant rectangle (0.2 x 50 µm), which decrease with the width meeting same value for both simulations in $W = 1.6$ µm (Figure 8b right). The linearity behavior of the Ca^{2+} frequency with *W* was higher in simulations were the stimulus area was a constant rectangle (0.2 x 50 µm). Results for the average amplitude and the average FWM of the Ca^{2+} event could be assumed the same for both simulations (Figure 8 c,d).

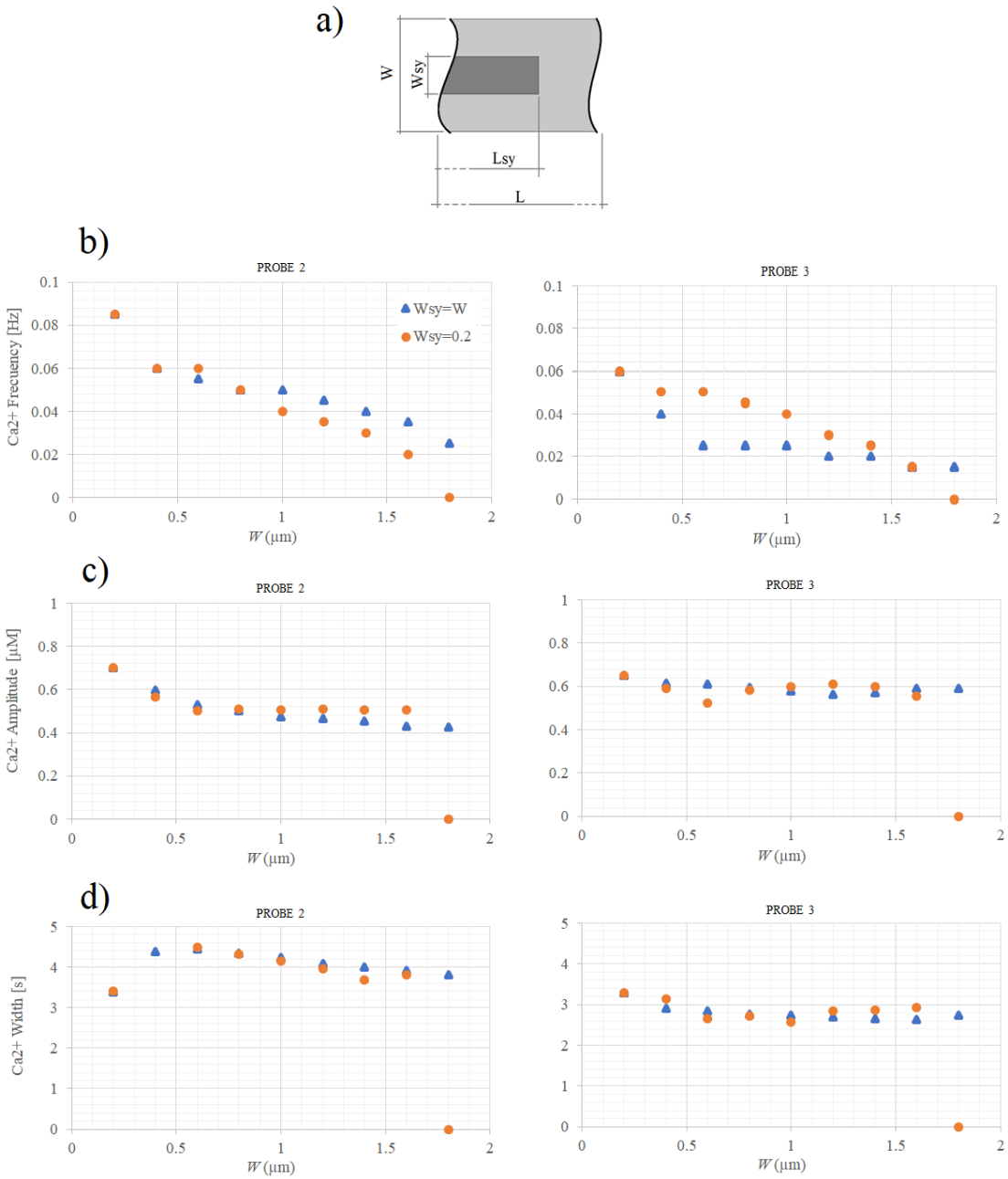

Figure 8. *Ca^{2+} dynamics independence of the process width, W. Orange circle, represents results in rectangular geometry were the stimulus area in the domain was a rectangle of 0.2µm width (Wsy) and 50µm (Lsy) of constant length values for the simulations. The width of the geometry 1 was varied from 0.2µm to 1.8µm, and the length was a constant value of 130 µm. The blue triangle represents simulations where the stimulus area was defined by the width of the geometry 1 (W=Wsy and the length of stimulation area was Lsy=W/Asy) **a)** Rectangular geometry, geometrical parameters scheme **b)** Ca^{2+} frequency in Hz , **c)** amplitude in µM and **d)** the FWHM in seconds [s] at probe 2 (left, respectively) and 3 (right, respectively) are presented.*

4.1.2 Maximum propagation distance

Maximum propagation distance calculations come from selecting the last simulations in the parametric sweep (*L* and *W)* in geometry 1 that has a Ca^{2+} event traveling through all the geometry. These results show the geometrical limitations in a subprocess (geometry 1) to propagate the Ca^{2+} event.

Ca^{2+} events that travel through the whole geometry 1 and arrive Probe 3 are the only ones that were considered here. Thus, the propagation distance is the same length as the length of geometry 1 for those simulations.

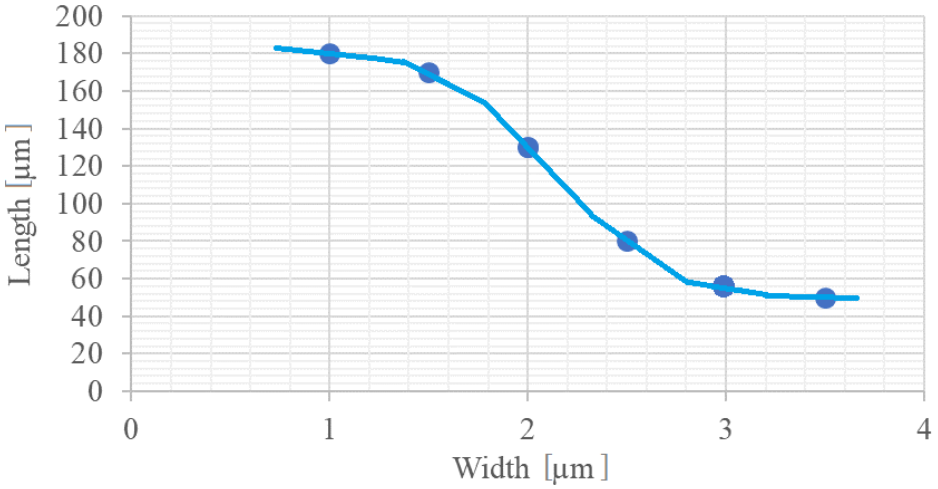

Figure 9. *Represents the maximum width and length combinations that generate a Ca^{2+} event that is able to travel through the whole geometry. The glutamate stimulus was 6µM and stimulation area 10µm^2.*

Figure 9 defines the geometries in which the Ca^{2+} event will go through all the domains. Above the line defined by the different points, there is no Ca^{2+} event appearing (simulations run in geometries wither than 3.5 µm and longer than 45 µm), or the Ca^{2+} event disappears before reaching the last probe (narrow processes of 1 µm and longer than 180 µm).

4.2 Geometry 2: Bifurcation geometry

The second geometry schematically represents an astrocyte process and two subprocesses. With this geometry, it is possible to study how the angle between subprocesses, stimulus distribution, and differences between the local and general area changes affect the Ca^{2+}.

In this geometry, there are two different geometrical changes. They are treated as two different simulations in two different geometries inside geometry 2. The first one is a parametric sweep for the main process length. As the main process (domain enclosed between points a,b,c,i in Figure 4) has twice more width than the subprocesses in our model, this simulation has a big area change on it. The second simulation inside this geometry consists of changing the length of one of the subprocesses, first the one with the stimulus, and then the one without the stimulus area on it.

All the simulations were run two times in the parametric sweep with the process length, and three times in the parametric sweep with the length of one of the subprocesses, tying like this all the combination possible with the Probe 3 location as the out-put of the system without the stimulus area at this location.

4.2.1 Angle test

In the angle test, parameter *alpha* represents the angle between the two processes (Figure 10a). Ten simulations for ten equidistant values between 10º and 190º were run for 200 seconds.

Figure 10 shows that the angle does not affect the Ca^{2+} dynamics of the astrocyte in De Pittà *et al.* (2009) model. Something that was also possible to intuit due to the physics under the model equations. At Probe 1 the frequency of the Ca^{2+} event was ≈ 0.5 Hz with the not distributed stimulus, variations in the value come from the fact, that the last Ca^{2+} event appearing in the geometry at 200s did not reach the probe on time to be computed, in the angles between 50º – 150º, and ≈ 0.3 Hz with the distributed stimulus (Figure 10b left), and it comes from the configuration of the geometry where the thickness of the subprocesses rise slightly but enough to generate a small difference in the time that the last Ca^{2+} event reaches the probe. The frequency of the Ca^{2+} event was constant in Probe 3 ≈ 0.3 Hz, (Figure 10b right). The average amplitude of the Ca^{2+} event does not change between the not distributed and distributed stimulus in Probe 1 and 3 and stays at a constant value of ≈ 0.7 μM (Figure 10c).The values of the average FWM of the Ca^{2+} event change in Probe 1 between the not distributed and distributed stimulus (Figure 10d left) and stay at a constant value of ≈ 3.5s and ≈ 4.5s, respectively. However, the average FWHM of the Ca^{2+} event did not change in Probe 3, staying in A value of ≈ 3.5s for both stimulus configurations (Figure 10d right). Differences between Probe 1 and Probe 3 in the Ca^{2+} frequency and FWHM between the distributed and not distributed stimulus,

comes from the fact that this probe is located in one subprocess in the proximity with the stimulus area (Figure 10b and 10d).

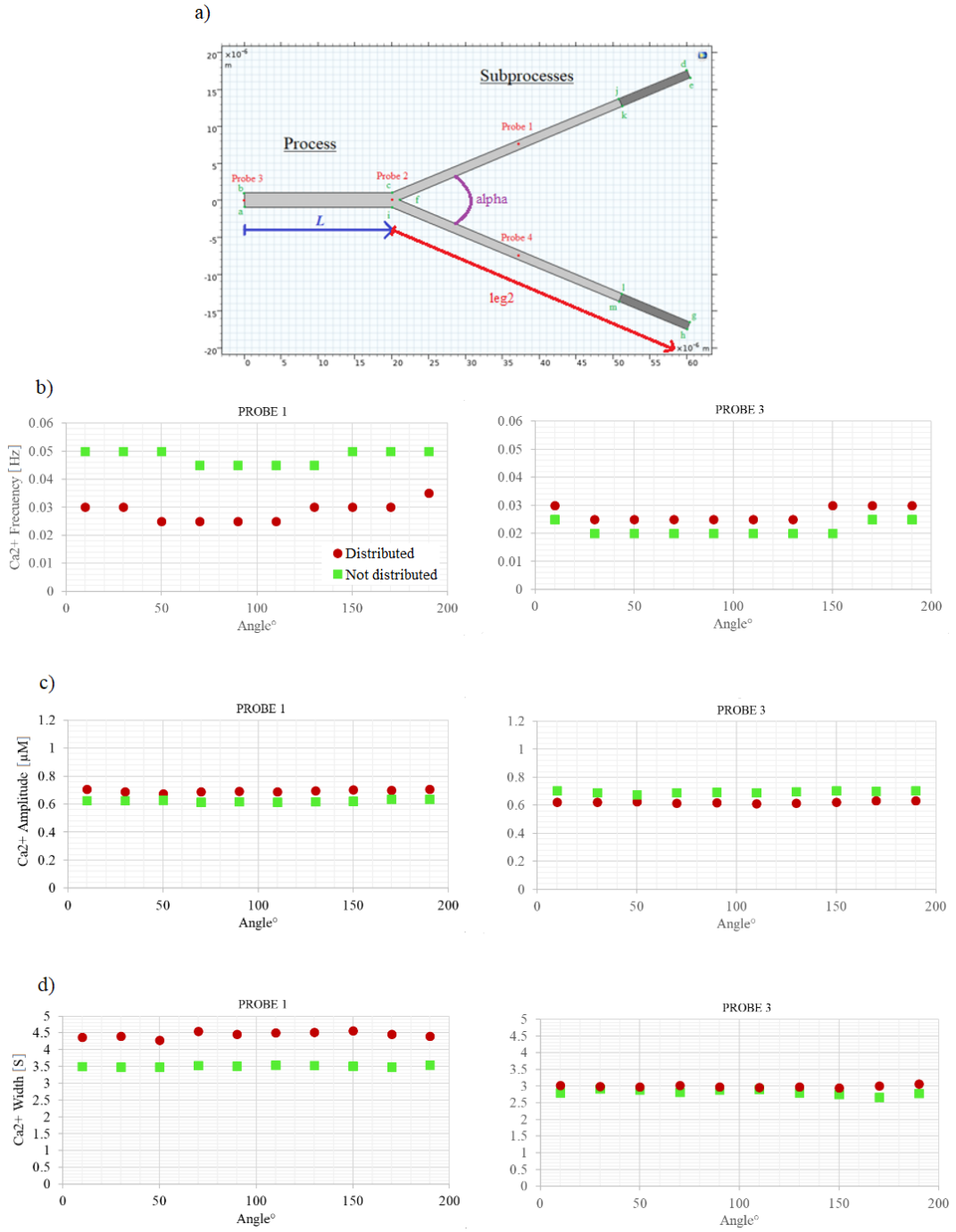

Figure 10. *Result from simulations run in geometry 2 for different angle values between the two subprocesses in the bifurcation geometry **a)**. Red circle matches the results for simulations run with the stimulus area distributed in the two different subprocesses, and the green square represents the values for the simulations where the stimulus area was only in one of the subprocesses. It is represented the values of frequency **b)**, amplitude **c)**, and FWHM of the Ca^{2+} events **d)** for different angles between the subprocesses.*

4.2.2 Process length change

With the process length test (*L* parametric sweep), probe 3 distance change and the area of the astrocyte also change significantly, but without changing the process width (Figure 11a). It is possible to see how does affect the behavior of the Ca^{2+} ion when Ca^{2+} event was produced in the same conditions or similar ones in probe 1, but the diffusion area next to the probe 3 change significantly.

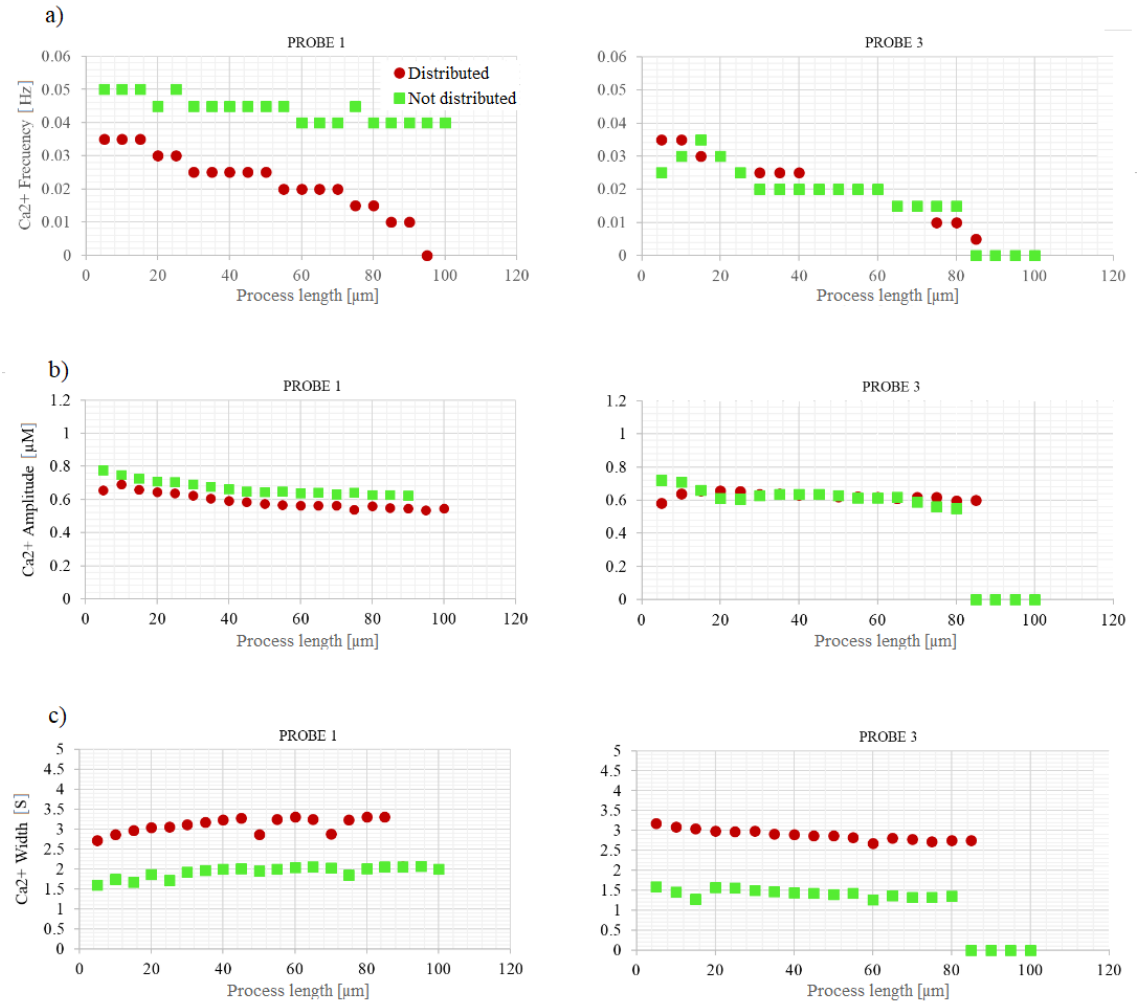

Figure 11. *Following the same markers codification as Figure 12. These simulations were run under a parametric sweep in the length of the process (L) in geometry 2.*

After simulations, it is possible to observe in Figure 11 larger differences in the frequency values and general behavior between results in probe 1 and probe 3 (left and right side, respectively in Figure 11). In probe 1, the two simulations bring different Ca^{2+} frequency; meanwhile, in probe 3 there are small differences (Figure 11a).

4.2.3 Subprocess length test

The last simulations come from changing the length of one subprocess in the bifurcation geometry (*leg2*). First, with the stimulus area distributed between the two subprocesses, then all the stimulus area was located in the upper subprocess (Figure 4) and the lower subprocess changed its length (*leg2*), in the last one the stimulus area was located in the lower subprocess which was changing is the length. Now the shape is changing without changing the area significantly, and it was possible to study how this affected the Ca^{2+} dynamics.

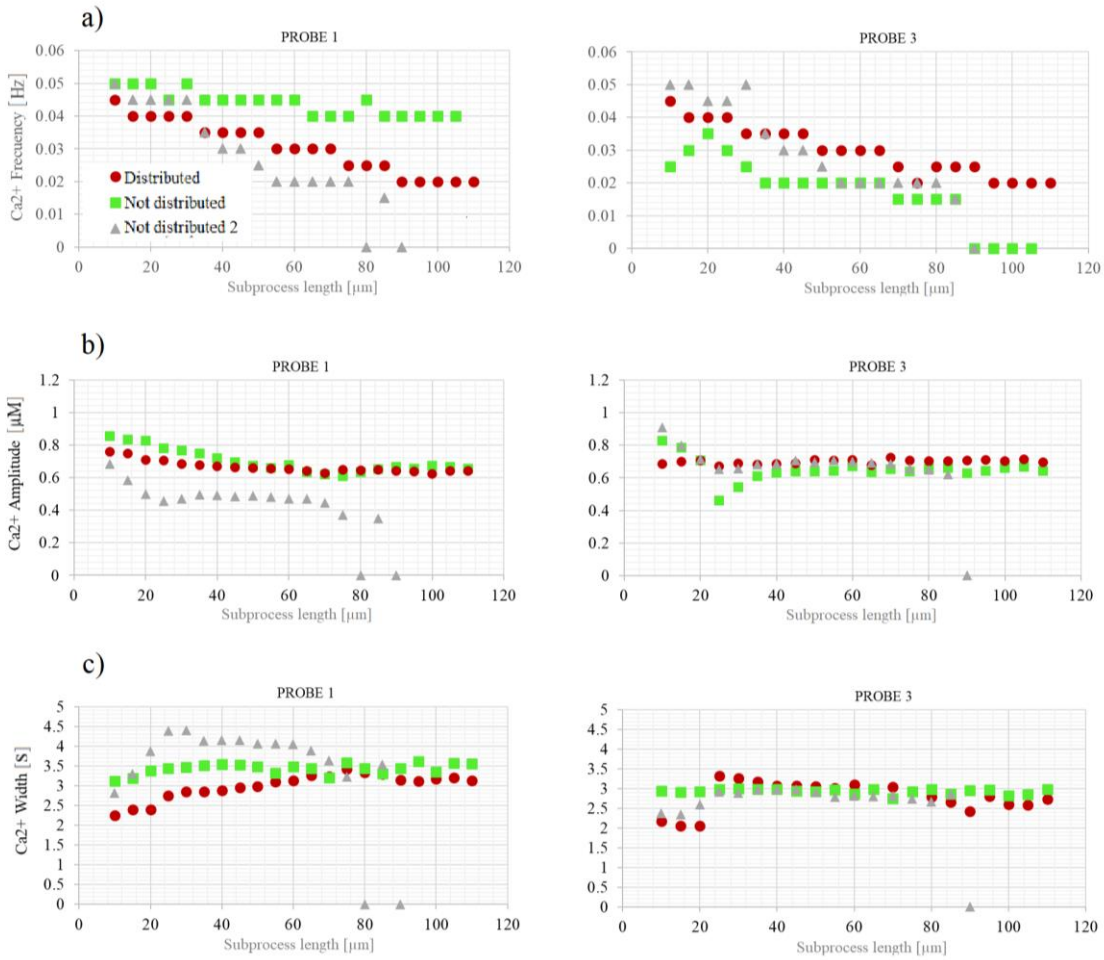

Figure 12. *Results from the parametric sweep in the length of a single subprocess in geometry 2. Red circle matches the results for simulations run with the stimulus area distributed in the two different subprocesses, the green square represents the values for the simulations where the stimulus area was only in the process of probe 1, and the other process was growing, and grey diamond marker represent the values when the stimulus area was located in the subprocess where its length was growing.*

It is possible to observe in Figure 12, similar behavior in probe 1 and 3, as in Figure 11. Ca^{2+} frequency in Probe 1 presents more significant differences between the stimulus configurations, while Probe 3 does not (Figure 12a). Moreover, the FWHM and amplitude of the Ca^{2+} present any known pattern with the studied variables in this thesis. With the statistical analysis, it will be possible to test if it is possible to accept same behavior in probe 3 for the 3 different stimulus position, and this would be suggesting that the Ca^{2+} event properties strongly depend on the morphology of the area that surrounds the measuring probe, even though the origin of the Ca^{2+} presented significant variability.

4.3 Buffering tests

This part of the thesis analyzes the simulations using our model with the rectangular geometry and the added buffering models. The diffusion coefficient of Ca^{2+} in the equation is changed for the unbuffered form of Ca^{2+} to 223$\mu m^2/s$ (equation 33) (Allbritton, Meyer and Stryer, 1992).

4.3.1 Buffering model by Hadfield *et al.* (2013)

In Figure 13, it is possible to compare our model without buffer, with Hadfield *et al.* (2015) buffer model implemented in De Pittà *et al.* (2009). Simulations were run with the parametric sweep length (*L*) for three different widths. Figure 13 shows simulations run in section *4.1Geometry 1: Rectangular geometry* and same simulations run with the Hadfield *et al.* (2015) buffer implemented in our model. It is possible to observe a reduction of the Ca^{2+} frequency in the model with the buffer implemented and in both probes and the reduction is more significant for lengths higher than 80 μm, with a reduction of ≈30% (Figure 13a), changes are less significative in the amplitude and FWHM of the Ca^{2+}event, with reductions of 1- 4% in the amplitude (Figure 13b) and increasing the FWHM around 15% (Figure 13c).

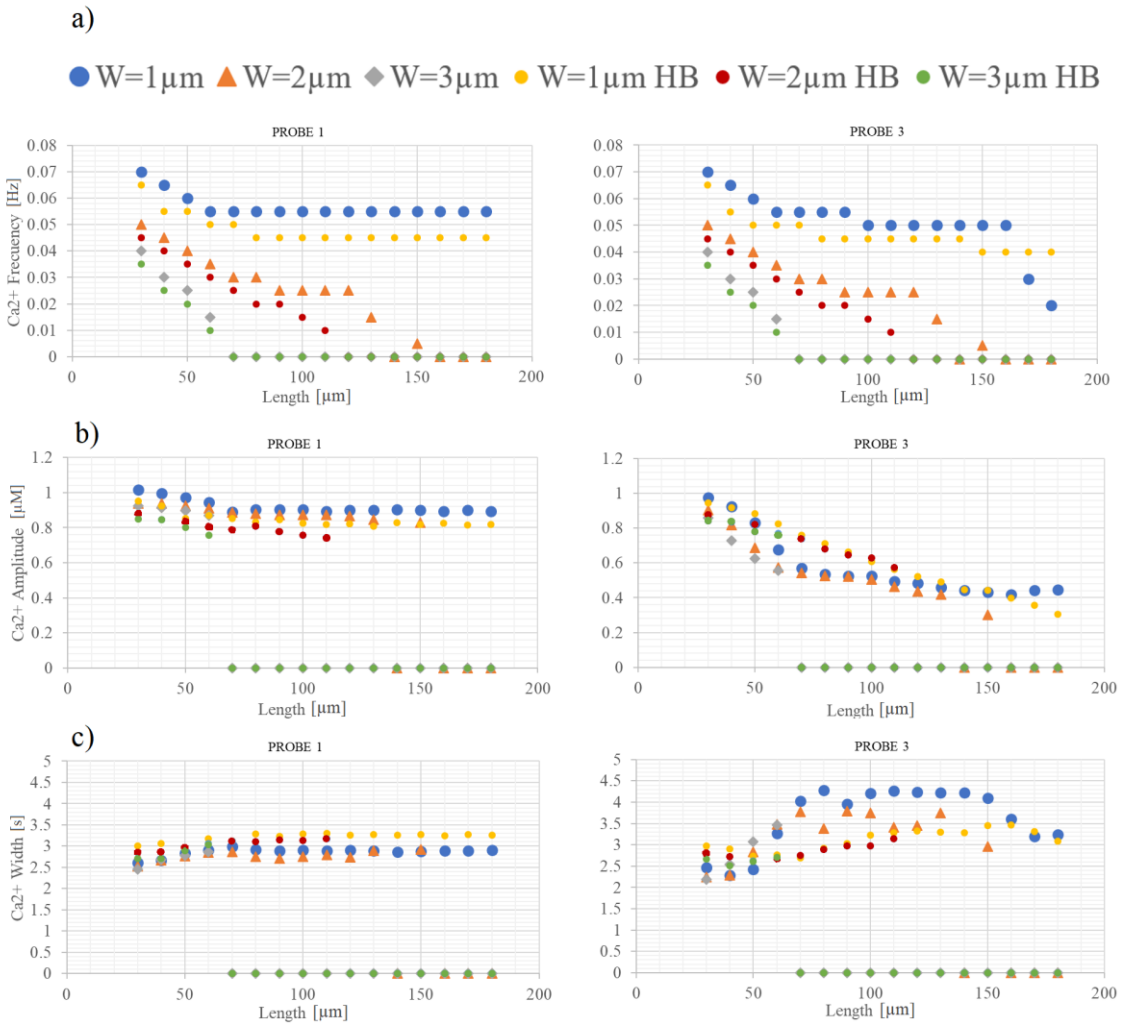

Figure 13. *Results from De Pittà et al. (2009) model and De Pittà et al. (2009) model with the buffering model of Hadfield et al. (2015). The blue circle represents the geometry with a width of 1µm, orange triangle geometry with a width of 2µm and grey diamond the 3µm one for De Pittà et al. (2009) model. Under these markers are located the ones for results of De Pittà et al. (2009) model with the buffering model of Hadfield et al. (2015), Small yellow circle represents the geometry with a width of 1µm, red one geometry with a width of 2µm and green one the 3µm width.* ***a)*** *Ca2+ frequency in Hz,* ***b)*** *amplitude in µM, and* ***c)*** *the FWHM in seconds [s] at probe 1 (left, respectively), and 3 (right, respectively) are presented.*

4.3.2 Buffering model by Lopez- Caamal *et al.* (2015)

The buffer model by Lopez-Caamal *et al.* (2015) contains more complex equations (equations number 17-20). These equations describe the buffering phenomenon in detail. As this buffering model was calculated to fit in the Ca^{2+} equation that the study was using, when it is added to De Pitta *et al.* (2009) model with the original parameters that Lopez-Caamal *et al.* (2015), was using, the buffer parameters result too big for our model, and Ca^{2+} dynamics disappear from the results.

In Figure 13 it is possible to observe the results after one simulation run for Lopez-Caamal *et al.* (2015) buffering model implemented in De Pitta *et al.* (2009) in the Geometry 1, with 80μm of length, 1μm width and 10μm^2 of stimulation area with 6μM of glutamate stimulus. In Figure 13c is plotted *b* variable from equation 18, which is the concentration of free Ca^{2+} buffer, it can also be seen as the Ca^{2+} buffer concentration that binds Ca^{2+}, and $(b_T - b)$ as the Ca^{2+} buffer concentration that unbinds Ca^{2+}, equations 19-20.

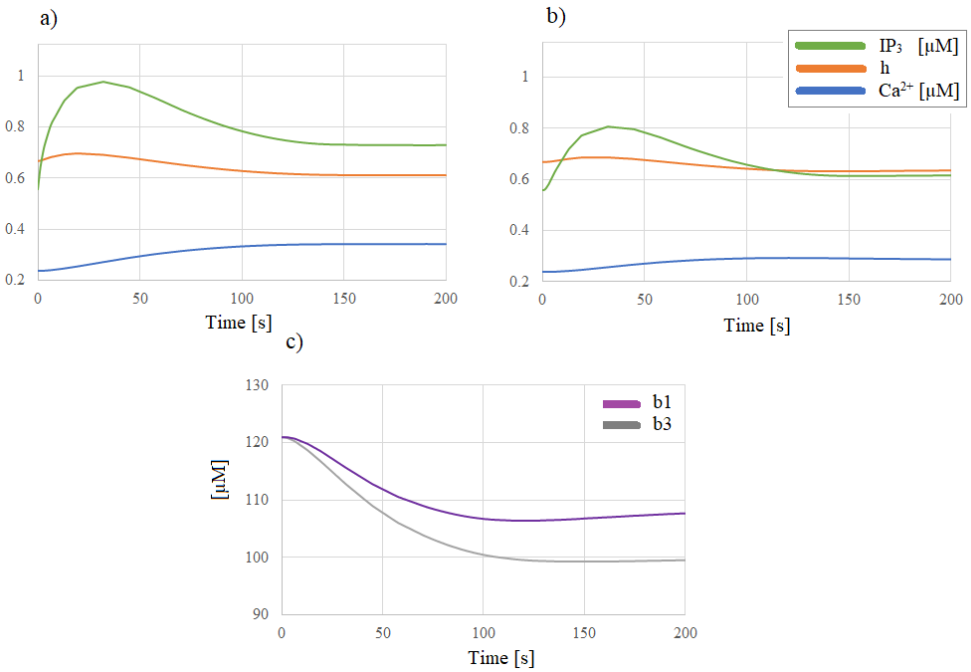

Figure 14. *Results from Lopez-Caamal et al. (2015) buffering model implemented in De Pittà et al. (2009). In plots **a)** and **b)** are represented the Ca^{2+} concentration in the blue line, IP_3 concentration with a green line, and the orange line is the value of h parameter; for probe 1 in **a)** and probe 3 in **b)**. Rectangular geometry of 80μm length and 1μm width, under the same stimulus as all the simulation, is this thesis was used. Finally, in plot "c", it is represented the buffer parameter that matches the '' b '' variable in Lopez – Caamal et al. 2015 model that counts the concentration of buffer associated with the Ca^{2+}, purple line for the measurement in probe 1 (b1) and grey for probe 3 (b3).*

4.3.3 Buffering model by Skupin *et al.* (2010)

The same problem as it was named before is appreciable in this model, Skupin *et al.* (2010) buffer are less potent than the one used in Lopez-Caamal *et al.* (2015) model, and it let appear some of the Ca^{2+} waves on the model. However, they are profoundly affected by the damping of the buffer, and the system reaches a stationary concentration after 100s, even though the glutamate stimulus continues continuously. Focusing on the Ca^{2+} concentration of buffer associated with the Ca^{2+}, it is possible to appreciate in Figure 15c the blinding and unblinding phenomena with ups and downs in the concentration, respectively. The concentration of buffer associated with the Ca^{2+} in immobile buffers presents more variations over time than the mobile one. The response from the buffer to the Ca^{2+} concentration highly depends on the parameters that compose it, equations 21-23. It is also possible to observe a higher IP_3 concentration in Probe 1, because it is located close to the glutamate stimulus area, where the IP_3 is produced mainly by the glutamate-dependent IP_3 production, equation 12.

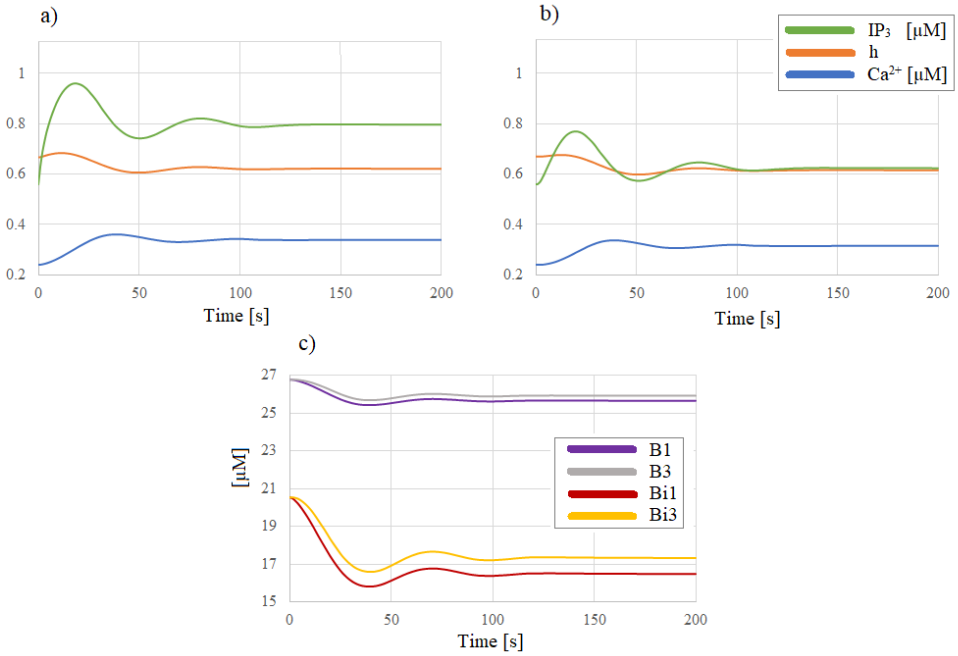

Figure 15. *Results from Skupin et al. (2010) buffering model implemented in De Pittà et al. (2009). In plots **a)** and **b)** are represented the Ca^{2+} concentration in the blue line, IP_3 concentration with a green line, and the orange line is the value of h parameter; for probe 1 in **a)** and probe 3 in **b)**. Rectangular geometry of 80µm length and 1µm width, under the same stimulus as all the simulation, is this thesis was used. Finally, in plot **c)**, it is represented the buffer parameter "B" and "Bi", that matches the concentration of buffer associated with the Ca^{2+} in Skupin et al. 2010 model, for the mobile and immobile buffers respectively. Purple and red line for the measurement in probe 1, and grey and yellow for probe 3.*

4.3.4 Buffering model by Savchenko *et al.* (2018)

Finally, the last buffer model tested was the one used in Savchenko *et al.* (2018). Even though in his study they were using De Pittà *et al.* (2009) equations under the IP_3 - Ca^{2+} dynamics, parameters that they used for the buffering equation does not fit our model correctly, as shown in Figure 16. It is possible to observe the behavior of the buffer with the blinding and unblinding phenomena because it cut down all the Ca^{2+} dynamics in our model.

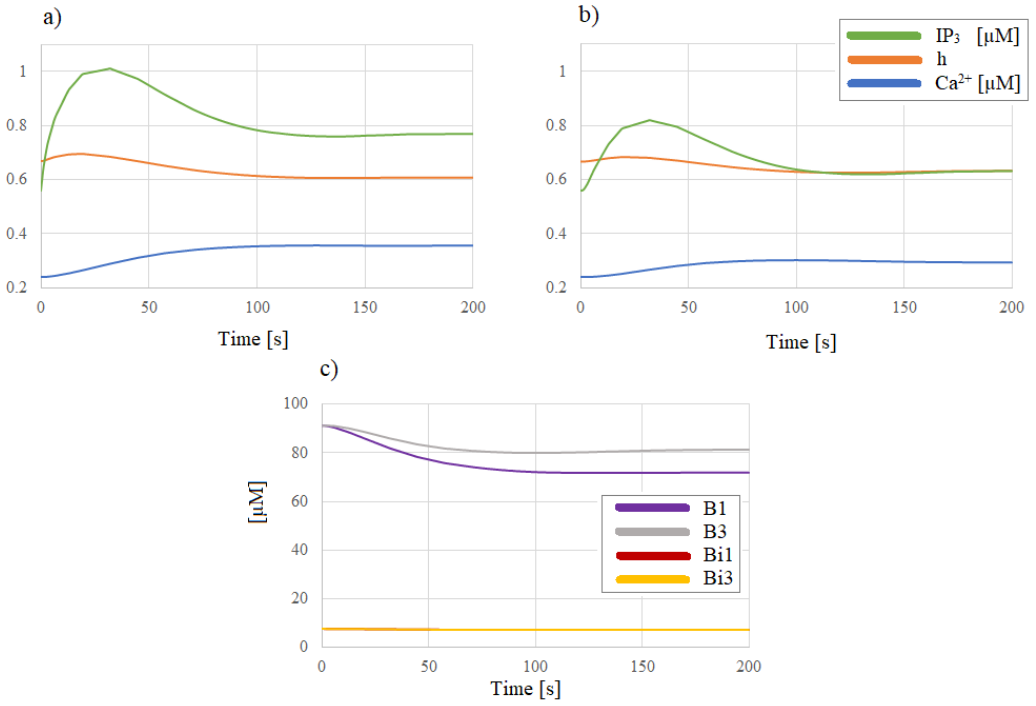

Figure 16. *Results from Savchenko et al. (2018) buffering model implemented in De Pittà et al. (2009). In plots **a)** and **b)** are represented the Ca^{2+} concentration in the blue line, IP_3 concentration with a green line, and the orange line is the value of h parameter; for probe 1 in **a)** and probe 3 in **b)**. Rectangular geometry of 80µm length and 1µm width, under the same stimulus as all the simulation, is this thesis was used. Finally, in plot **c)**, it is represented the buffer parameter "B" and "Bi", that matches the concentration of buffer associated with the Ca^{2+} in Savchenko et al. (2018) model, for the mobile and immobile buffers respectively. Purple and red line for the measurement in probe 1, and grey and yellow for probe 3.*

4.4 Statistical Analysis

After checking the possibility of representative trending lines in the data, it is essential to correlate our result with the morphology changes in the geometries; for this reason, a multiple linear regression analysis of the parametric sweep in geometry 1 and geometry 2 was done. Looking for linear correlations between the Ca^{2+} event frequency, average amplitude or width, with the different geometrical parameters.

4.4.1 Differences between simulations, ANOVA test

First, it was studied if there was any difference in the means of the results from geometry 1 and geometry 2, also between the different simulations in geometry 2. For this, the procedure was to analyze the frequency of the Ca^{2+} event. Ca^{2+} frequency presents a serious relation with the area of the geometry, as the different simulations had values of areas that are not present in all of them, Figure 17. The data was taken where areas ranged from 90μm^2 to 190μm^2 that were values found in every simulation. Also, as the sweep in the parametric simulations had a constant distance between every parameter of the simulation, the results were equidistantly distributed in these areas, and it makes it a representative measurement and comparison between the means distribution of the models.

Then a boxplot of the values for the different groups was done in Figure 18; in this case, there are 3 groups to study (*R* - Simulations run in the rectangular geometry (geometry 1), *A* - Bifurcation geometry (geometry 2) with the main process length change. *B* - Geometry 2 with the subprocess length change; and tested if there were significant differences between their means and dispersion.

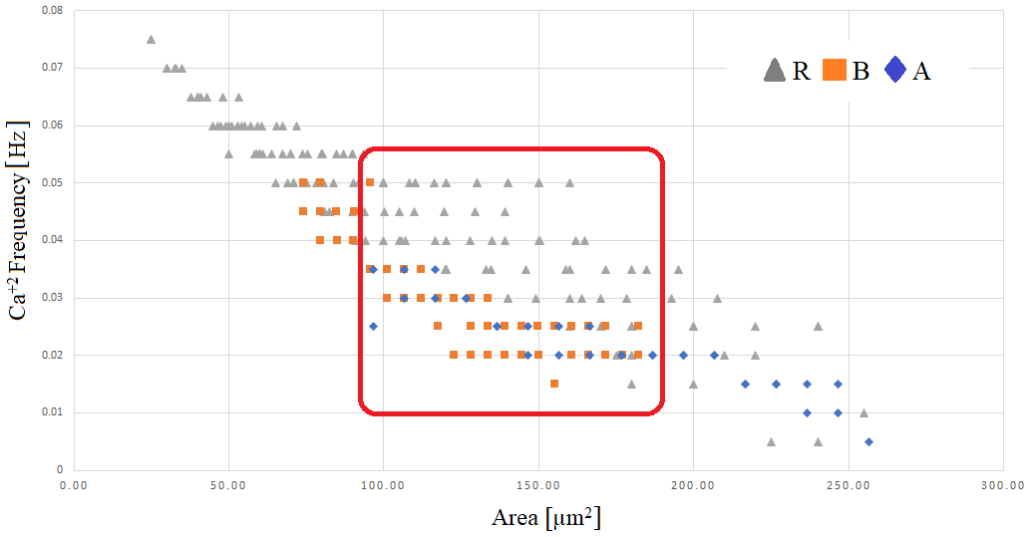

Figure 17. *Results from all the simulations, separated into 3 groups. Simulations run in the rectangular geometry (geometry 1) are represented with a grey triangle (R). In the astrocyte bifurcation geometry (geometry 2) with the process, length change is represented by a blue circle (A). Geometry 2 with the subprocess length change is represented by an orange square marker (B). A red square encompassed the points that will be used for the comparisons.*

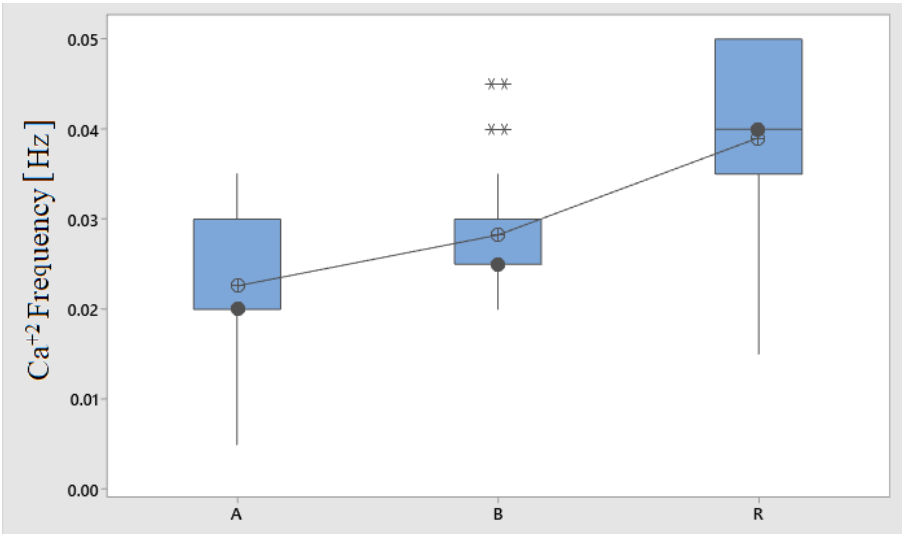

Figure 18. *Boxplot of the three different groups A, B, R (Rectangular geometry (R), astrocyte bifurcation geometry (geometry 2) with the process length change (A), and bifurcation geometry with the subprocess length change (B)). The graph represents the values of dispersion, median, mean for the frequency, and rare values of the Ca^{2+} event frequency recorded in Probe 3.*

It is possible to see differences between the three different groups and its Ca^{2+} frequency values, but as it is also possible to see some values as shared between the groups, Figure 18. For proving that the A, B, R groups are statistically different or not, an ANOVA test was done.

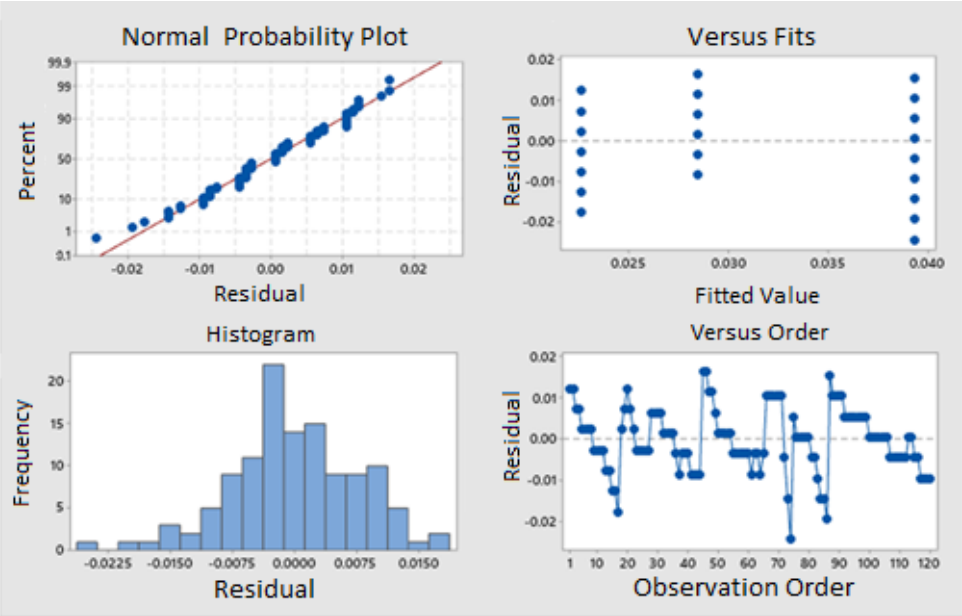

Figure 19. *Minitab 19 residual analysis of ANOVA test for the frequency of the Ca^{2+} event.*

Taking a look in Figure 19 the upper left corner plot represented the Normal probability graphic with the percent of the standardized residuals. In most of the cases the data was close to the trending line, which represents the normal distribution. In the two graphics on the right side of the figure, it was possible to check the constant variance and independence of the data. Values were clustered at both sides of the zero line with similar dispersion, and they did not follow a pattern.

Table 9. *Variance analysis for ANOVA residuals.*

Source	**DF[1]**	**Adj SS[2]**	**Adj MS[3]**	**F_vaule[4]**	**p_value[5]**
Group	2	0.005857	0.002928	48.08	0.000
Error	117	0.007127	0.000061		
Total	119	0.012983			

[1] DF : degrees of freedom
[2] Adj SS : adjusted sums of squares
[3] Ad MS: adjusted mean squares
[4] F_value: statistic test to determine whether the term is associated with the response
[5] p_value: probability that measures the evidence against the null hypothesis

Table 10. *Means analysis in ANOVA test.*

Group	N[6]	Mean	StDev[7]	95% CI[8]
A	27	0.02259	0.00764	(0.01962; 0.02557)
B	38	0.02842	0.00679	(0.02591; 0.03093)
R	55	0.03936	0.00850	(0.03728; 0.04145)

The clustered standard deviation from the ANOVA analysis was 0.0078045. In Table 9, it is possible to observe the variance analysis for ANOVA residuals, focusing in the p_value which is <0.05, the residual analysis confirms that there is at least one significative difference between the three clustered groups: A, B, R (Rectangular geometry (R), astrocyte bifurcation geometry (geometry 2) with the process length change (A) and bifurcation geometry with the subprocess length change (B). In Table 10 the mean for the Ca^{2+} frequency, its Confidence Interval, and the standard deviation were analyzed in the three groups. Deviation in the rectangular geometry is significative higher that in the bifurcation geometry, and the simulations with the main process length change contain higher deviation than the one with the subprocess change even though this one had one more stimulus configuration and the number of samples is higher (N) (Table 10).

This gives the conclusion that the effect of shape changes in the geometry brings high variability to the values in the Ca^{2+} frequency, even though they are evaluated under the same domain area, and the more significant are the shape changes, the bigger dispersion will be found in the Ca^{2+} frequency. Moreover, the three clustered groups (A, B, R) do not share any value for their Confidence Interval (95%) in the means, which is already suggesting that they are significative different between each other. This will be confirmed after the Tukey's range test, which is a test statically adapted to answer this question and will compare the mean and data distribution between all the groups.

[6] N: sample size
[7] StDev: standard deviation
[8] CI: confidence intervals

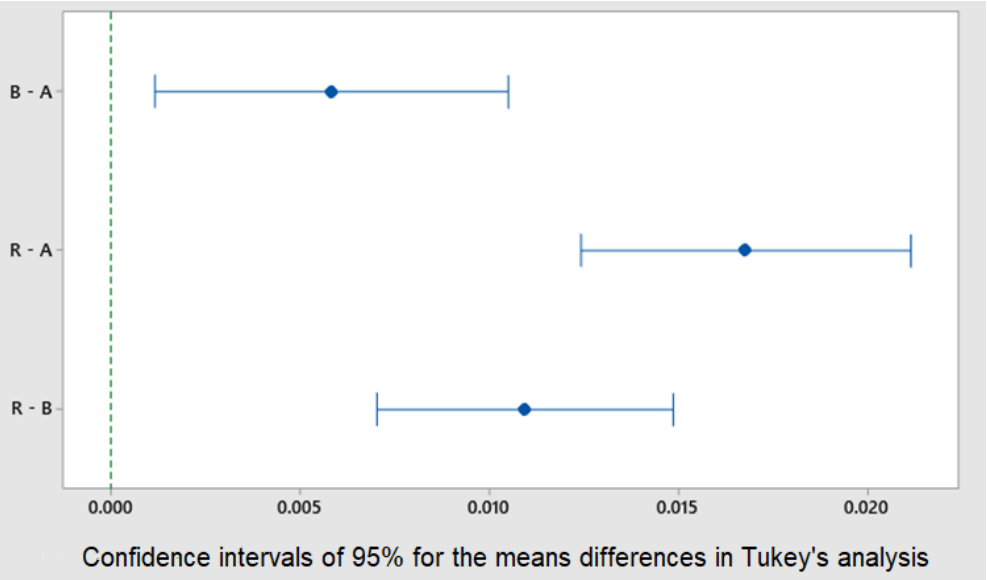

Figure 20. *Means differences with confidence intervals of 95% with the Tukey method for the frequency of the Ca2+ event in the 3 groups of study. Rectangular geometry (geometry 1, R). In the astrocyte bifurcation geometry (geometry 2) with the process length change (A). Geometry 2 with the subprocess length change (B).*

Tukey's range test did not contain the 0 in its interval, which means that there were significant differences in their means, taking into account the dispersion of the data (Figure 20).

Table 11. *Minitab Tukey's range test result for the means in R, B, A.*

Group	N	Mean	Clusters		
R	55	0.03936	A		
B	38	0.02842		B	
A	27	0.02259			C

The means that not share the same cluster letter after Tukey's range test will be treated as significantly different (Table 11). Finally, as there were significant differences between the three simulations, I will be needed at least three different linear regression analyses, one for each group.

Inside simulations in geometry 2, there were different stimulus configurations, two for the body length sweep and three for the process's length sweep. It is important to study if there were differences between the simulations, or they could be assumed with the same behavior and study them with only one linear regression.

Main process length change in bifurcation geometry.

After knowing that there were different stimulus configurations, two for the body length sweep and three for the process's length sweep, it was essential to check if the stimulus position affects the model and another ANOVA test to the results in the two stimulus positions obtained in Probe 3 was done.

After the ANOVA test, we obtained a p_value of 0.972 > 0.05 in the variance analysis and the 0 value in the Tukey's range test, among other indicators that confirm that the two configuration does not present enough differences in their Ca^{2+} frequency values to be considered significative different. Results for the ANOVA test done here can be found in the appendix section (Table A2 – A4, Figure A1 - A3). Both stimulus configurations can be assumed with the same behavior and will be studied with only one linear regression.

Subprocess length change in bifurcation geometry

The Ca^{2+} frequency values for the three stimulus positions obtained in Probe 3 in the subprocess length change will be analyzed thought an ANOVA test, results from the ANOVA test with Minitab19 can be consulted in the appendix section (Table A5 – A7, Figure A4). Stimulus position "1" refers to the model where the stimulus area was located in one of the subprocesses, and the opposite one is growing its length, stimulus position "2" refers to the model where the synaptic area was distributed by the two subprocesses, and stimulus position "3" is the one where the synaptic area was located in the subprocess that changed its length.

As happened with the stimulus configuration in the main process length change in the bifurcation geometry, here, the three stimulus configurations do not present significative differences between them for the Ca^{2+} frequency. They will be assumed with the same behavior and studied with only one linear regression

4.4.2 Regression analysis

Rectangular geometry

The first step in the regression analysis was looking into the matrix that correlates all our study variables (Figure 21). In the case of Geometry 1, geometrical parameters were divided between answer variables (studied parameters): Ca^{2+} peaks frequency, Ca^{2+} average amplitude, Ca^{2+} average FWHM; And continuous predictors that were the length,

width, and area of the geometry. Two hundred twelve simulations were run for the analysis of geometry 1, and only values in probe 3 are going to be studied as the location of probe 3 corresponds with a possible system output.

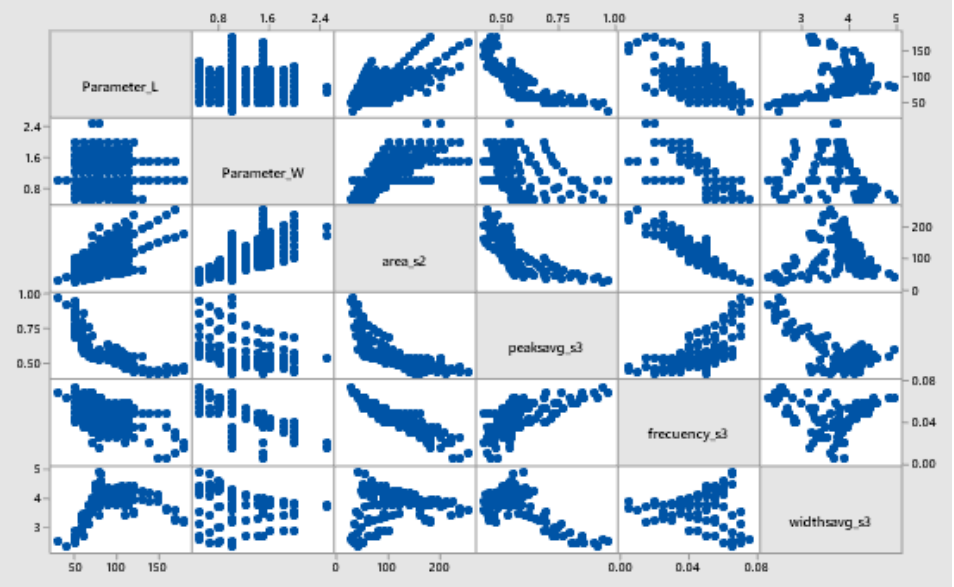

Figure 21. *Matrix graph of the different possible relations between the parameters in simulations for geometry 1.*

Then, it is necessary to do a Pearson's correlation analysis of the parameters and make a first sight of the possible relations between them. Table 12 shows strong relations between the answer variables and the continuous predictors, with values of -0.9 between the area and the frequency of the calcium event, among others.

Table 12. *Pearson's correlations table*

	L	**W**	**area**	**amplitude**	**frequency**
W	-0.034				
area	0.630	0.726			
amplitude	-0.759	-0.333	-0.720		
frequency	-0.478	-0.801	-0.917	0.622	
FWHM	0.434	-0.135	0.143	-0.722	-0.067

After perceiving possible good correlations between the answer variables and the continuous predictors, we will proceed to analyze the variance inflation factor (VIF) in Table

13 for the linear regression between the Ca^{2+} frequency and the continuous predictors. VIF with values higher than 10, indicates multicollinearity problems.

Table 13. *Linear Regression coefficients for three parameters (L, W, area) multiple linear regression analysis.*

Parameter	Coef[9]	SE Coef[10]	t_value	p_value	VIF
Constante	2.261	0.403	5.61	0.000	
L	0.01905	0.00444	4.29	0.000	10.83
W	0.689	0.330	2.09	0.038	13.79
area	-0.0097	0.00369	-2.63	0.009	22.85

In the case of the Best Subsets Regression analysis of peaks frequency, amplitude and FWHM, the best subgroup was the one made by two variables (*L, W*) (Table 14). However, in the case of the width, the prediction potential is very low, smaller than 20% (Appendix Table A8 – A9, Figure A5). When it happens, it means that the study variable cannot be analyzed thought a multiple linear regression, at least, with this prediction variables and data. For the average amplitude of the calcium event, the regression equation presents a bigger prediction potential, around 68% (Table A10 – 12, Figure A6). Nevertheless, the Ca^{2+} frequency is the parameter that was described better by the multiple regression analysis and presented more significant relations with the geometrical changes; for this reason, this study will focus on it.

Table 14. *Best subgroups linear regression analysis in the Ca^{2+} frequency.*

Vars	R^2	R^2(adjust)	R^2 (pred.)	Cp Malows	L	W	area
1	84.1	84.0	83.6	76.8			X
1	64.1	63.8	63.3	352.2		X	
2	89.7	89.5	89.0	2.7	X	X	
2	88.0	87.8	87.2	26.0		X	X
3	89.7	89.5	88.7	4.0	X	X	X

[9] Coef: coefficient

[10] SE Coef: standard error of the coefficient

After testing the best subgroups, it has been preceded to make a multiple linear regression of the one that describes better the study variable, in this case, was the two parameters one, made by the length parameter (*L*) and the width (*W*) parameter.

Frequency model in the rectangular geometry

In a multiple linear regression, it is fundamental to check that the model meets the conditions for the analysis:

- Data used in the study must be normally distributed in its majority.
- Independence of cases (the sample cases must be independent of each other in its majority).
- Homogeneity of variance (variance between the groups must be approximately equal). (Solutions, 2013)

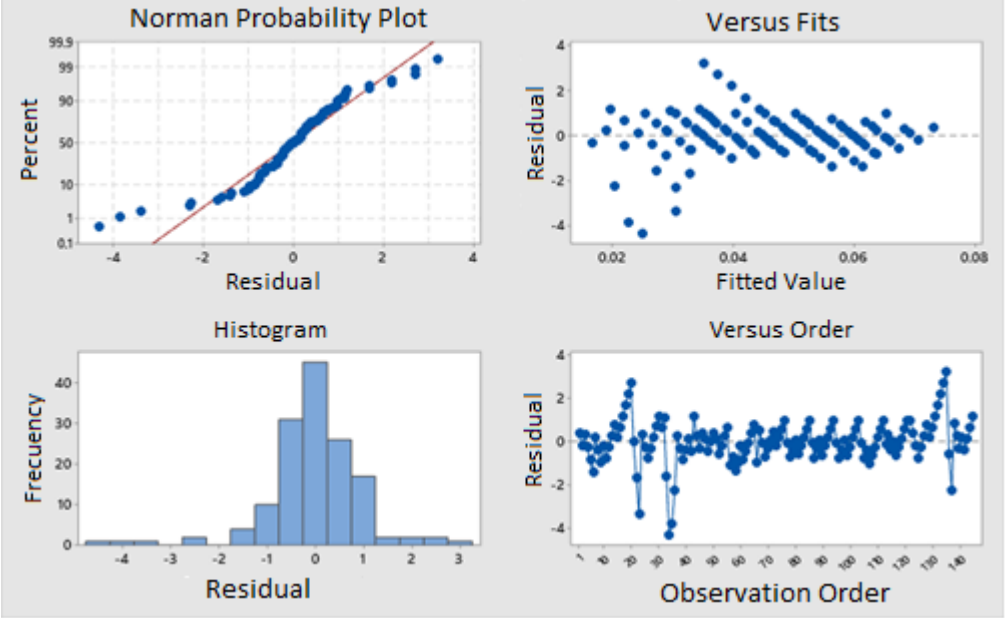

Figure 22. *Residual analysis for the multiple linear regression in the frequency of the Ca^{2+} event in geometry 1.*

Takin a look in Figure 22, the upper left corner plot represent the Normal probability graphic with the percent of the standardized residuals, it was possible to appreciate that in most of the cases the figure was close to the trending line, but extreme cases did not let assume normality with more than a 95% of accuracy after testing it with the standardized residuals in an Anderson-Darling normality test. Even though checking the nature of the problem and due to the number of cases analyzed is high, it has been taken a normality assumption, also taking a look in the lower-left subfigure is possible to assume a normal shaped graphic in the frequency of the residual. In the two graphics on the right

side of the figure, it was possible to observe values clustered at both sides of the cero line with similar dispersion, and they do not follow a known pattern; therefore, we assumed constant variance and independence of the data.

Table 15. *Multiple linear regression coefficients*

Term.	Coef	SE Coef[11]	T_value	p_value	VIF
Constante	0.09724	0.00158	61.65	0.000	
Parameter_L	-0.00023	0.000012	-18.77	0.000	1.00
Parameter_W	-0.0248	0.000818	-30.33	0.000	1.00

In Table 15, each VIF of every variable was < 10; it has been possible to assume that there were no multicollinearity problems.

Table 16. *Multiple linear regression, analysis of the variance*

Source	DF	Adj SS	Adj MS	F_vaule	p_value
Regression	2	0.027439	0.013720	617.41	0.000
Parameter_L	1	0.007828	0.007828	352.27	0.000
Parameter_W	1	0.020445	0.020445	920.04	0.000
Error	142	0.003155	0.000022		
Adjust Error	120	0.002993	0.000025	3.38	0.001
Pure Error	22	0.000162	0.000007		
Total	144	0.030595			

After the variance analysis table, it was possible to comment on the significance of the model and the individual significance of the coefficients from the regression variables that appear in the model.

For global significance, Minitab 19.1 calculates a p-value < 0.05 (Table 16). This p-value is the result of a test where the null hypothesis is that all the coefficients of the predicting

[11] SE Coef: standard error of the coefficient

variables are 0, which is the same that any predicting variable has a linear relation with the answer variable. Moreover, the alternative hypothesis is that at least one of the predicting coefficients is different to 0, and at least one of the variables has a linear relation with the frequency of the Ca^{2+} event. As p-values are smaller than 0.05, the null hypothesis is rejected, and the alternative one is accepted (Eddison, J., 2000).

In Table 17 is assumed a representative correlation of the regression model and the results obtained from the simulations, with a significative prediction power (R^2 (pred)). This prediction power was calculated by the Minitab 19 program, doing and elimination of singular points from the data and trying to predict them by the regression equation.

Table 17. *Multiple linear regression, model summary*

S	R^2	R^2 (adjust)	R^2 (pred)
0.0047139	89.69%	89.54%	88.96%

Finally, the width (W) and the length (L) of the process can relate to the calcium frequency by equation 43, with a prediction potential (R^2 (pred)) for the equation of 88.96% (Table 17).

Regression equation

$$Ca^{2+} frequency\ (probe\ 3) = 0.09724 - 0.00023 * L - 0.0248 * W \quad (43)$$

Amplitude model in the rectangular geometry

The same procedure was done for the amplitude of the Ca^{2+} frequency. The multiple linear regression can predict it on this geometry in a two-parameter regression model, and the prediction potential of this equation is 68.85%.

Table 18. *Multiple linear regression, model summary*

S	R^2.	R^2 (adjust)	R^2 (pred)
0.0660875	70.51%	70.10%	68.85%

Regression equation.

$$Ca^{2+} concentration\ (probe\ 3) = 0.09503 - 0.002949 * L - 0.0904 * W \quad (44)$$

Bifurcation geometry

Remembering that there were two different geometrical changes inside geometry 2. The first one was the main process length change, with two different stimulus positions, the second ones were the simulations where the length of one subprocess was changing and three different options for the synaptic position. All the results are obtained from probe 3, the one located at the end of the main astrocyte process.

Main process length change in the bifurcation geometry

The first step as before was to take a look at the relations matrix (Figure 23).

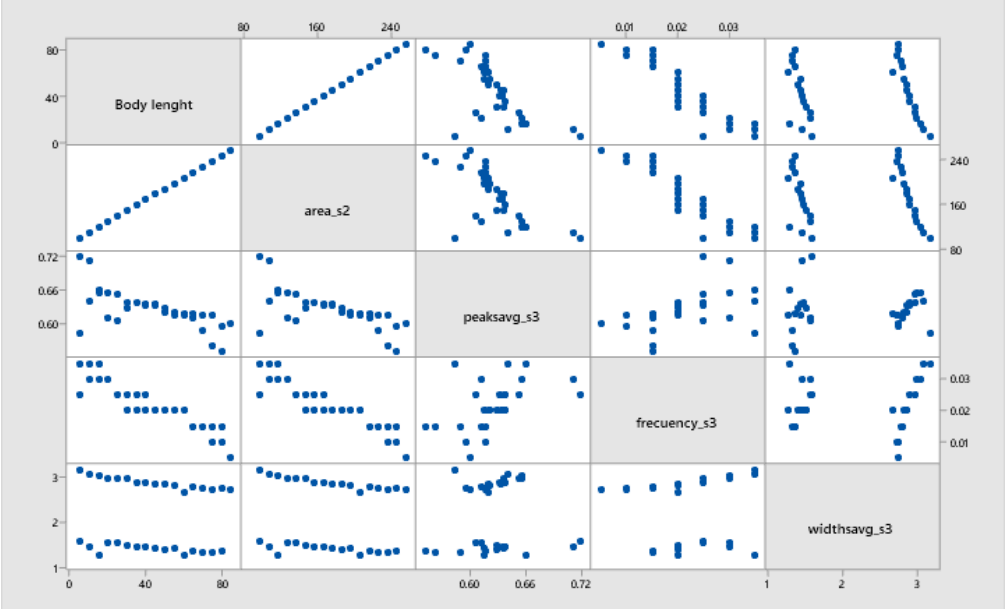

Figure 23. *Matrix graphic of the different possible relations between the parameters in geometry 2 simulations with a body length parametric sweep.*

In Figure 23, the area of the geometry and the body length parameter was directly correlated, both compute as the same parameter and affect the same the study parameters (frequency of the Ca^{2+} event, width, and amplitude). It was possible so see certain linear relation between the area and the frequency of the event, less significant with the amplitude and nonexistent with the width.

Finally, as the stimulus positions did not affect our model significantly, only one linear regression analysis that relates the area with the different study variables for this geometry was done. A Pearson's analysis has been done first to check which variables have a linear relation with the area changes, and in this case, a simple linear regression will have a good potential for describing the Ca^{2+} frequency.

Table 19. *Pearson's correlations table*

	area_s2	peaksavg_s3	frecuency_s3
peaksavg_s3	-0.667		
frequency_s3	-0.921	0.489	
widthsavg_s3	-0.078	0.034	0.106

As it is shown in Table 19, the area could have good predictive power for the Ca^{2+} frequency event due to its high Pearson coefficient close to -1, while it has not a very good linear relation with the width and the peak amplitude. After doing a linear regression with these parameters, the prediction power of the trending lines is less than 50% in the case of the Ca^{2+} full-width at half-maximum and average amplitude (Appendix Table A14 and A17). Finally, only the relationship with the frequency will be shown in the results (Figure 24).

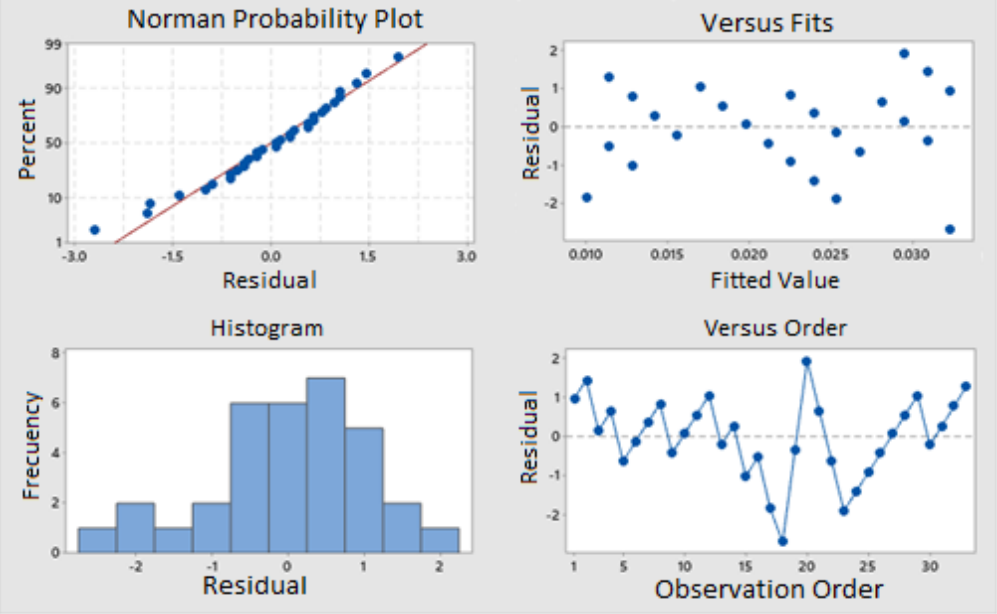

Figure 24. *Residual analysis for multiple linear regression of frequency of the Ca^{2+} event in geometry 2 in the body length changing simulation.*

Residual analysis confirms that the regression meets the conditions for the analysis (Figure 24). Coefficients and VIF analysis in Table 20.

Table 20. *Multiple linear regression coefficients*

Parameter	Coef	SE Coef.	t_value	p_value	VIF
Constant	0.04585	0.000504	42.65	0.000	
area_s2	-0.00014	0.000512	-13.20	0.000	1.00

Table 21. *Multiple linear regression model summary*

S	R^2	R^2 (adjust)	R^2 (pred)
0.0028977	84.90%	84.42%	82.20%

In this analysis, using only the shape and the area, it is possible to have a prediction potential of 82%, with equation 45, for the Ca^{2+} frequency (Table 21).

Regression equation

$$Ca^{2+}(Hz) = 0.04585 - 0.00014 * area\ (geometry\ 2\ process\ L\ change) \quad (45)$$

Subprocess length change in the bifurcation geometry

After the results of the ANOVA test, it was possible to confirm that there were significant differences in the average value of the Ca^{2+} frequency for the two different simulations; group A was the main process length change and group B where a single subprocess length was changing. There were no significant differences in the result between the three synaptic positions, and as before, the area is the best parameter for describing the Ca^{2+} frequency response of the model. With this, another linear regression analysis as before has been done in this geometry (Figure 29, Table 22-24). This new linear regression model will predict the Ca^{2+} frequency in Probe 3, having as prediction variable the area of the domain, and the data that was used were the results obtained in Probe 3 for the subprocess length change in the bifurcation geometry.

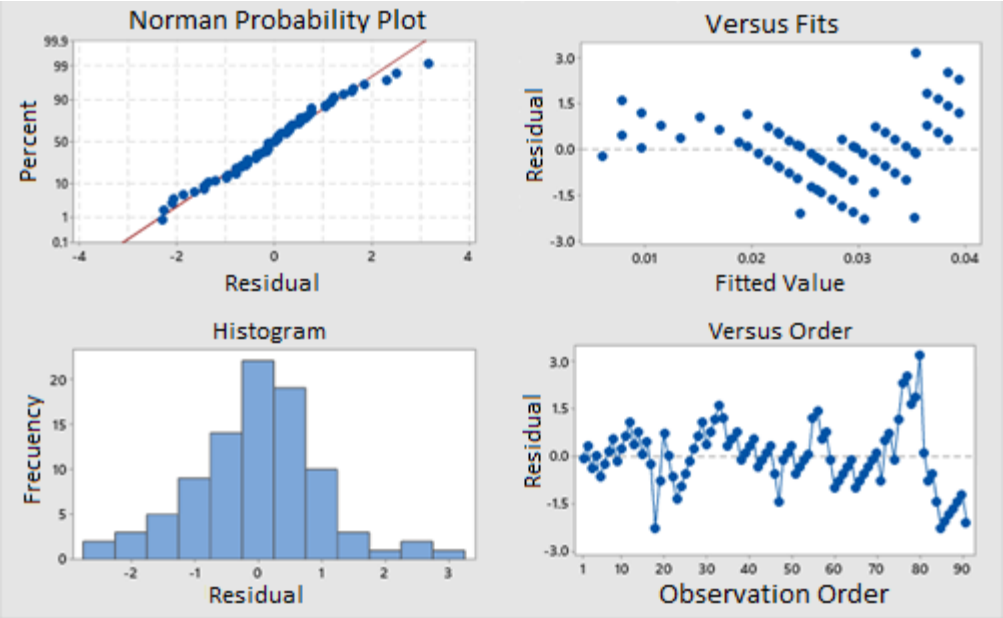

Figure 25. *Residual analysis for multiple linear regression of frequency of the Ca^{2+} event in geometry 2 in the single process length change simulation.*

Table 22. *Multiple linear regression coefficients*

Parameter	Coef	SE Coef.	t_value	p_value	VIF
Constante	0.0502	0.000486	55.37	0.000	
area_s2	-0.000183	0.000489	-16.94	0.000	1.00

Table 23. *Multiple linear regression, analysis of the variance*

Source	GL	SC Adjust	MC Adjust	F_vaule	p_value
Regresión	1	0.006174	0.006174	287.00	0.000
area_s2	1	0.006174	0.006174	287.00	0.000
Error	89	0.001915	0.000022		
Ajust. error	51	0.001640	0.000032	4.44	0.000
Pure error	38	0.000275	0.000007		
Total	90	0.008088			

Regression equation.

$$Ca^{2+}(Hz) = 0.0502 - 0.000183 \\ * area\ (geometry\ 2\ subprocess\ L\ change) \quad (46)$$

Table 24. *Multiple linear regression model summary*

S	R^2	R^2 (adjust)	R^2 (pred)
0.0046381	76.33%	76.06%	75.17%

5. DISCUSSION

Converting the mathematical model by De Pittà *et al.* (2009) to a FEM model implemented in COMSOL Multiphysics 5.4 and introducing the diffusion coefficient of the different molecules makes our model behave differently than the original one. Furthermore, it allows us to study the diffusion within a well-defined geometry, hence increasing the complexity of the study, thus moving one step closer to the reality of the cell.

The model presented by De Pittà *et al.* (2009) was run with a rectangular 60 seconds pulse of glutamate stimulus, and it showed a stationary response after some fluctuations inside this 60s. After introducing the diffusion coefficient of the molecules and implementing the model in a FEM model including geometry and astrocyte dimensions, the behavior of the calcium (Ca^{2+}) changes presenting a pulsatile behavior. Experiments showed that Ca^{2+} wave often has a pulsatile behavior, characterized by the frequency of the Ca^{2+} event. (Wu *et al.*, 2019). Looking at the amplitude and values of the concentration of the different molecules, it shows great similarities in the general behavior of the system, as it can be seen on Figure 5.

Figure 5 shows, in several probes, how the production and degradation of inositol 1,4,5-trisphosphate (IP_3) leads to the Ca^{2+} release from the endoplasmic reticulum (ER) and control the gating variable *h*. Finally, the system controls itself, degrading the IP_3, gathering up the Ca^{2+} back into the ER, and re-starting the circle as the stimulus is always constant in our simulations. This process fits the behavior described by the original model De Pittà *et al.* (2009) and the literature about the intracellular release of Ca^{2+} from the ER due to the stimulation of metabotropic glutamate receptors (mGluRs) and IP_3 production and degradation (Communi *et al.*, 2001; Verkhratsky and Butt, 2013; Guerra-Gomes *et al.*, 2018).

Furthermore, trying to compare our study and results with more recent astrocyte models, is not trivial. Reason being every model proposed in a paper runs under the conditions inherent to that particular study. In order to directly compare two different systems, it is essential so simulate them under the same conditions, for results to be compared. Even though, as there will be explained later on, our model, with its simple relative complexity, can explain phenomena studied in other models and be compared with results in the experimentation done in other published studies.

5.1 Geometry 1: Rectangular geometry

From the result shown in Figure 6, it is possible to identify different behaviors between the geometries with three different widths. Having a thicker process results generally in a lower frequency in the Ca^{2+} event. It is also possible to identify differences between the probe located next to the stimulus area (Probe 1) and the one on the opposite side of the geometry (Probe 3). This shows the effect of the propagation speed of the Ca^{2+} wave. These differences are very visible in the 1 μm width geometry, where there is a continuous Ca^{2+} frequency in Probe 1 next to the glutamate stimulus area for all the lengths larger than 60 μm, and Ca^{2+} frequency decrease in Probe 3 which is distancing from the stimulus. It is the last Ca^{2+} wave does not reach Probe 3 in time to be calculated by the program in lengths larger than 100 μm; this phenomenon was possible to be appreciated in the simulation videos.

With lengths larger than 160 μm, not all the Ca^{2+} waves that are produced travel the same length, and some are not able to travel such long distances; even though, the stimulus was constant during all the simulations. The capability of the Ca^{2+} wave to propagate large distances has more relation with the IP_3 production and degradation through the geometry than the diffusion potential of Ca^{2+}; this effect is more visible and explained on the discussion of the results extracted from the bifurcation geometry. One conclusion that can be drawn from the results is that the average amplitude and average full width at half-maximum (FWHM) of the Ca^{2+} wave does not depend on the width of the process. Still, it depends on the length of the process and also on the position of the measuring probe in the case of the average amplitude of the Ca^{2+} concentration, this simulation shows clear differences between probe 1 and 3. The amplitude of the Ca^{2+} wave concentration decrease with the distance from the stimulus position.

The behavior of the average FWHM of the Ca^{2+} wave cannot be explained by any of the parameters used in this study at first sight in Figure 6; neither it is possible to explain it through a multiple linear regression with the parameters used in this study, as it was analyzed in the Appendix “Regression analysis of the Ca^{2+} width at half-maximum” with p_values > 0.05 in the variance analysis (Table A8) and a prediction potential of 15.6% (Table A9).

Finally, in Figure 7, it is possible to see different Ca^{2+} frequency values from the three different widths under the same area, which highlights the effect of the domain shape on the Ca2+ event frequency. There are significantly higher Ca^{2+} frequency values in narrow processes than in the wider ones.

Taking a look into the results extracted from the stimulus area morphology test; we can conclude that, the stimulus area morphology does not affect the Ca^{2+} behavior in our model significantly, for large diffusion areas. The stimulus domain morphology is not directly related to the Ca^{2+} release, but it is with the IP_3 production, as its diffusion coefficient is ten times bigger than the diffusion of the Ca^{2+}. The effect of the shape of the stimulus and early production of IP_3 do not contribute to make big differences between the simulations, with geometries wider than 1 μm. Notwithstanding, it is important to highlight that it can affect the Ca^{2+} frequency in geometries were the stimulus area represented between the 7 - 16%; in these cases, the differences were present in Probe 3. These changes can come from the fact that the distance to the centroid of the stimulus area, divided by the whole domain area was very different between the simulations at this geometrical configuration. This affirmation could be inaccurate as the differences are not so clear in Probe 2, as we will confirm later, the propagation of the Ca^{2+} wave is not a diffusion problem at all, and more simulations focused in the glutamate stimulus without changing the astrocyte geometry should be taken into account to describe accurately how the stimulus morphology could affect our system output.

Studying how the centroid position of the stimulation domain could affect the results was not a topic deeply investigated in this thesis and need more future work on it. However, it would be interesting to study if it can be used as a prediction variable from the system and if it could give us some clues about the general Ca^{2+} behavior in astrocytes. The fact that the shape of the stimulus area could or not affect the Ca^{2+} dynamics does not say that the area of the stimulus does not affect. The bigger the stimulus area, the bigger the early production of IP_3, which strongly affects the Ca^{2+} dynamics, but it was neither evaluated in this study, and these questions leave promising research lines open for upcoming master's students that would like to continue researching in this topic.

5.1.1 Maximum propagation distance

From the results shown in Figure 9, it is possible to evaluate the maximum distance that a Ca^{2+} wave can travel through a process under specified conditions and relate it with the width of the process. The narrow process can keep the Ca^{2+} traveling long distances (up to 180μm), and the propagation distance is reduced with the thickening of the process. In narrow areas the diffusion takes mainly the direction towards the long axis, as well the early production of IP_3 rises its concentration faster than in wider ones.

Furthermore, Figure 9 makes it possible to categorize the widths that would be able to propagate the Ca^{2+} through all the processes with an already known length and which

widths would be too wide for generating a successful Ca^{2+} event able to reach Probe 3. These results generate an approximate boundary, which is the line presented in Figure 9, connecting the simulation results. Geometries that are not able to propagate the Ca^{2+} wave through all the domain are located above the line. This result could be useful to categorize which hypertrophied processes with an already known stimulation will be able to propagate or not the Ca^{2+} event through them.

5.1.2 Statistical analysis in the rectangular geometry

Trying to understand the behavior of the Ca^{2+} dynamics in the proposed rectangular geometry and provide a conclusion and statistical support, a regression analysis was done for the simulations run in this geometry. Regression analysis is an efficient procedure when one tries to understand how much the prediction parameters affect the answer variable. From the results, the Ca^{2+} frequency is the variable being more affected by the geometrical changes, and the one that is explained better by the regression analysis.

Starting with the regression analysis done to the Ca^{2+} frequency in geometry 1, the width (W) and the length (L) of the process can be connected with the Ca^{2+} frequency by equation 43. The prediction potential for equation 43 is 89%. When the prediction potential is close to 100%, the regression analysis suggests how much these parameters are defining the answer variable and how strong is the relation between them is. Also, it is important to examine how significant is the effect of the width of a swollen astrocyte process is, as it might be in Alzheimer's disease. Increasing 1μm in length reduces the Ca^{2+} frequency by 0.00023 Hz, and 1μm in width reduces it by 0.024 Hz. Therefore, the effect of the width of a process is 100 times bigger than the length regarding to the Ca^{2+} frequency.

The effect of the thickening of a process was evidenced before in Wu *et al.* (2019), where they contrasted the effect of the thickening of processes in the frequency of the Ca^{2+} events. The effect of growing 1μm reduced the frequency around 0.02Hz in the computational model and also in the experiments, which makes this thesis result reasonable.

5.2 Geometry 2: Bifurcation geometry

5.2.1 Angle test

As it is possible to observe in Figure 10, the angle between the subprocesses does not affect the Ca^{2+} events in our model. Modifying the angle does not generate significant variations on the frequency, average amplitude, or average FWHM of Ca^{2+} events. The cause of the small variation appreciable in angles between 50º – 150º is explained in more detail in the results and it came from a small variation in the thickening of the subprocesses due to the configuration of the geometry. This variation can increase the thickness of the process in the bifurcation side $\sqrt{2}$ times between these angles (following the geometrical configuration of the model, Table 7), it could be reflected in a decrease of the Ca^{2+} frequency around 0.0016 Hz in most extreme cases (following the results in the regression analysis in the rectangular geometry), and fits the variations showed in Figure 10b left. It would have been possible to look for a triangular configuration where the hypotenuse in the bifurcation would be reoriented in every angle, and we would have avoided these small changes in the thickness, however other geometrical configurations that were tested generated bigger area differences and convergence problems.

The effect of the angle is very significant in fluidics simulation due to the kinetic energy of a fluid mass that travels, its inertial forces and its interactions with the boundaries, and also is very important in electromagnetic simulations, due to the importance of the orientation of the magnetic field (Rubenstein, D. A. *et al*, (2012); Fundamentals of Magnetic Fields. (2002)). As the system being analyzed is not considering any magnetic field and any mass, the angle should not affect our model, and it is corroborated with the simulations.

Future implementation of geometries that would use the De Pittà *et al.* (2009) model cloud be simplified, saving time in computing the simulations and making the geometries.

5.2.2 Geometrical changes and statistical analysis in the bifurcation geometry

After results showed in Figure A4, it was demonstrated statistically thought an ANOVA test, that there were no significative differences in probe 3 between the distributed and not distributed stimulus in the subprocesses.

Figure 10 illustrates the effect of the shape of the local geometry, and this phenomenon is also shown in Figure 11. Differences in the Ca^{2+} frequency between probe 1 and probe 3 and similarities between data collected by the same probe in different geometries, for example, comparing the results in figures 10 and 11. These results confirm the significant importance in the location of the measuring point and, for the same reason, the geometry surrounding it.

Another important effect very present in the literature is that the Ca^{2+} wave is mainly a result of the release events associated with the opening of Ca^{2+} release channels through the endoplasmic reticulum membrane to the cytosol of the cell (Verkhratsky and Butt, 2013). This can be seen in Figure 10 and Figure 11, where not all the Ca^{2+} waves that appear, travel from probe 1 to 3, and some look like they disappear on the way. It is not a diffusion property of the Ca^{2+} or a particular way of traveling of this ion. Local cytosolic Ca^{2+} concentration has more to do with the release of Ca^{2+} from the ER stores and depends strongly on the geometry surrounding the measuring point than on the diffusion of the Ca^{2+} ion. This effect can be seen in Figure 10 on probe 1, with the not distributed stimulus area at 40 µm of main process length, the frequency of the Ca^{2+} event is around 0.045 Hz, and in probe 3 is 0.02 Hz.

Recent studies have confirmed this phenomenon where the local shape that surrounds the measuring location has big relevance in the frequency of the Ca^{2+} event. For example, the differences found between the Ca^{2+} frequency measured experimentally in subregions of the process and the one measured in the entire expanded process. Significantly higher values were recorded in the subregion measurements (Di Castro et al., 2011). Similar results are visible in the experiments comparing the frequency in the soma, processes, and end-foot, showing the highest Ca^{2+} frequency in the processes, then in the end-foot and finally very deceased in the soma (Bindocci *et al.*, 2017), which can be related directly with our result obtained from Geometry 2 with an equivalence between the subprocesses and the main process (Probe 1 and Probe 2 in Figure 11, not distributed simulation). Subprocesses in Geometry 2 presented higher Ca^{2+} frequency than the main process, thickness of the main process is twice the thickness of the subprocesses, and it is equivalent to the results found between the processes and the soma in Bindocci et al. (2017).

Furthermore, Wu *et al.* (2019) relate the frequency of the Ca^{2+} event with the volume fraction (VF) of the local geometry of the astrocyte. In their study, they found lower-frequency values in the astrocyte regions with high VF like in the soma, and higher frequencies in low VF values like in thin processes. The VF was calculated to represent the

surface-to-volume-ratio (SVR) between the different astrocyte sections inversely, as thin processes could not be seen accurately when they were recreating the 3D geometry of in-vitro astrocytes. It was calculated as the ratio between the fluorescence in the measured area and the fluorescence of the soma, under the expression of GCaMP2. These results were corroborated experimentally and computationally (Wu *et al.*, 2019). This effect fits again the results showed in Figure 10, with the reduction of the Ca^{2+} frequency from the subprocesses to the main process that has a lager VF.

Also, the result showed in Figure 11 corroborate what was said before, it is possible to appreciate the differences between probes and compare results between simulations. A statistical analysis was done, first an ANOVA test to check the possible significant differences between geometries and then a regression analysis to explain how the proposed geometrical variations in the simulation are affecting our results.

It was also possible to appreciate in the simulations run in the bifurcation with the subprocess length change, that the calcium event always started to travel from the largest subprocess, it travelled through it, and then goes to the main process and the second shorter subprocess. This behavior is not expected in a diffusion model where the stimulation in both subprocesses is the same, and it is also happening simultaneously. However, biological experimentations with astrocytes have proved that the Ca^{2+} event mostly starts from distal astrocytic processes (Nett, Oloff and Mccarthy, 2002; Asada *et al*., 2015; Bindocci *et al*., 2017). This phenomenon in the medical imaging use to be connected with the ubication of the synapses in the astrocyte's endfeet at the end of the astrocyte's processes (Di Castro *et al*., 2011); it can also be related to the distribution of the content of the cell, the allocation of the receptors, and the ER distribution in the cell among others (Arizono *et al*., 2012). As our model does not take into account the distribution of the cell organelles and the fact that both subprocesses have the same stimulus condition, this factors are removed from the equation and take sides studies that attribute this phenomenon to the geometrical configuration of the processes (Wu *et al*., 2019). Taking a look on how the model is built and the mathematical equations behind, the fact that the shorter subprocess is closer to the main process makes the diffusion area next to the stimulation zone has a general smaller SVR than the one located in a larger subprocess far from the main and thicker process. As it was evidenced in previous studies, astrocytes processes with high SVR are more likely to start the Ca^{2+} release (Wu *et al*., 2019), and it was also evidenced in our model with the calcium event always starting to travel from the larger subprocess with the most distal stimulation from a wider area, even though, both subprocesses had the same thickness.

Different geometries bring different Ca^{2+} dynamics, as it was verified with an ANOVA analysis of the Ca^{2+} frequency. It was essential to compare the Ca^{2+} frequency in the different geometries under the same area, as the diffusion principle under molecular behavior depends strongly on the diffusion space (Figure 17).

On Table 11, the ANOVA test demonstrates that Geometry 1 and Geometry 2 present significative different Ca^{2+} frequency under the same domain area, and even the two simulations inside Geometry 2 cannot get clustered together.

Looking into Figure 20, that shows the means differences with the Tukey method for the frequency of the Ca^{2+} between the three geometrical models. it is possible to see that the two different geometrical changes simulations inside Geometry 2 (B – A) are closer to the 0 value in Tukey analysis than the comparisons (R – A or R - B). This result demonstrates that more significant changes in the morphology will bring bigger differences in the Ca^{2+} frequency. Moreover, even small changes inside the same geometry (geometry changes in geometry 2, simulations B and A) are enough to present significative differences in the Ca^{2+} frequency results, and simulations inside the same geometry can be clustered together even though their stimulus configurations could be different (Figure A3, A4).

By discretizing the area and the different shapes, it is still possible to get good linear predictors of the Ca^{2+} frequency just using the area and shape as predictors, for example, in Table 21 with the linear regression analysis for the main process change in geometry 2. In this analysis, using only the shape and the area of it, it is possible to have a prediction potential of 82%, with equation 45. The fact of having different equations for every shape, and a great prediction potential in them, confirm the significant effect of the morphology in the frequency of the Ca^{2+} event in astrocytes, and its strong relation with it.

5.3 Buffer analysis

Taking a look into the buffering model's results, the Hadfield *et al.* (2013) model is the only one that can be directly fitted to the De Pittà *et al.* (2009) model with the original parameters. Nonetheless, the Hatfield *et al.* (2013) model has a very simple equation (equation 16) that was calculated to fit the experiments described in their paper. It does not reproduce the Ca^{2+} buffering phenomena with the binding–unbinding behavior. It only partially reduces the Ca^{2+} frequency and amplitude. As Hadfield *et al.* (2013) as tested in its study, the Ca^{2+} buffer does not affect the morphology of the Ca^{2+} dynamics through

time significantly. It is equivalent to add a constant ρ that multiplies and reduces the Ca^{2+} concentration. It comes from the Hadfield *et al.* (2013) buffer equation, where parameter K_d is much bigger than physiological cytosolic Ca^{2+} concentrations (Wang *et al.*, 1997). Finally, Hadfield *et al.* (2013) suggested that their buffering model could have been reduced to the following parameter multiplying the Ca^{2+} concentration, where K_d represents the buffer disassociation constant with a value of 20 μM, and B_T represents the total buffer concentration with a value of 10 μM.

$$\rho = \frac{K_d}{K_d + B_T} = \frac{2}{3} \tag{43}$$

However, Lopez-Caamal *et al.* (2014), Skupin *et al.* (2010), Komin *et al.* (2015), and Savtchenko *et al.* (2018), used derivations of the same equations (equations 17 - 25). These equations reproduce the Ca^{2+} buffering behavior, with the mobile and immobile part and the binding–unbinding phenomena. All of them use different parameters for the same equations, most of them calculated to fit their Ca^{2+} models. As they are using different astrocyte's calcium models, or modifications of the one used in this thesis, their Ca^{2+} buffering parameters do not fit our model, absorbing our intracellular Ca^{2+} disproportionately.

Notwithstanding, the study of a buffering equation that could fit the model should continue due to the importance of this phenomenon in the cell (Verkhratsky and Butt, 2013). Furthermore, most of the Ca^{2+} imaging techniques use Ca^{2+} buffers, and a model with the buffer implemented will make more accessible the validation of it and the linkage between the Ca^{2+} imaging and the computational simulations(Khakh and McCarthy, 2015). Finally, it will also be closer to represent all the biological processes under the Ca^{2+} dynamics in the cell.

6. CONCLUSION

The effect of morphology changes on the Ca^{2+} dynamics in astrocytes was already evidenced in previous publications (Khalid *et al.*, 2018). Furthermore, biology is demonstrating that pathological astrocytes present morphological changes in neuropathologies like Alzheimer's Disease. As Ca^{2+} defines most of the functional chores of astrocytes, studies that link the morphological changes to the astrocyte behaviour can be a crucial point in the understanding of many neuropathologies.

With this master's thesis, we have been able to decrypt the impact of many geometrical parameters to the intracellular Ca^{2+} behaviour in astrocytes. Parameters as the thickness of a process have demonstrated to have a crucial influence in the Ca^{2+} frequency. Furthermore, we have been able to analyse the differences between regions inside an astrocyte, and to demonstrate statistically that Ca^{2+} frequency can be clustered inside a geometrical shape and the differences between the Ca^{2+} frequency in the geometries is bigger when their shapes present greater changes. Moreover, parameters like the angle between the subprocesses does not make significant differences in the intracellular Ca^{2+} for the used model.

This study would help to simplify future models and simulations, giving the astrocyte morphology an essential role in the decryption of Ca^{2+} dynamics. Moreover, numerous paths have been open for future research, for example, to study deeply the effect of the glutamate stimulus in the model, comparing new astrocyte models, improving the buffering model, etc…

7. REFERENCES

Agulhon, C. *et al.* (2008) 'What Is the Role of Astrocyte Calcium in Neurophysiology? Glia: From Passive Glue to Excitable Cells', *Neuron*, 59(6), pp. 932–946. doi: 10.1016/j.neuron.2008.09.004 .

Alan Bloom (2010). "Chapter 8. Modulation". In H. Ward Silver; Mark J. Wilson (eds.). The ARRL Handbook for Radio Communications. American Radio Relay League. p. 8.7. ISBN 978-0-87259-146-2.

Allbritton, N. L., Meyer, T. and Stryer, L. (1992) 'Range of messenger action of calcium ion and inositol 1,4,5-trisphosphate', *Science*, 258(5089), pp. 1812–1815. doi: 10.1126/science.1465619.

Almad, A. and Maragakis, N. J. (2018) 'A stocked toolbox for understanding the role of astrocytes in disease', *Nature Reviews Neurology*. Springer US, 14(6), pp. 351–362. doi: 10.1038/s41582-018-0010-2.

Anlauf, E. and Derouiche, A. (2013) 'Glutamine Synthetase as an Astrocytic Marker: Its Cell Type and Vesicle Localization', *Frontiers in Endocrinology*, 4(2), pp. 263–271. doi: 10.3389/fendo.2013.00144.

Arizono, M. *et al.* (2012) 'Receptor-selective diffusion barrier enhances sensitivity of astrocytic processes to metabotropic glutamate receptor stimulation', *Science Signaling*, 5(218). doi: 10.1126/scisignal.2002498.

Asada, A. *et al.* (2015) 'Subtle modulation of ongoing calcium dynamics in astrocytic microdomains by sensory inputs', *Physiological Reports*, 3(10), pp. 1–11. doi: 10.14814/phy2.12454.

Bennett, M. R., Farnell, L. and Gibson, W. G. (2005) 'A quantitative model of purinergic junctional transmission of calcium waves in astrocyte networks', *Biophysical Journal*. Elsevier, 89(4), pp. 2235–2250. doi: 10.1529/biophysj.105.062968.

Bindocci, E. *et al.* (2017) 'Neuroscience: Three-dimensional Ca2+ imaging advances understanding of astrocyte biology', *Science*, 356(6339). doi: 10.1126/science.aai8185.

Brenner, M. (1994) 'Glial Fibrillary Acidic Protein (GFAP)', *Brain Pathology*, 4(3), pp. 219–220. doi: 10.1111/j.1750-3639.1994.tb00836.x.

Cahoy, J. D. *et al.* (2008) 'A transcriptome database for astrocytes, neurons, and oligodendrocytes: A new resource for understanding brain development and function', *Journal of Neuroscience*, 28(1), pp. 264–278. doi: 10.1523/JNEUROSCI.4178-07.2008.

Chander, B. S. and Chakravarthy, V. S. (2012) 'A Computational Model of Neuro-Glio-Vascular Loop Interactions', *PLoS ONE*, 7(11), pp. 1–11. doi: 10.1371/journal.pone.0048802.

Chia, T. H. and Levene, M. J. (2009) 'Microprisms for in vivo multilayer cortical imaging', *Journal of Neurophysiology*, 102(2), pp. 1310–1314. doi: 10.1152/jn.91208.2008.

Communi, D. *et al.* (2001) 'A Novel Receptor-mediated Regulation Mechanism of Type I Inositol Polyphosphate 5-Phosphatase by Calcium/Calmodulin-dependent Protein Kinase II Phosphorylation', *Journal of Biological Chemistry*, 276(42), pp. 38738–38747. doi: 10.1074/jbc.M105640200.

Computational Biophysics , nature.com; https://www.nature.com/subjects/computationa l-biophysics

De Pittà, M. *et al.* (2009) 'Glutamate regulation of calcium and IP3 oscillating and pulsating dynamics in astrocytes', *Journal of Biological Physics*, 35(4), pp. 383–411. doi: 10.1007/s10867-009-9155-y.

De Young, G. W. and Keizer, J. (1992) 'A single-pool inositol 1,4,5-trisphosphate-receptor-based model for agonist-stimulated oscillations in Ca2+ concentration', *Proceedings of the National Academy of Sciences of the United States of America*, 89(20), pp. 9895–9899. doi: 10.1073/pnas.89.20.9895.

Di Castro, M. A. *et al.* (2011) 'Local Ca2+ detection and modulation of synaptic release by astrocytes', *Nature Neuroscience*. Nature Publishing Group, 14(10), pp. 1276–1284. doi: 10.1038/nn.2929.

Dickinson, G. D. *et al.* (2016) 'Hindered cytoplasmic diffusion of inositol trisphosphate restricts its cellular range of action', *Science Signaling*, 9(453), pp. ra108–ra108. doi: 10.1126/scisignal.aag1625.

Diekman, C. O. *et al.* (2013) 'Modeling the neuroprotective role of enhanced astrocyte mitochondrial metabolism during stroke', *Biophysical Journal*. Biophysical Society, 104(8), pp. 1752–1763. doi: 10.1016/j.bpj.2013.02.025.

Donato, R. *et al.* (2012) 'Functions of S100 Proteins', *Current Molecular Medicine*, 13(1), pp. 24–57. doi: 10.2174/156652413804486214.

Eng, L. F., Ghirnikar, R. S. and Lee, Y. L. (2000) 'Glial Fibrillary Acidic Protein : GFAP-Thirty-One Years (1969 – 2000)*', 25, pp. 1439–1451.

E. M. Adler, G. J. Augustine, S. N. Duffy and P. C. Milton, Alien intracellular calcium chelators attenuate neurotransmitter release at the squid giant synapse, J. Neurosci. 1(6) (1991) 1496–1507.

Eddison, J. (2000). Quantitative Investigations in the Biosciences using MINITAB. New York: Routledge, https://doi.org/10.1201/9780203741535

Falcke, M. (2003) 'On the role of stochastic channel behavior in intracellular Ca^{2+} dynamics', *Biophysical Journal*, 84(1), pp. 42–56. doi: 10.1016/S0006-3495(03)74831-0.

Farr, H. and David, T. (2011) 'Models of neurovascular coupling via potassium and EET signalling', *Journal of Theoretical Biology*. Elsevier, 286(1), pp. 13–23. doi: 10.1016/j.jtbi.2011.07.006.

Fernandez, A. M. *et al.* (2012) 'Regulation of the phosphatase calcineurin by insulin-like growth factor i unveils a key role of astrocytes in Alzheimer's pathology', *Molecular Psychiatry*, 17(7), pp. 705–718. doi: 10.1038/mp.2011.128.

Fink, C. C. *et al.* (2000) 'An Image-Based Model of Calcium Waves in Differentiated Neuroblastoma Cells', 79(July).

Fundamentals of Magnetic Fields. (2002). Electromagnetics Explained, 51–74. doi:10.1016/b978-075067403-4/50004-5

Gibson, W. G., Farnell, L. and Bennett, M. R. (2007) 'A computational model relating changes in cerebral blood volume to synaptic activity in neurons', *Neurocomputing*, 70(10–12), pp. 1674–1679. doi: 10.1016/j.neucom.2006.10.071.

Gilabert, J. A. (2012) 'Cytoplasmic Calcium Buffering', in Islam, M. S. (ed.). Dordrecht: Springer Netherlands (Advances in Experimental Medicine and Biology), pp. 483–498. doi: 10.1007/978-94-007-2888-2_20.

Gonzalez-Fernandez, J. M. and Ermentrout, B. (1994) 'On the origin and dynamics of the vasomotion of small arteries', *Mathematical Biosciences*, 119(2), pp. 127–167. doi: 10.1016/0025-5564(94)90074-4.

Gordleeva, S. Y. *et al.* (2019) 'Astrocyte as spatiotemporal integrating detector of neuronal activity', *Frontiers in Physiology*, 10(MAR). doi: 10.3389/fphys.2019.00294.

Guerra-Gomes, S. *et al.* (2018) 'Functional roles of astrocyte calcium elevations: From synapses to behavior', *Frontiers in Cellular Neuroscience*, 11(January), pp. 1–7. doi: 10.3389/fncel.2017.00427.

Guettier, J. *et al.* (2009) 'A chemical-genetic approach to study G protein regulation of cell function in vivo Jean-Marc', *Pnas*, 106(45), pp. 19197–19202.

Guillamón-Vivancos, T., Gómez-Pinedo, U. and Matías-Guiu, J. (2015) 'Astrocitos en las enfermedades neurodegenerativas (I): Función y caracterización molecular', *Neurologia*, 30(2), pp. 119–129. doi: 10.1016/j.nrl.2012.12.007.

Hadfield, J., Plank, M. J. and David, T. (2013) 'Modeling Secondary Messenger Pathways in Neurovascular Coupling', *Bulletin of Mathematical Biology*, 75(3), pp. 428–443. doi: 10.1007/s11538-013-9813-x.

Hayashi, M. K. and Yasui, M. (2015) 'The transmembrane transporter domain of glutamate transporters is a process tip localizer', *Scientific Reports*, 5, pp. 1–8. doi: 10.1038/srep09032.

Herculano-Houzel, S. (2009) 'The human brain in numbers: A linearly scaled-up primate brain', *Frontiers in Human Neuroscience*, 3(NOV), pp. 1–11. doi: 10.3389/neuro.09.031.2009.

Hirrlinger, J., Hülsmann, S. and Kirchhoff, F. (2004) 'Astroglial processes show spontaneous motility at active synaptic terminals in situ', *European Journal of Neuroscience*, 20(8), pp. 2235–2239. doi: 10.1111/j.1460-9568.2004.03689.x.

Horton, N. G. *et al.* (2013) 'In vivo three-photon microscopy of subcortical structures within an intact mouse brain', *Nature Photonics*, 7(3), pp. 205–209. doi: 10.1038/nphoton.2012.336.

Jafri, M. S. and Keizer, J. (1995) 'On the roles of Ca2+ diffusion, Ca2+ buffers, and the endoplasmic reticulum in IP3-induced Ca2+ waves', *Biophysical Journal*, 69(5), pp. 2139–2153. doi: 10.1016/S0006-3495(95)80088-3.

Jensen, T. P. *et al.* (2019) 'Multiplex imaging relates quantal glutamate release to presynaptic Ca 2+ homeostasis at multiple synapses in situ', *Nature Communications*. Springer US, 10(1), pp. 1–14. doi: 10.1038/s41467-019-09216-8.

Jha, B. K., Adlakha, N. and Mehta, M. N. (2014) 'Two-dimensional finite element model to study calcium distribution in astrocytes in presence of excess buffer', *International Journal of Biomathematics*, 7(3), pp. 1–11. doi: 10.1142/S1793524514500314.

Jha, B. K., Jha, A. and Adlakha, N. (2019) 'Three-Dimensional Finite Element Model to Study Calcium Distribution in Astrocytes in Presence of VGCC and Excess Buffer', *Differential Equations and Dynamical Systems*. Springer India, (0123456789). doi: 10.1007/s12591-019-00502-x.

Ji, Z. G. and Wang, H. (2015) 'Optogenetic control of astrocytes: Is it possible to treat astrocyte-related epilepsy?', *Brain Research Bulletin*. Elsevier Inc., 110, pp. 20–25. doi: 10.1016/j.brainresbull.2014.10.013.

Jungblut, M. *et al.* (2012) 'Isolation and characterization of living primary astroglial cells using the new GLAST-specific monoclonal antibody ACSA-1', *Glia*, 60(6), pp. 894–907. doi: 10.1002/glia.22322.

Kang, M. and Othmer, H. G. (2009) 'Spatiotemporal characteristics of calcium dynamics in astrocytes', *Chaos*, 19(3), pp. 1–21. doi: 10.1063/1.3206698.

Kang, M. and Othmer, H. G. (2007) 'The variety of cytosolic calcium responses and possible roles of PLC and PKC', *Physical Biology*, 4(4), pp. 325–343. doi: 10.1088/1478-3975/4/4/009.

Kang, M. and Othmer, H. G. (2009) 'Spatiotemporal characteristics of calcium dynamics in astrocytes', *Chaos*, 19(3), pp. 1–21. doi: 10.1063/1.3206698.

Keizer, G. W. D. Y. A. J. (1992) 'A single-pool inositol 1,4,5-trisphosphate-receptor-based model for agonist-stimulated oscillations in Ca2+ concentration', 89(September), pp. 9895–9899.

Kenny, A., Plank, M. J. and David, T. (2018) 'The role of astrocytic calcium and TRPV4 channels in neurovascular coupling', *Journal of Computational Neuroscience*. Journal of Computational Neuroscience, 44(1), pp. 97–114. doi: 10.1007/s10827-017-0671-7.

Khakh, B. S. and McCarthy, K. D. (2015) 'Astrocyte calcium signaling: From observations to functions and the challenges therein', *Cold Spring Harbor Perspectives in Biology*, 7(4), pp. 1–18. doi: 10.1101/cshperspect.a020404.

Khalid, M. U. *et al.* (2018) 'Geometry-based Computational Modeling of Calcium Signaling in an Astrocyte', in, pp. 157–160. doi: 10.1007/978-981-10-5122-7_40.

Komin, N. *et al.* (2015) 'Multiscale Modeling Indicates That Temperature Dependent [Ca2+]i Spiking in Astrocytes Is Quantitatively Consistent with Modulated SERCA Activity', *Neural Plasticity*, 2015. doi: 10.1155/2015/683490.

Korngreen, A., Gol'shtein, V. and Priel, Z. (1997) 'A realistic model of biphasic calcium transients in electrically nonexcitable cells', *Biophysical Journal*, 73(2), pp. 659–673. doi: 10.1016/S0006-3495(97)78101-3.

Li, Y. X. and Rinzel, J. (1994) 'Equations for InsP3 receptor-mediated [Ca2+](i) oscillations derived from a detailed kinetic model: A hodgkin-huxley like formalism', *Journal of Theoretical Biology*, pp. 461–473. doi: 10.1006/jtbi.1994.1041.

Loaiza, A., Porras, O. H. and Barros, L. F. (2003) 'Glutamate triggers rapid glucose transport stimulation in astrocytes as evidenced by real-time confocal microscopy', *Journal of Neuroscience*, 23(19), pp. 7337–7342. doi: 10.1523/jneurosci.23-19-07337.2003.

Lopez-Caamal, F. *et al.* (2014) 'Spatial quantification of cytosolic Ca2+ accumulation in non-excitable cells: An analytical study', *IEEE/ACM Transactions on Computational Biology and Bioinformatics*, 11(3), pp. 592–603. doi: 10.1109/TCBB.2014.2316010.

Losi, G. *et al.* (2017) 'New tools to study astrocyte Ca2+ signal dynamics in brain networks in vivo', *Frontiers in Cellular Neuroscience*, 11(May), pp. 1–7. doi: 10.3389/fncel.2017.00134.

Manninen, T., Havela, R. and Linne, M. L. (2018) 'Computational models for calcium-mediated astrocyte functions', *Frontiers in Computational Neuroscience*, 12(April). doi: 10.3389/fncom.2018.00014.

Minitab 19 Statistical Software (2019). [Computer software]. State College, PA: Minitab, Inc. (www.minitab.com)

McIver, S. R., Faideau, M. and Haydon, P. G. (2013) 'Astrocyte–Neuron Communications', in *Neural-Immune Interactions in Brain Function and Alcohol Related Disorders*. Boston, MA: Springer US, pp. 31–64. doi: 10.1007/978-1-4614-4729-0_2.

Nagel, G. *et al.* (2003) 'Cation-Selective Membrane Channel', *Pnas*, 100(24), pp. 13940–13945. doi: 10.1073/pnas.1936192100.

Nagelhus, E. A. and Ottersen, O. P. (2013) 'Physiological roles of Aquaporin-4 in brain', *Physiological Reviews*, 93(4), pp. 1543–1562. doi: 10.1152/physrev.00011.2013.

Nagy, J. I. *et al.* (2011) 'Connexin26 expression in brain parenchymal cells demonstrated by targeted connexin ablation in transgenic mice', *European Journal of Neuroscience*, 34(2), pp. 263–271. doi: 10.1111/j.1460-9568.2011.07741.x.

Nakayama, R. *et al.* (2016) 'Subcellular calcium dynamics during juvenile development in mouse hippocampal astrocytes', *European Journal of Neuroscience*, 43(7), pp. 923–932. doi: 10.1111/ejn.13188.

Nett, W. J., Oloff, S. H. and Mccarthy, K. D. (2002) 'Hippocampal astrocytes in situ exhibit calcium oscillations that occur independent of neuronal activity', *Journal of Neurophysiology*, 87(1), pp. 528–537. doi: 10.1152/jn.00268.2001.

Oschmann, F. *et al.* (2017) 'Spatial separation of two different pathways accounting for the generation of calcium signals in astrocytes', *PLoS Computational Biology*, 13(2), pp. 1–25. doi: 10.1371/journal.pcbi.1005377.

Parpura, V. and Zorec, R. (2010) 'Gliotransmission: Exocytotic release from astrocytes', *Brain Research Reviews*. Elsevier B.V., 63(1–2), pp. 83–92. doi: 10.1016/j.brainresrev.2009.11.008.

Patrushev, I. *et al.* (2013) 'Subcellular location of astrocytic calcium stores favors extrasynaptic neuron-astrocyte communication', *Cell Calcium*. Elsevier Ltd, 54(5), pp. 343–349. doi: 10.1016/j.ceca.2013.08.003.

Perea, G., Navarrete, M. and Araque, A. (2009) 'Tripartite synapses: astrocytes process and control synaptic information', *Trends in Neurosciences*, 32(8), pp. 421–431. doi: 10.1016/j.tins.2009.05.001.

Perea, G. *et al.* (2014) 'Optogenetic astrocyte activation modulates response selectivity of visual cortex neurons in vivo', *Nature Communications*. Nature Publishing Group, 5. doi: 10.1038/ncomms4262.

Perez-Alvarez, A., Araque, A. and Martin, E. D. (2013) 'Confocal microscopy for astrocyte in vivo imaging: Recycle and reuse in microscopy', *Frontiers in Cellular Neuroscience*, 7(APR), pp. 1–10. doi: 10.3389/fncel.2013.00051.

Pfaff, D. W., & Volkow, N. D. (Eds.). (2016). N. in the 21st C. doi:10. 1007/97.-1-4939-3474-4 (2016) *Neuroscience in the 21st Century*, *Neuroscience in the 21st Century: From Basic to Clinical, Second Edition*. Edited by D. W. Pfaff and N. D. Volkow. New York, NY: Springer New York. doi: 10.1007/978-1-4939-3474-4.

Preston, A. N., Cervasio, D. A. and Laughlin, S. T. (2019) *Visualizing the brain's astrocytes*. 1st edn, *Methods in Enzymology*. 1st edn. Elsevier Inc. doi: 10.1016/bs.mie.2019.02.006.

Preston, A. N. *et al.* (2018) 'Visualizing the Brain's Astrocytes with Diverse Chemical Scaffolds', *ACS Chemical Biology*. American Chemical Society, 13(6), pp. 1493–1498. doi: 10.1021/acschembio.8b00391.

Richardson, A. and Taylor, C. W. (1993) 'Effects of Ca2+ chelators on purified inositol 1,4,5-trisphosphate (InsP3) receptors and InsP3-stimulated Ca2+ mobilization', *Journal of Biological Chemistry*, 268(16), pp. 11528–11533.

Rubenstein, D. A., Yin, W., & Frame, M. D. (2012). Fundamentals of Fluid Mechanics. Biofluid Mechanics, 11–48. doi:10.1016/b978-0-12-381383-1.00002-3

Rusakov, D. A. (2015) 'Disentangling calcium-driven astrocyte physiology', *Nature Reviews Neuroscience*. Nature Publishing Group, 16(4), pp. 226–233. doi: 10.1038/nrn3878.

Savtchenko, L. P. *et al.* (2018) 'Disentangling astroglial physiology with a realistic cell model in silico', *Nature Communications*, 9(1). doi: 10.1038/s41467-018-05896-w.

SCEMES, E. (2006) 'Astrocyte Calcium Waves: What They Are and What They Do', *Sixth Report on the World Nutrition Situation Geneva*, 479(March), p. 132. doi: 10.1002/glia.20374.

Schwaller, B. (2010) 'Ca2+ buffers', *Handbook of Cell Signaling, 2/e*, 2, pp. 955–962. doi: 10.1016/B978-0-12-374145-5.00120-0.

Skupin, A., Kettenmann, H. and Falcke, M. (2010) 'Calcium signals driven by single channel noise', *PLoS Computational Biology*, 6(8), pp. 17–19. doi: 10.1371/journal.pcbi.1000870.

Srinivasan, R. *et al.* (2015) 'Ca2+ signaling in astrocytes from Ip3r2−/− mice in brain slices and during startle responses in vivo', *Nature Neuroscience*, 18(5), pp. 708–717. doi: 10.1038/nn.4001.

Sun, W. *et al.* (2017) 'SOX9 is an astrocyte-specific nuclear marker in the adult brain outside the neurogenic regions', *Journal of Neuroscience*, 37(17), pp. 4493–4507. doi: 10.1523/JNEUROSCI.3199-16.2017.

Swanson, L. *et al.* (1999) 'Tripartite synapses : glia , the unacknowledged partner', 22(5).

Tada, M., Nishizawa, M. and Onodera, O. (2012) *Calcium Signaling*, *Neurochemistry International*. Edited by M. S. Islam. Dordrecht: Springer Netherlands (Advances in Experimental Medicine and Biology). doi: 10.1007/978-94-007-2888-2.

Ullah, G., Jung, P. and Cornell-Bell, A. H. (2006) 'Anti-phase calcium oscillations in astrocytes via inositol (1, 4, 5)-trisphosphate regeneration', *Cell Calcium*, 39(3), pp. 197–208. doi: 10.1016/j.ceca.2005.10.009.

Urban, D. J. and Roth, B. L. (2015) 'DREADDs (Designer Receptors Exclusively Activated by Designer Drugs): Chemogenetic Tools with Therapeutic Utility', *Annual Review of Pharmacology and Toxicology*, 55(1), pp. 399–417. doi: 10.1146/annurev-pharmtox-010814-124803.

Vardy, E. *et al.* (2015) 'A New DREADD Facilitates the Multiplexed Chemogenetic Interrogation of Behavior', *Neuron*. Elsevier Inc., 86(4), pp. 936–946. doi: 10.1016/j.neuron.2015.03.065.

Verkhratsky, A. and Butt, A. (2013) *Glial Physiology and Pathophysiology*, *Glial Physiology and Pathophysiology*. doi: 10.1002/9781118402061.

Verkhratsky, A. and Nedergaard, M. (2018) 'Physiology of astroglia', *Physiological Reviews*, 98(1), pp. 239–389. doi: 10.1152/physrev.00042.2016.

Verkhratsky, A. *et al.* (2010) 'Astrocytes in Alzheimer's disease', *Neurotherapeutics*, 7(4), pp. 399–412. doi: 10.1016/j.nurt.2010.05.017.

Volterra, A. and Meldolesi, J. (2005) 'Astrocytes, from brain glue to communication elements: The revolution continues', *Nature Reviews Neuroscience*, 6(8), pp. 626–640. doi: 10.1038/nrn1722.

Wagner, J. and Keizer, J. (1994) 'Effects of rapid buffers on Ca2+ diffusion and Ca2+ oscillations', *Biophysical Journal*, 67(1), pp. 447–456. doi: 10.1016/S0006-3495(94)80500-4.

Wang, Z. *et al.* (1997) 'Impact of cytoplasmic calcium buffering on the spatial and temporal characteristics of intercellular calcium signals in astrocytes', *Journal of Neuroscience*, 17(19), pp. 7359–7371. doi: 10.1523/jneurosci.17-19-07359.1997.

Weisberg, S. (2005). Applied linear regression. Hoboken, NJ: Wiley-Interscience.

Wieder, N., Fink, R. and Von Wegner, F. (2015) 'Exact stochastic simulation of a calcium microdomain reveals the impact of Ca2+ fluctuations on IP3R gating', *Biophysical Journal*. Biophysical Society, 108(3), pp. 557–567. doi: 10.1016/j.bpj.2014.11.3458.

Wilhelmsson, U. *et al.* (2006) 'Redefining the concept of reactive astrocytes as cells that remain within their unique domains upon reaction to injury', *Proceedings of the National Academy of Sciences of the United States of America*, 103(46), pp. 17513–17518. doi: 10.1073/pnas.0602841103. "Copyright (2006) National Academy of Sciences, U.S.A."

Witthoft, A. and Em Karniadakis, G. (2012) 'A bidirectional model for communication in the neurovascular unit', *Journal of Theoretical Biology*. Elsevier, 311, pp. 80–93. doi: 10.1016/j.jtbi.2012.07.014.

Witthoft, A., Filosa, J. A. and Karniadakis, G. E. (2013) 'Potassium buffering in the neurovascular unit: Models and sensitivity analysis', *Biophysical Journal*. Biophysical Society, 105(9), pp. 2046–2054. doi: 10.1016/j.bpj.2013.09.012.

Wu, Y. W. *et al.* (2019) 'Morphological profile determines the frequency of spontaneous calcium events in astrocytic processes', *Glia*, 67(2), pp. 246–262. doi: 10.1002/glia.23537.

Ye, L. *et al.* (2017) 'Comparison of GCaMP3 and GCaMP6f for studying astrocyte Ca2+ dynamics in the awake mouse brain', *PLoS ONE*, 12(7), pp. 1–17. doi: 10.1371/journal.pone.0181113

8. APPENDIX

Table A1: *Parameters from De Pittà et al. (2009) used in this study*

	Value	Description
rC	6 s-1	Maximal CICR rate
C0	2 μM	Total cell free Ca2+ concentration referred to the cytosol volume
c1	0.185	Ratio between cytosol volume and ER volume
rL	0.11 s-1	Maximal rate of Ca2+ leak from the ER
υER	0.9 μM s-1	Maximal rate of SERCA uptake
KER	0.05 μM	SERCA Ca2+ affinity
d1	0.13 μM	IP3 dissociation constant
d2	1.049 μM	Ca2+ inactivation dissociation constant
d3	0.9434 μM	IP3 dissociation constant
d5	0.08234 μM	Ca2+ activation dissociation constant
a2	0.2 s-1	IP3R binding rate for Ca2+ inhibition
Agonist-independent IP3 production		
ῡδ	0.05	Maximal rate of IP3 production by PLC
KPLCδ	0.1	Inhibition constant of PLC activity
kδ	1.5	Ca2+ affinity of PLC
IP3 degradation		
r5P	0.05	Maximal rate of degradation by IP-5P
ῡ3K	2	Maximal rate of degradation by IP3-3K
KD	0.7	Ca2+ affinity of IP3-3K
K3	1	IP3 affinity of IP3-3K
Agonist-dependent IP3 production		
ῡβ	0.5	Maximal rate of IP3 production by PLC
KR	1.3	Glutamate affinity of the receptor
Kp	10	Ca2+/PKC-dependent inhibition factor
Kπ	0.6	Ca2+ affinity of PKC

ANOVA test for the main process change in bifurcation geometry

First, making a box-plot of the Ca^{2+} frequency to check if there was any significant difference between the two stimulus positions (Figure A1).

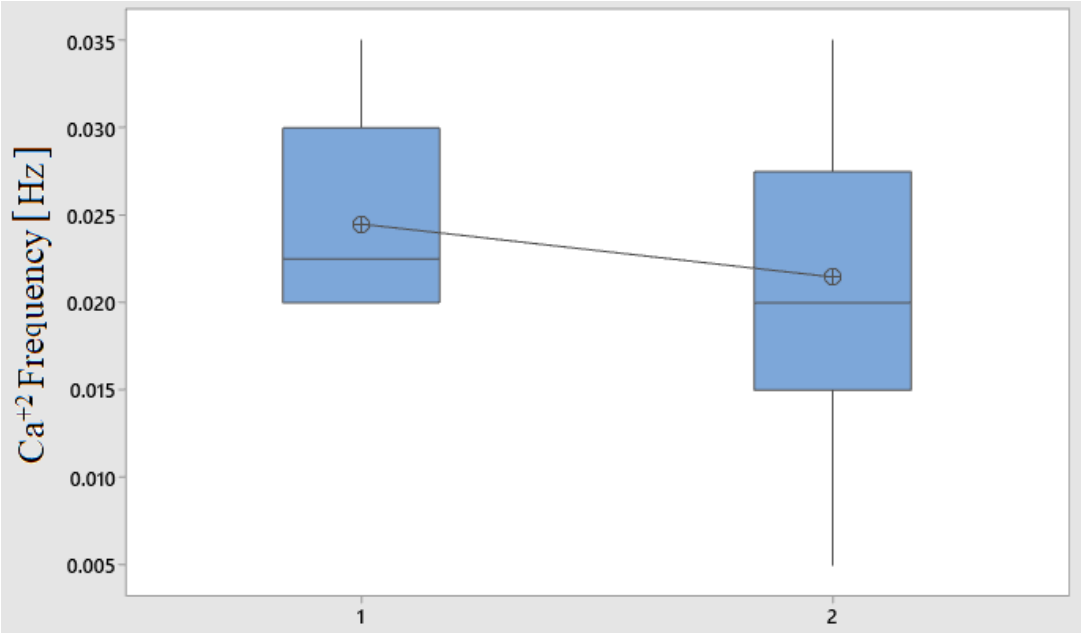

Figure A1. *Boxplot of the two different stimulus positions for the main process length change in geometry 2, position 1 represents the simulations where the stimulus event was located in just one subprocess and position 2 when the stimulus area was divided between both subprocesses.*

There were no big differences between the simulations with the stimulus position located on one side and the ones with it located in both positions. For proving that mathematically and statistically, an ANOVA test was done to compare these two different simulations.

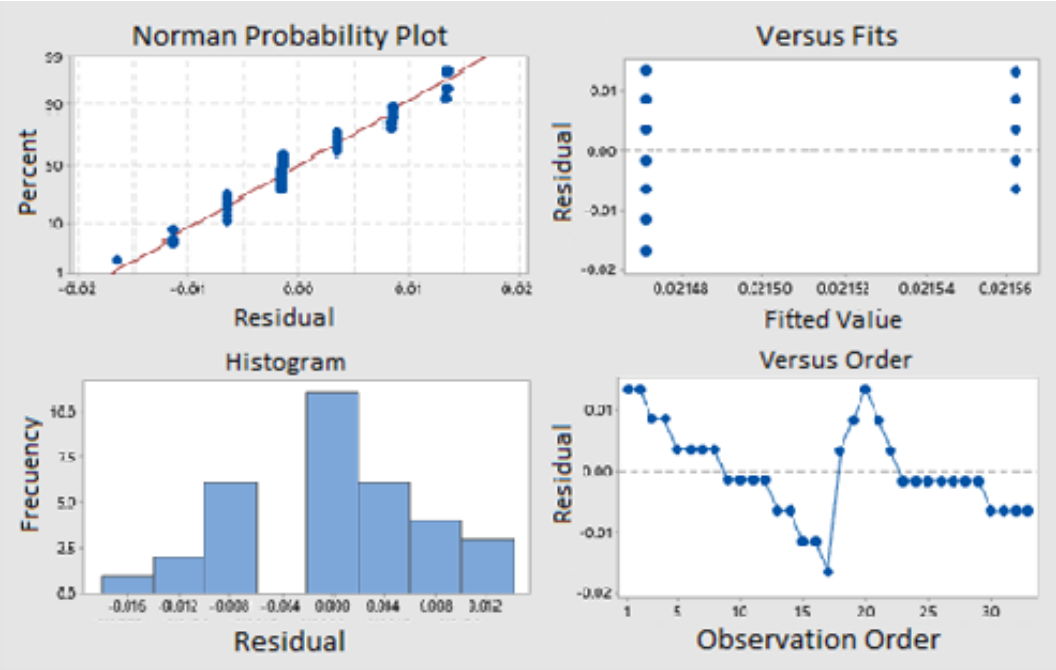

Figure A2. *Residual analysis for ANOVA test of the frequency of the Ca^{2+} event, it is done in geometry 2 in the body length changing simulation for the different synaptic positions.*

Table A2. Variance analysis for ANOVA residuals

Source	DF	Adj SS	Adj MS	F_vaule	p_value
Sinapse Numb	1	0.000000	0.000000	0.00	0.972
Error	31	0.001724	0.000056		
Total	32	0.001724			

Table A3. *Means analysis in ANOVA test*

Stimulus Distribution	N	Mean	StDev	CI de 95%
1	16	0.02156	0.00598	(0.01776; 0.02537)
2	17	0.02147	0.00862	(0.01778; 0.02516)

Clustered Standard Errors = 0.00745778

Tukey's range test contained the 0 in its interval, which means that there were no significant differences in their means, taking into account the dispersion of the data (Figure A3).

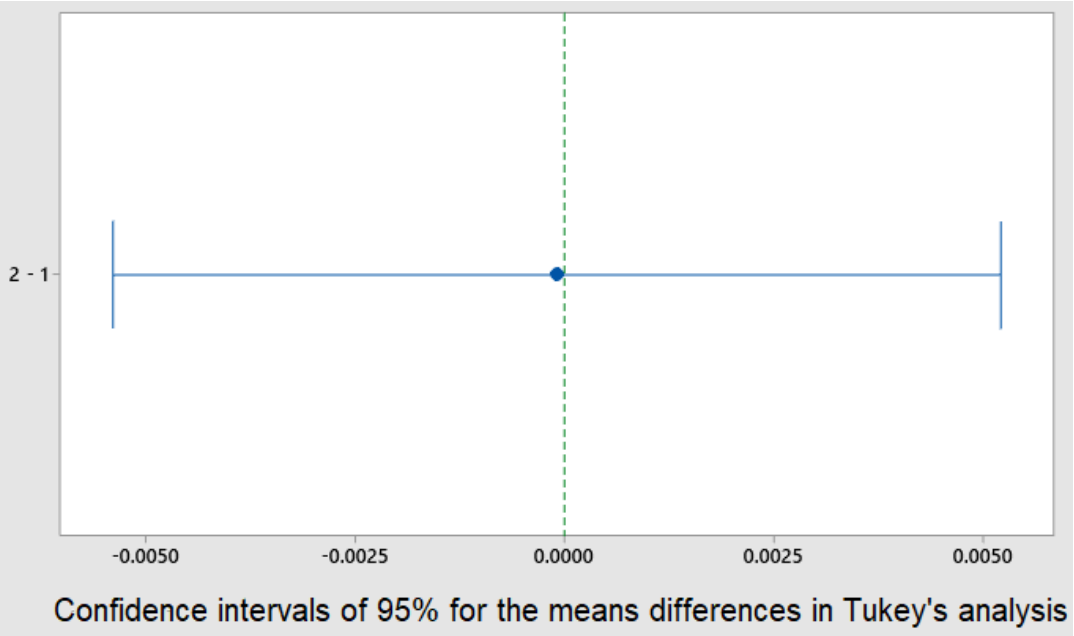

Figure A3. *Confidence intervals of 95% with the Tukey method for the mean differences between stimulus locations 1 and 2. If the interval contains the 0 value, It is not possible to assume that models offer significative differences in their means.*

Table A4. *Minitab Tukey's range test result for the means*

Stimulus Distribution	N	Mean	Clusters
2	16	0.02156	A
1	17	0.02147	A

Means that share the same cluster letter are not significantly different.

ANOVA test for the subprocess length change in bifurcation geometry

Analysis of differences between the stimulus positions in the subprocess length change. Stimulus position "1" refers to the model where the stimulus area was located in one of the subprocesses, and the opposite one is growing its length, stimulus position "2" refers to the model where the synaptic area was distributed by the two subprocesses, and stimulus position "3" is the one where the synaptic area was located in the subprocess that changed its length.

Table A5. Variance analysis for ANOVA residuals

Source	DF	Adj SS	Adj MS	F_vaule	p_value
Sinapse Numb	2	0.000020	0.000010	0.11	0.893
Error	55	0.004830	0.000088		
Total	57	0.004850			

Table A6. *Means analysis in ANOVA test*

Stimulus Distribution	N	Mean	StDev	CI de 95%
1	21	0.02952	0.00740	(0.02543; 0.03362)
2	21	0.02976	0.00782	(0.02566; 0.03386)
3	16	0.03094	0.01294	(0.02624; 0.03563)

Clustered standard deviation = 0.00937112

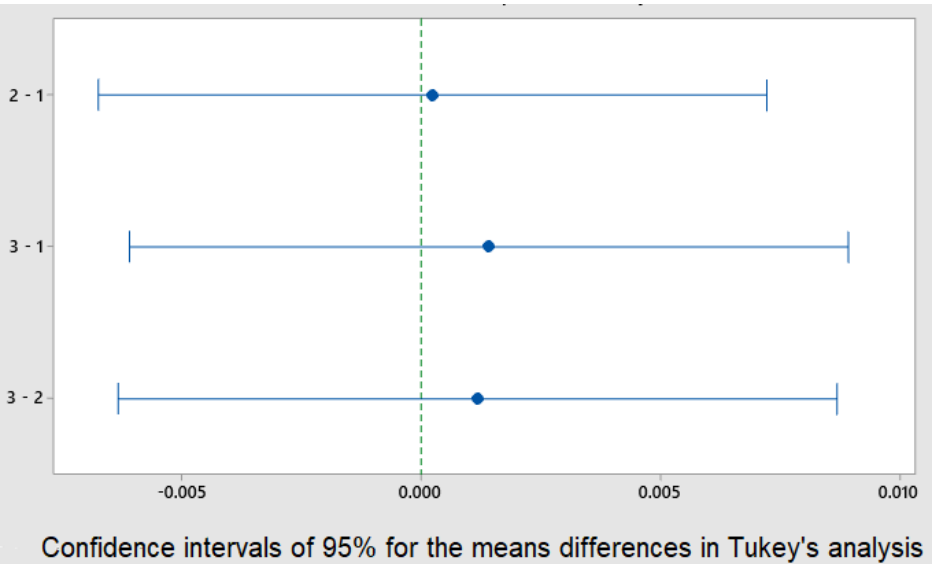

Figure A4. Confidence intervals of 95% with the Tukey method for the frequency of the Ca^{2+} event mean differences between the three synaptic positions in the second simulation configurations of geometry *2.*

Table A7 *Minitab Tukey's range test result for the means*

Stimulus Distribution	N	Mean	Clusters
3	16	0.03094	A
2	21	0.02976	A
1	21	0.02952	A

In this case, there were no significant differences in the result between the three synaptic positions, and the 3 of them can be studied under the same multiple linear regression analysis.

ANOVA test for the subprocess length change in bifurcation geometry

Analysis of differences between the stimulus positions in the subprocess length change. Stimulus position “1” refers to the model where the stimulus area was located in one of the subprocesses, and the opposite one is growing its length, stimulus position “2” refers to the model where the synaptic area was distributed by the two subprocesses, and stimulus position “3” is the one where the synaptic area was located in the subprocess that changed its length.

Table A5. Variance analysis for ANOVA residuals

Source	DF	Adj SS	Adj MS	F_vaule	p_value
Sinapse Numb	2	0.000020	0.000010	0.11	0.893
Error	55	0.004830	0.000088		
Total	57	0.004850			

Table A6. *Means analysis in ANOVA test*

Stimulus Numb	N	Mean	StDev	CI de 95%
1	21	0.02952	0.00740	(0.02543; 0.03362)
2	21	0.02976	0.00782	(0.02566; 0.03386)
3	16	0.03094	0.01294	(0.02624; 0.03563)

Clustered standard deviation = 0.00937112

Regression analysis of the Ca^{2+} FWHM in the rectangular geometry in Probe 3

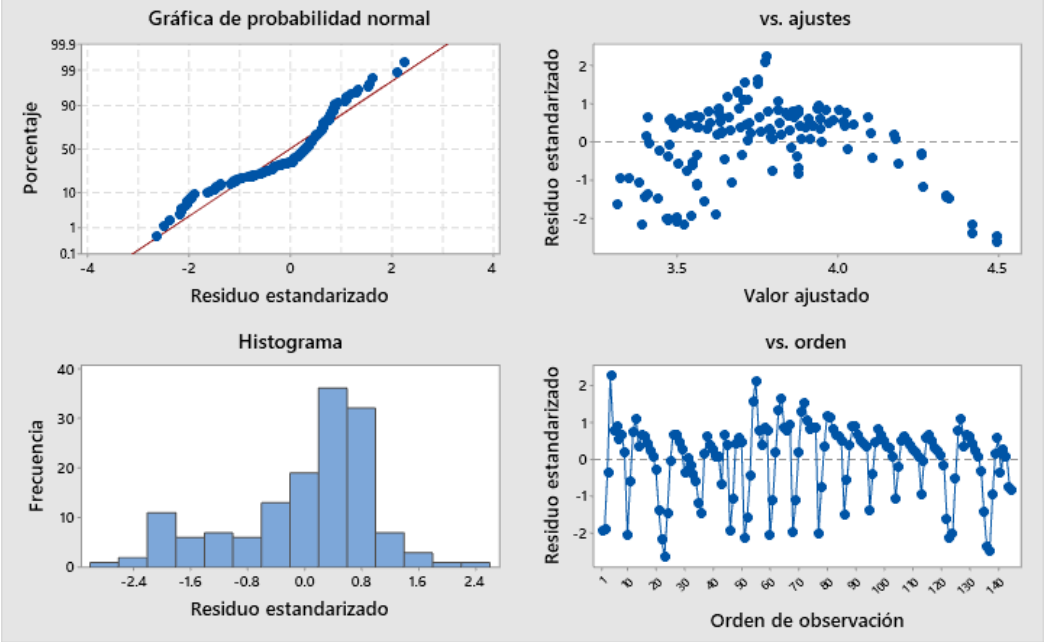

Figure A5. *Residual analysis of the FWHM of the Ca^{2+} event*

Table A8. Multiple linear regression, analysis of the variance

Source	DF	Adj SS	Adj MS	F_vaule	p_value
Regresion	2	9.8807	4.94036	18.07	0.000
Parameter_L	1	8.9898	8.98985	32.89	0.000
Parameter_W	1	0.7069	0.70695	2.59	0.110
Error	142	38.8163	0.27335		
Ajust error	120	38.6383	0.32199	39.79	0.000
Pure error	22	0.1780	0.00809		
Total	144	48.6970			

Table A8. *Multiple linear regression, model summary*

S	R^2	R^2 (adjust)	R^2 (pred)
0.522833	20.29%	19.17%	15.60%

Table A9. *Multiple linear regression coefficients*

Term.	Coef	Coef_EE	T_value	p_value	VIF
Constant	3.220	0.175	18.41	0.000	
Parameter_L	0.00791	0.00138	5.73	0.000	1.00
Parameter_W	-0.1458	0.0907	-1.61	0.110	1.00

Regression equation

widthsavg_s3 = 3.220 + 0.00791 Parameter_L - 0.1458 Parameter_W

Regression analysis of the Ca^{2+} average amplitude in the rectangular geometry in Probe 3

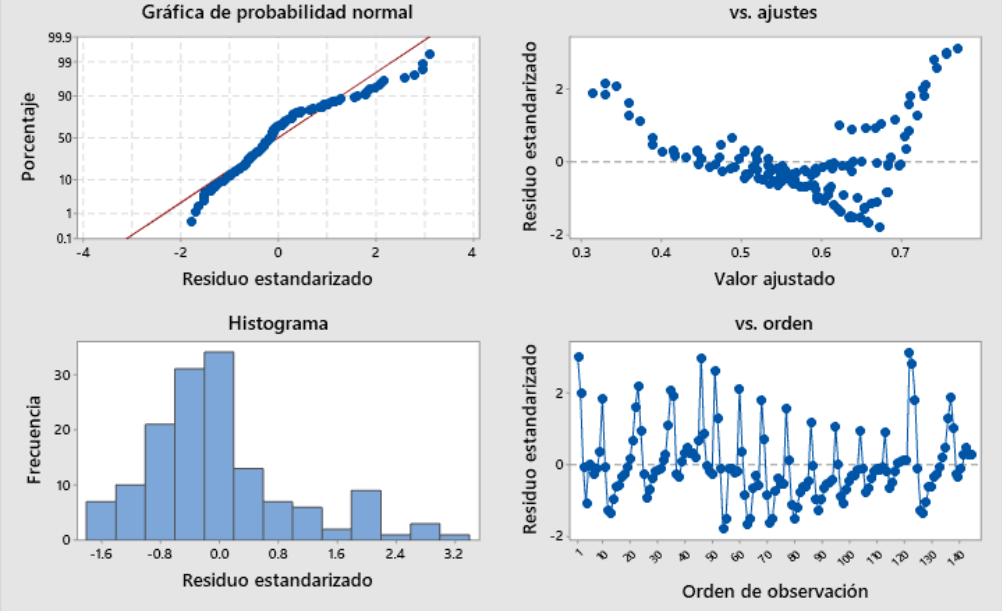

Figure A6. *Residual analysis of the Ca^{2+} average amplitude*

Table A10. Multiple linear regression, analysis of the variance

Source	DF	Adj SS	Adj MS	F_vaule	p_value
Regresion	2	1.48307	0.74153	169.78	0.000
Parameter_L	1	1.24967	1.24967	286.13	0.000
Parameter_W	1	0.27149	0.27149	62.16	0.000
Error	142	0.62019	0.00437		
Ajust error	120	0.61958	0.00516	185.18	0.000
Pure error	22	0.00061	0.00003		
Total	144	2.10326			

Table A11. *Multiple linear regression, model summary*

S	R-cuad.	R-cuad. (adjust)	R-cuad. (pred)
0.0660875	70.51%	70.10%	68.85%

Table A12. *Multiple linear regression coefficients*

Term.	Coef	Coef_EE	T_value	p_value	VIF
Constant	0.9503	0.0221	42.97	0.000	
Parameter_L	-0.002949	0.000174	-16.92	0.000	1.00
Parameter_W	-0.0904	0.0115	-7.88	0.000	1.00

Regression equation

peaksavg_s3 0.9503 - 0.002949 Parameter_L - 0.0904 Parameter_W

Regression analysis of the Ca^{2+} FWHM in the bifurcation geometry

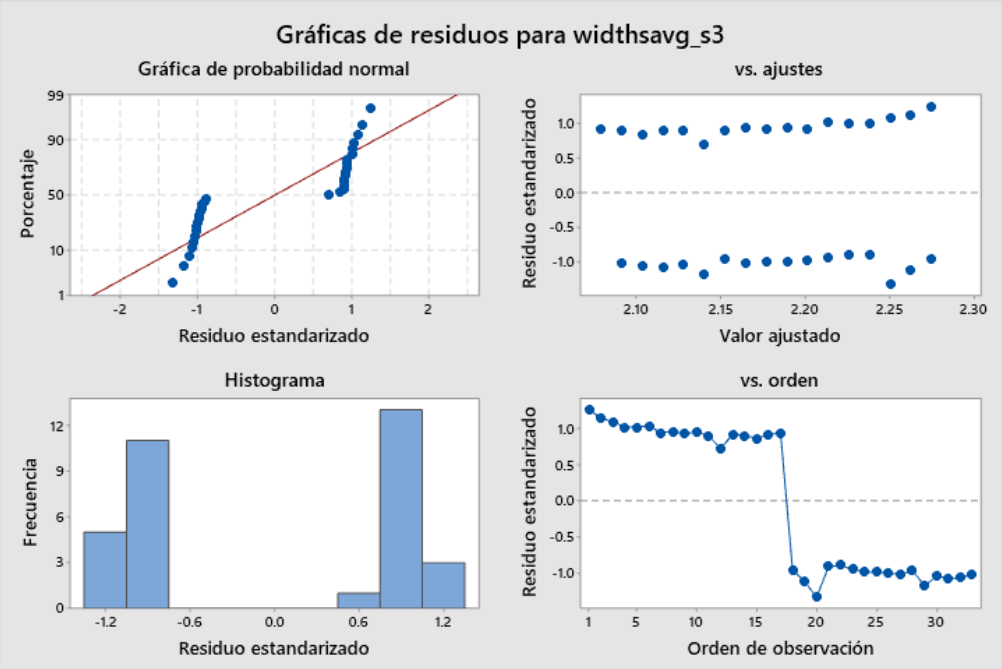

Figure A7. *Residual analysis of the Ca^{2+} FWHM in the bifurcation geometry*

Table A13. Multiple linear regression, analysis of the variance

Source	DF	Adj SS	Adj MS	F_vaule	p_value
Regresion	1	0.1127	0.11268	0.19	0.664
area_s2	1	0.1127	0.11268	0.19	0.664
Error	31	18.2101	0.58742		
Ajust error	15	0.5840	0.03893	0.04	1.000
Pure error	16	17.6261	1.10163		
Total	32	18.3228			

Table A14. *Multiple linear regression, model summary*

S	R-cuad.	R-cuad. (ajustado)	R-cuad. (pred)
0.766435	0.61%	0.00%	0.00%

Table A15. *Multiple linear regression coefficients*

Term.	Coef	Coef_EE	T_value	p_value	VIF
Constant	2.180	0.133	16.34	0.000	
area_s2	-0.059	0.135	-0.44	0.664	1.00

Regression equation

FWHM = 2.394 - 0.00123 area_s2

Regression analysis of the Ca^{2+} average amplitude in the bifurcation geometry

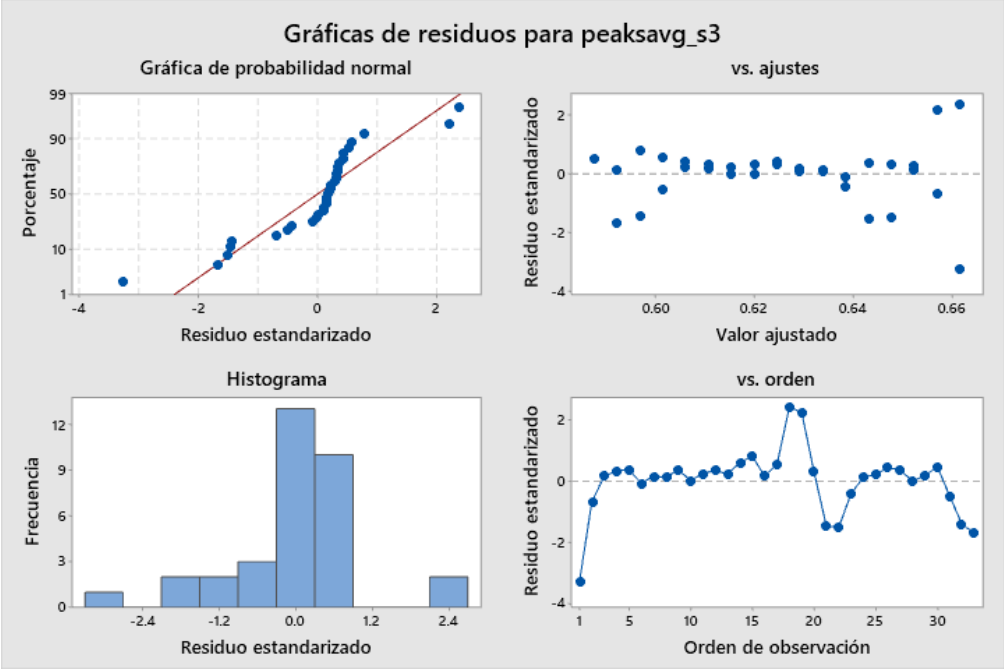

Figure A8. *Residual analysis of the Ca^{2+} average amplitude in the bifurcation geometry*

Table A16. Multiple linear regression, analysis of the variance

Source	DF	Adj SS	Adj MS	F_vaule	p_value
Regression	1	0.1127	0.11268	0.19	0.664
area_s2	1	0.1127	0.11268	0.19	0.664
Error	31	18.2101	0.58742		
Ajust error	15	0.5840	0.03893	0.04	1.000
Pure error	16	17.6261	1.10163		
Total	32	18.3228			

Table A17. *Multiple linear regression, model summary*

S	R-cuad.	R-cuad. (ajustado)	R-cuad. (pred)
0.0254879	44.51%	42.72%	32.43%

Table A18. *Multiple linear regression coefficients*

Term.	Coef	Coef_EE	T_value	p_value	VIF
Constant	0.62574	0.00444	141.03	0.000	
area_s2	-0.02247	0.00451	-4.99	0.000	1.00

Regression equation

Amplitude= 0.7066 - 0.000464 area_s2